Thesis for a Ph.D. Degree

Rainfall structure of tropical cyclone over the globe: The present characteristics and future changes

전 지구 태풍의 강수 구조:
현재 특성과 미래 변화

February 2020

School of Earth and Environmental Sciences
Graduate School
Seoul National University

Dasol Kim

Rainfall structure of tropical cyclone over the globe: The present characteristics and future changes

지도 교수 허 창 회

이 논문을 이학박사 학위논문으로 제출함
2020년 1월

서울대학교 대학원
지구환경과학부
김 다 솔

김다솔의 이학박사 학위논문을 인준함
2020년 1월

위 원 장 백 종 진 (인)
부위원장 허 창 회 (인)
위 원 (인)
위 원 (인)
위 원 JOHNNY CHAN (인)

Rainfall structure of tropical cyclone over the globe: The present characteristics and future changes

By

Dasol Kim

Dissertation Submitted to the Faculty of the Graduate School of the Seoul National University for the Degree of Doctor of Philosophy

Degree Awarded:
February 2020

Advisory committee:

Professor	Jong-Jin Baik,	Chair
Professor	Chang-Hoi Ho,	Advisor
Professor	Seok-Woo Son	
Doctor	Hee-Dong Yoo	
Professor	Johnny C. L. Chan	

Abstract

Tropical cyclones (TCs) incurring gusty winds and heavy rainfall are the most destructive meteorological disasters. In particular, floods related to TCs cause serious economic losses and casualties. Accurate prediction of TC rainfall, therefore, will bring great social benefits. However, TC rainfall has received less attention than other TC characteristics such as track, and intensity. Key information of TC rainfall such as global climatology and mechanisms for its variation is required to predict TC rainfall, but it has not been studied in detail. In this dissertation, climatological characteristics of TC rainfall were investigated over the globe using satellite observation data. The role of multiple factors affecting TC rainfall such as the primary circulation, and environmental conditions were also examined. Through this approach, basic knowledge of TC rainfall can be improved. In addition, changes in TC rainfall according to global warming were investigated using a high-resolution global climate model.

Global climatology of TC rainfall was investigated using TRMM-3B42 precipitation data during 1998–2013. This study defined two indices representing rainfall structure of TCs. The inner-core rainfall strength (RS) and total rainfall area (RA) indicate intensity and spatial scale of TC rainfall, respectively. Various characteristics of TC rainfall such as basic statistics, spatial and temporal distributions were explored. The RS and RA significantly vary according to region, month, and year. To understand what

causes the variations of TC rainfall, relationships between TC rainfall and various factors such as the primary circulation and environmental conditions were examined. The results suggest that RS is primarily controlled by the primary circulation and less affected by environmental conditions, which is vice versa for the RA. Variation of RA is significantly related to large-scale low (or high) pressure systems, and environmental flows with SST.

The relationships between TC rainfall and controlling factors also vary depending on region, particularly for the RA and environmental flows, which indicates their relationship is non-linear. To understand non-linear relationship between TC rainfall and environmental conditions, variations of RA over the tropics and mid-latitudes were investigated. In mid-latitudes, stronger environmental flows significantly contribute to an increase in RA by making horizontal rainfall distribution more asymmetric, while sea surface temperature has minor contribution to the fluctuation of RA. This relationship between RA and environmental conditions in mid-latitudes is almost opposite to that in the tropics. In the mid-latitudes, TCs weaken due to cool SST and loose resistance to environmental flows, which can be the reason for the non-linear response of RA on environmental flows and sea surface temperature. Changes in TC rainfall influenced by environmental flows and related processes were also investigated by examining TCs making landfall over South Korea. In general, TCs show significantly asymmetric wind and rainfall structures, with strong vertical wind shear appearing over South Korea. The RA significantly increases with environmental vertical wind shear while the

wind area is not sensitive to it. Analysis on the cases of strong and weak vertical wind shear confirms that the increase of RA is related to the asymmetric convection (rising/sinking motion in the downshear-left/upshear-right side) induced by the vertical wind shear.

Based on the knowledge of factors controlling TC rainfall, multi-variable linear regression models for RS and RA over the six ocean basins were constructed. The regression models explain 10.9–37.2% and 27.0–41.0% variability of the RS and RA over the six basins, respectively. Also, spatial distributions of mean RS and RA estimated from the model are similar to those from the observation. The pattern correlations of RS and RA between the observation and regression model in the NI, WP, EP, and NA are 0.52–0.95, and 0.74–0.95, respectively. The correlation coefficients of RS and RA between the observation and model are significant in most area of the four basins. Therefore, current statistical models successfully explain climatological spatial distributions of RS and RA in the Northern Hemisphere. On the other hand, RS and RA models for the SI, and SP show low performance to estimate climatological distributions and variations of RS and RA.

Lastly, future changes in TC rainfall under global warming were projected using a high-resolution global climate model. The control and RCP4.5 experiments are performed for 70 years prescribing SST and radiative forcing obtained from climatological values from observation (1986–2005) and 17 CMIP5 models (2081–2100), respectively. Although the control

experiment overestimates RS, the model captures the present climatology of TC rainfall including spatial and temporal variations of RS and RA. In RCP4.5 experiment, RS homogeneously increases over the globe, while RA presents a wave-like changes in the tropics and homogeneous increase in the mid-latitudes. Analysis of changes in controlling factors suggests that the homogeneous increase in RS can be associated with a homogeneous increase in V_{max} and SST over the globe. Wave-like changes in RA in the tropics may be affected by weakening of the Walker Circulation. In addition, homogeneous increase in V_{max} and environmental flows in the Southern Hemisphere may increase RA in mid-latitudes.

Keywords: tropical cyclone, rainfall, global climatology, global climate model, climate change

Student Number: 2012-20334

Table of Contents

List of Figures

Fig. 3.1.4. Monthly distribution of RS over the globe, and the six basins. The 95% significance interval of the mean value is plotted in dark gray.

Fig. 3.1.5. Same as Fig. 3.1.4, but for the RA.

Fig. 3.1.6. Yearly distribution of RS over the globe, and the six basins. The 95% significance interval of the mean value is plotted in dark gray. Blue lines indicate linear regression lines of which slope is significant in 95% confidence level.

Fig. 3.1.7. Same as Fig. 3.1.6, but for the RA.

Fig. 3.2.1. Mean distributions of TC rainfall (unit: mm hr^{-1}) according to the quartile bins of V_{max}. The directions of x- and y- axis are right and front to TC motion, respectively. The dashed circle indicates the inner-core region of TCs.

Fig. 3.2.2. Correlation coefficients between RS and multiple parameters (i.e., SST, RH700, RV850, DV850, DV200, VWS, STEER, and Vmax) for the globe (GB; black bars) and individual ocean basins (NI, WP, EP, NA, SI, and SP; red, green, blue, orange, purple, and pink, respectively).

Fig. 3.2.3. Same as the Fig. 3.2.2, but for the RA.

Fig. 3.2.4. Eigenvalue of the eight factors (i.e., F1–F8) for the six ocean basins. Eigenvalue means total sum of squared factor loadings which are the correlation coefficients between factor and analyzed variables.

Fig. 3.2.5. Correlation coefficients between F1 and multiple parameters (i.e., SST, RH700, RV850, DV850, DV200, VWS, STEER, and Vmax) for the six ocean basins.

Fig 3.2.6. Same as the Fig 3.2.4, but for the F2.

Fig 3.2.7. Same as the Fig 3.2.4, but for the F3.

Fig. 3.2.8. Correlation coefficients between TC rainfall (i.e., RS and RA) and three major factors (i.e., F1–F3) in the NI. The correlation coefficient in each 5 degree grid box is calculated from the TCs of which centers are located in the grid box.

Fig. 3.2.9. Same as the Fig. 3.2.7, but for the WP.

Fig. 3.2.10. Same as the Fig. 3.2.7, but for the EP.

Fig. 3.2.11. Same as the Fig. 3.2.7, but for the NA.

Fig. 3.2.12. Same as the Fig. 3.2.7, but for the SI.

Fig. 3.2.13. Same as the Fig. 3.2.7, but for the SP.

Fig. 3.2.14. Global TC tracks during 1998–2013 and locations of six ocean basins. The black lines indicate TC tracks of mid-latitudes analyzed in this study.

Figure 3.2.15. Distributions of RA with varying a–b) Vmax, c–d) SST, e–f) STEER, and g–h) VWS. Left and right columns present the analysis result for global and individual subtropical ocean basins, respectively. Dots and error bars denote the mean and 95% confidence interval of the mean, respectively. Only bins with sample numbers larger than 50 are presented here.

Figure 3.2.16. Distributions of SST with varying a) STTER, and b) VWS in the mid-latitudes and the tropics of global oceans. Dots and error bars denote the mean and 95% confidence interval of the mean, respectively. Only bins with sample numbers larger than 50 are presented here.

Figure 3.2.17. Average RA in azimuthal bins (unit: 10^4 km^2) in the a) WP, b) NA, c) SI, and d) SP. Blue and red arrows indicate the direction of TC motion and vertical wind shear, respectively. Dots and error bars denote the mean and 95% confidence interval of the mean, respectively.

Figure 3.2.18. Rainfall asymmetry distributions of mid-latitude TCs in global and individual ocean basins with varying a) STEER, and b) VWS. The relationship between RA and asymmetry are shown in c). Dots and error bars denote the mean and 95% confidence interval of the mean, respectively. Only bins with sample numbers larger than 50 are presented here.

Fig. 3.2.19. Tracks of TCs making landfall over South Korea during 1998–2013. The black and gray lines indicate tracks of landfall period and entire life time of each TC, respectively. Dots denote the genesis locations of TCs.

Fig. 3.2.20. Averaged horizontal TC structures of (a) wind at 10-m level (arrows, unit: m s^{-1}) with its speed (shaded, unit: m s^{-1}), (b) precipitation rate (unit: mm hr^{-1}), and divergence (shaded, unit: 10-5 s^{-1}) and wind (arrows, unit: m s^{-1}) at (c) 10-m and (d) 250 hPa level during the landfall period. The directions of x- and y- axis are right and front to TC motion, respectively.

Fig. 3.2.21. The (a) mean and (b) standard deviation of vertical wind shear over the East Asia region during the landfall period.

Fig. 3.2.22. Distributions of the (a) wind area, and (b) rainfall area according to the vertical wind shear. The solid line in each plot denotes the linear regression line.

Fig. 3.2.23. Averaged horizontal TC structure of wind at 10-m level (arrows, unit: m s^{-1}) with its speed (shaded, unit: m s^{-1}), and precipitation rate (unit: mm hr^{-1}) for the (a, b) strong shear (SS) case, (c, d) weak shear (WS) case, and (e, f) their differences (SS minus WS) during the landfall period. The directions of x- and y- axis are right and front to TC motion, respectively. The gray dots indicate the statistically significant differences at the 95% confidence level evaluated with Student's *t*-test.

Fig. 3.2.24. The vertical velocity (shaded, unit: 10^{-1} hPa s^{-1}) at 500 hPa level and the vertical wind shear vector (arrow, unit: m s^{-1}) in the (a) SS case, (b) WS case, and (c) their differences (SS minus WS) during the landfall periods. The directions of x- and y- axis are right and front to TC motion, respectively. The gray dots indicate the statistically significant differences at the 95% confidence level evaluated with Student's *t*-test.

Fig. 3.2.25. The difference composite (SS minus WS) of vertical wind shear (arrows, unit: m s-1) and its magnitude (shaded, unit: m s^{-1}) between 850 and 250 hPa level. The thick black arrows and gray dots indicate the statistically significant differences at the 95% confidence level evaluated with Student's *t*-test.

Fig. 3.2.26. The distribution of TC center for the SS (red) and WS (blue) cases.

Fig. 3.2.27. Mean a) RI, and b) RA in each 5 degree grid box estimated by the statistical model for the NI. The correlation coefficient between the observation and estimation in each grid box is presented in c), and d).

Fig. 3.2.28. Same as Fig. 3.2.27, but for the WP.

Fig. 3.2.29. Same as Fig. 3.2.27, but for the WP.

Fig. 3.2.30. Same as Fig. 3.2.27, but for the EP.

Fig. 3.2.31. Same as Fig. 3.2.27, but for the SI.

Fig. 3.2.33. Same as Fig. 3.2.27, but for the SP.

Fig. 4.1.1. Mean distributions of TC rainfall (unit: mm hr^{-1}) over the a) globe, b) NI, c) WP, d) EP, e) NA, f) SI, and g) SP in the CTL experiment. The directions of x- and y- axis are right and front to TC motion, respectively. The dashed circle indicates the inner-core region of TCs.

Fig. 4.1.2. Spatial distributions of the mean a) RS, and b) RA in the CTL experiment. The mean value in each 5-degree grid box is calculated from the TCs of which centers are located in the grid box. Only grid boxes with sample numbers larger than 20 are presented here.

Fig. 4.1.3. a–b) Zonal and a–b) meridional mean of RS, and RA in the CTL experiment.

Fig. 4.1.4. Monthly distribution of RS over the globe, and the six basins. The 95% significance interval of the mean value is plotted in dark gray.

Fig. 4.1.5. Monthly distribution of RA over the globe, and the six basins. The 95% significance interval of the mean value is plotted in dark gray.

Fig. 4.1.6. Spatial distributions of the mean a) Vmax, b) SST, c) RH700, d) RV850, e) DV850, f) DV250, g) VWS, and h) STEER in the observation. The mean value in each 5-degree grid box is calculated from the TCs of which centers are located in the grid box. Only grid boxes with sample numbers larger than 20 are presented here.

Fig. 4.1.7. Same as Fig. 4.1.6, but for the CTL experiment.

Fig. 4.2.1. Difference of mean a) RS and b) RA between RCP4.5 and CTL experiments (RCP4.5 minus CTL). Changing ratios of RS and RA are provided in c) and d). Only grid points in which the difference is significant in 95% confidence level.

Fig. 4.2.2. Zonal distribution of changes in a) RS and b) RA averaged in the tropics (solid line) and mid-latitudes (dashed line).

Fig. 4.2.3. Future changes in a) Vmax, b) SST, c) RH700, d) RV850, e) DV850, f) DV250, g) VWS, and h) STEER. Arrows indicate the vectors of wind, shear, and steering flow in d–h). Only grid points in which the difference is significant in 95% confidence level.

Fig. 4.2.4. Future changes in winds at a) 850 hPa, and b) 250 hPa level. Only wind vector in which the change is significant in 95% confidence level.

List of Tables

center. The direction of four quadrants are based on the direction of TC motion.

Table 3.2.7. The average vertical wind shear, wind area, rainfall area, and minimum sea level pressure of TCs for the strong and weak shear cases. Statistically significant differences between the two cases for vertical wind shear and rainfall area appear at the 95% confidence level evaluated with Student's *t*-test.

Table 3.2.8. Results of multi-variable linear regression models for the RS and RA over the NI. The R indicates correlation coefficient between the model and observation.

Table 3.2.9. Same as Table 3.2.8, but for the WP.

Table 3.2.10. Same as Table 3.2.8, but for the EP.

Table 3.2.11. Same as Table 3.2.8, but for the NA.

Table 3.2.12. Same as Table 3.2.8, but for the SI.

Table 3.2.13. Same as Table 3.2.8, but for the SP.

Table 4.1.1. Statistics of the RS (unit: mm hr^{-1}) over the globe, and the six ocean basins in the CTL experiment.

Table 4.1.2. Same as Table 4.1.2, but for the RA (unit: 10^5 km^2).

Table 4.2.1. Mean RS and RA in RCP4.5 experiment, and their differences from CTL experiment. Asterisks denote differences significant in 95%

confidence level. Ratio of the difference to the mean value of CTL experiment is provided in parentheses.

List of Acronyms

DV200	Divergence at 200 hPa level
DV850	Divergence at 850 hPa level
EP	Eastern north Pacific
NA	North Atlantic
NI	North Indian
RA	Rainfall Area
RH700	Relative humidity at 700 hPa level
RS	Rainfall Strength
RV850	Relative vorticity at 850 hPa level
SI	South Indian
SP	South Pacific
SST	Sea Surface Temperature
STEER	Steering flow
TC	Tropical Cyclone
V_{max}	maximum wind speed
VWS	vertical wind shear
WP	Western north Pacific

1. Introduction

Tropical cyclones (TCs) are intense cyclonic systems formed over warm tropical oceans and characterized by extreme wind and rainfall. The impact of TCs on humans is enormous both in positive and negative aspects. Rainfall of TCs plays an important role in reducing droughts (Maxwell et al., 2012, Kam et al., 2013), since it accounts for large portion of rainfall extremes and climatology in both the tropics and mid-latitudes (Jiang and Zipser, 2010, Khouakhi et al., 2017). On the other hand, gusty winds and massive rainfall associated with TCs can cause serious economic damages and casualties. In particular, recent studies highlighted that human society is vulnerable to flooding from TC rainfall (Rappaport, 2000, Changnon, 2008, Czajkowski et al., 2011, Rappaport, 2014, Czajkowski et al., 2017). For example, about 90% of deaths by TCs are attributed to drowning (Rappaport, 2014). Czajkowski et al. (2011) also suggested that total fatalities can increase by 28% and 4% as local rainfall and wind speed of TCs increase one-inch and one-knot, respectively. Therefore, accurate forecast of TC rainfall can significantly contribute to prevention of catastrophe incurred by TCs.

TC rainfall has received less attention than TC wind in terms of academic aspects and operational forecasts. Representative characteristics of TCs (i.e., intensity and size) are conventionally defined based on TC wind such as maximum wind speed (V_{max}) and radii of specific wind speed (e.g.,

Knaff et al., 2014, Chan and Chan, 2015, Chavas et al., 2016). A number of operational forecast systems have been developed for intensity and size of TC wind, for example the multi-model and ensemble prediction system in the Regional Specialized Meteorological Center (RSMC) and Tropical Cyclone Warning Centers (TCWCs; Krishnamurti et al., 2010, Krishnamurti et al., 2011, Yu et al., 2013) and the Automated Tropical Cyclone Forecasting System (ATCF; Sampson and Schrader, 2000) in the Joint Typhoon Warning Center (JTWC). Operational TC forecast generally provides only information of track, intensity (i.e., V_{max}), and size (i.e, wind radii) of TCs. Furthermore, predictability of TC wind has been steadily improved, while forecast of TC rainfall has been rarely validated (Peatman et al., 2019).

Understanding characteristics of TC rainfall is preferentially necessary to predict TC rainfall. Fundamentally, TC rainfall is a product of the secondary circulation (i.e., radial and vertical motion), a resultant of the primary circulation (i.e., horizontal and cyclonic motion) and frictions in boundary layer (Smith et al., 2009, Smith and Montgomery, 2010, Montgomery and Smith, 2017). Rainfall is maximized near the center of TC where the upward motion of secondary circulation is the strongest, and rapidly reduced with the radius from the center (Marks et al., 2002, Lonfat et al., 2004, Tuleya et al., 2007). Also, TC rainfall is generally stronger as the primary circulation is stronger (e.g., Rodgers et al., 1994, Lonfat et al., 2004, Jiang et al., 2008a, Lin et al., 2015, Rios Gaona et al., 2018). The relationship between TC rainfall and wind, however, is sharply weakened with increases

in radius from TC center. According to Jiang et al. (2008a), the rainfall rate within 150 km radius from TC center is highly correlated with V_{max} (r = 0.39–0.68), but the relationship is not significant outside a radius of 400 km. These results indicate TC rainfall is not only determined by TC wind.

Characteristics of TC rainfall are also affected by environmental conditions. For example, TC rainfall can be enhanced if sea surface temperature (SST) and humidity increase. This is because they are the major energy source of TCs (e.g., Jiang et al., 2008b, Hill and Lackmann, 2009, Matyas, 2010, Lin et al., 2015). Environmental flows including steering flow and vertical wind shear (e.g., Frank and Ritchie, 1999, 2001, Corbosiero and Molinari, 2002, 2003, Chen et al., 2006b) cause asymmetry of TC rainfall. Large-scale upper-level trough which has effects of angular momentum flux, upper-level divergence, and vertical wind shear (Hanley et al., 2001b, Ritchie and Elsberry, 2003) also plays an important role in changing TC rainfall (e.g., Kim et al., 2006, Kim et al., 2019). Effects of topography also can significantly affect TC rainfall during landfall period (e.g., Chen and Yau 2003; Kimball 2008; Xu et al. 2014).

Although plenty of studies have suggested factors affecting TC rainfall, only a few studies tried to quantitatively investigate the controlling factors utilizing observational data (e.g, Chen and Yau, 2003, Kimball, 2008, Xu et al., 2014). Jiang et al. (2008b) reported that environmental moisture parameters (i.e., total perceptible water, horizontal moisture convergence, and ocean surface moisture flux) account for 26–35% of variability in volumetric

rain (i.e., total volume of rainfall within 5° radius from a TC center) of TCs. According to Lin et al. (2015), the maximum rain rates and rainfall radii of the global TCs increase by ~2.5 mm hr^{-1} and ~100 km, respectively, as relative SST increases 3°C. Most of previous studies have investigated the effect of single factor on TC rainfall. However, TCs are affected by various factors at the same time. Therefore, it is necessary to understand not only the respective effects but also the comprehensive effects of multiple factors on TC rainfall.

The understanding on TC rainfall would be limited due to the lack of observational data. Generally, TCs spend most of their lives over the ocean, which is the major reason for the limited observation of TCs. It is the satellite observation that have made the most significant contributions for understanding the characteristics of TC wind and rainfall. Recently, global climatology of TC wind has been investigated utilizing long-term satellite observations (Liu and Chan, 1999, Chavas and Emanuel, 2010, Chan and Chan, 2012, 2015, Lin et al., 2015, Chavas et al., 2016). In particular, spatial and temporal distributions of TC wind are investigated (e.g., Chan and Chan 2015; Chavas et al. 2016). However, global climatology of TC rainfall such as inter- or inner- basin distributions, and monthly distributions of TC rainfall has not been investigated in detail.

The first goal of this study is to clarify global climatology of TC rainfall using satellite observed precipitation data. A thorough investigation of spatial and temporal distribution of TC rainfall over the globe can suggest basic characteristics of TC rainfall. Understanding the global climatology of TC

rainfall will help to evaluate prediction of TC rainfall and to plan disaster mitigation. The second goal of this study is to understand multiple factors affecting TC rainfall. This approach will improve understanding on mechanisms for variations in TC rainfall and contribute to improvement of TC rainfall forecast. There have been two ways (i.e., statistical and dynamical models) to predict TC rainfall. The most popular statistical model for TC rainfall is the rainfall climatology and persistence model (R-CLIPER; Marks et al., 2002). The R-CLIPER basically assumes rain rate of TC as an exponentially decreasing function over time and radius. The major limitation of R-CLIPER is that the model considers symmetric rainfall structure of TCs and dependency of rainfall on TC intensity (i.e., V_{max}) only. Lonfat et al. (2007) improved the R-CLIPER by including the influence of vertical wind shear and topography on TC rainfall to the model. However, there is an open question whether this model fully takes into account the effects of environments surrounding TCs. Another approach to forecast TC rainfall is high-resolution numerical models. The performance of numerical models for simulating TC rainfall can be significantly improved as the resolutions of models increase (e.g., Fierro et al., 2009; Gentry and Lackmann, 2010; Manganello et al., 2012). However, the latest operational forecast model has systematic errors of TC rainfall, which is attributed to bias of large-scale environments in the model (Peatman et al., 2019). Thus, understanding the factors affecting TC rainfall will help to clarify the causes of errors in TC rainfall prediction and suggest numerical models' weaknesses to be improved.

In addition, this study examined future changes in TC rainfall according to global warming scenario. Global and regional climate is projected to change significantly under global warming (IPCC, 2013). In particular, interest in long-term changes in extreme weather events, such as TCs, heavy rainfall, heat waves, and cold surges, is high in both academia and government. Numerous studies have reported that the genesis, track, and intensity of TCs can change with global warming (e.g., Webster et al., 2005, Bender et al., 2010, Knutson et al., 2010, Park et al., 2017). However, only few studies examined future changes in TC rainfall, since high-resolution numerical models are required to simulate realistic TC rainfall. Several studies have reported that TC rainfall will be enhanced due to increasing SST (e.g., Scoccimarro et al., 2014, Villarini et al., 2014, Lin et al., 2015), but detailed characteristics of TC rainfall have not been investigated. This study utilized the High-resolution Forecast-Oriented Low Ocean Resolution (HiFLOR) model developed by the Geophysical Fluid Dynamics Laboratory (GFDL) to project changes in TC rainfall according to the Representative Concentration Pathway (RCP) 4.5 scenario. The HiFLOR is a high-resolution (i.e., horizontal resolution of 0.25°) atmosphere-ocean coupled global climate model which is developed for seasonal forecasting (Murakami et al., 2016). The HiFLOR has high performance in prediction of TC activity as well as large-scale climate and seasonal variability such as the El Niño–Southern Oscillation (ENSO) phenomenon and its teleconnections (Murakami et al., 2015, Murakami et al., 2016, Zhang et al., 2016, Liu et al., 2018). Therefore,

future changes in TC rainfall under global warming are predicted using the HiFLOR, and possible reasons for the changes are investigated.

This thesis is organized as follows. The Section 2 describes data and methodology used in this study. Characteristics of global TC rainfall in present climate, including spatial- and temporal distributions of TC rainfall, and controlling factors of them, is presented in the Section 3. The Section 4 illustrates changes in TC rainfall projected by the HiFLOR, and possible mechanisms for the future changes. Lastly, the summary and conclusion of this study is suggested in the Section 5.

2. Data and Methodology

2.1. Data

a. TC Information

The International Best Track Archive for Climate Stewardship (IBTrACS) which is a global collection of TC best-track datasets from 1842 to present (Knapp et al., 2010) was used to obtain information of TCs. This data provides information of individual TCs such as the location of TC center (i.e. their latitude and longitude), grade of TC (e.g. tropical depression, tropical storm, and extra-tropical cyclone), maximum wind speed (V_{max}), and minimum sea level pressure (SLP) at 6-hr intervals. In this study, only TCs having maximum wind speed higher than 34 kts, and classified as a tropical storm, severe tropical storm, or typhoon, are investigated. Figure 2.1.1 presents tracks of the TCs over the globe and locations of the six ocean basins investigated in this study. The NI, WP, EP, NA, SI, and SP were used as abbreviations for the North Indian, Western north Pacific, Eastern north Pacific, North Atlantic, South Indian, and South Pacific, respectively.

b. Rainfall Data

The rainfall data analyzed in this study are obtained from the Tropical Rainfall Measuring Mission (TRMM) 3B42 precipitation data retrieved from TRMM and other multi-satellite (Huffman et al., 2007). The TRMM-3B42

have been generally used in previous studies on the TC rainfall due to its high temporal resolution and wide spatial coverage (Jiang and Zipser, 2010, Jiang et al., 2011, Matyas, 2013, 2014, Lin et al., 2015). This dataset also can detect intense TC rainfall reasonably, although it shows higher skills over the ocean than the land (Yu et al., 2009, Chen et al., 2013). The temporal and geographical coverage of this data is from January 1998 to September 2014 and global band from 50°S to 50°N, respectively. Thus, the analysis period was selected as 1998–2013, and the analysis latitude was limited to 50°S–50°N. The temporal and horizontal resolution of this data are 3-hour and 0.25°, respectively. TC rainfall is sampled from this data in every 6 hours along the center of TC in best-track data.

c. Reanalysis and SST Data

To diagnose large-scale environments surrounding TCs, atmospheric sate variables, such as relative humidity, horizontal winds, vertical velocity, and geopotential height were obtained from European Centre for Medium Range Weather Forecast (ECMWF) reanalysis data; ERA-Interim (Dee et al., 2011). From the reanalysis data, vertical wind shear (VWS) is calculated as the difference of winds between 200 and 850 hPa level. Steering flow (STEER), pressure weighted mean winds from 100 and 900 hPa level, is also obtained from these data. The ERA-Interim data is provided from 1979 to present and its horizontal resolution is 0.75°. The SST under TCs is examined by using the daily Optimum Interpolation Sea Surface Temperature version 2

(OISSTv2) (Reynolds et al., 2002). The OISSTv2 is provided from 1982 to present, and its horizontal resolution is 1°. To obtain large-scale environmental conditions without TCs, 20 days low-pass filtering was applied (Fu et al., 2012, Peng et al., 2012). Also, the large-scale environments were averaged within 1,000 km radius from TC center along the track.

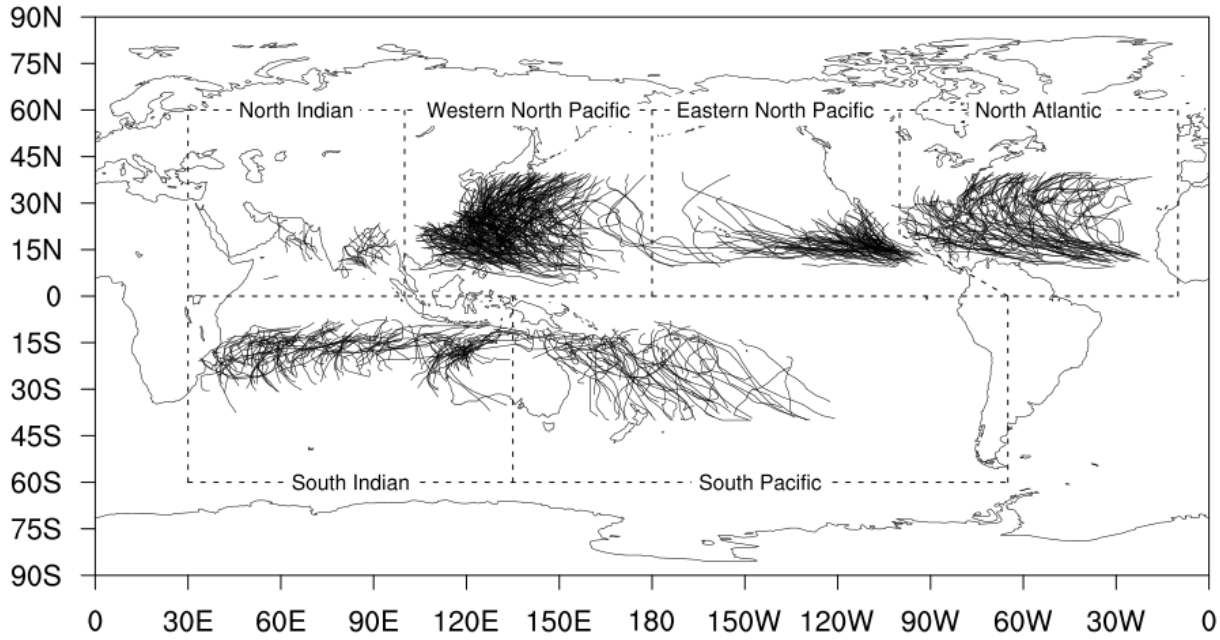

Fig. 2.1.1. Global TC tracks during 1998–2013 and locations of six ocean basins.

2.2. Methodology

a. Rainfall Structure of TCs

This study focus on inner-core rainfall strength (RS), and total rainfall area (RA) of TCs. These two indices represent intensity and spatial scale of TC rainfall, respectively. In general, TC rainfall is maximized near the TC center and weakens with the distance from the center (Marks et al., 2002, Lonfat et al., 2004, Tuleya et al., 2007). Therefore, characteristics of TC rainfall can be expressed by the rainfall intensity near the center and the spatial scale of the overall rainfall. This concept has also been generally applied to wind structure of TCs (e.g., V_{max} and wind radii of 17 m s^{-1}).

The RS is defined as the mean rainfall rate within 100 km radius from the TC center. The algorithm applied to estimate RA is based on the methods used in previous studies (Jiang et al., 2011, Matyas, 2013, 2014, Lin et al., 2015) with a small modification (Fig. 2.2.1). At the beginning of the algorithm, every rain cell within the maximum potential range of TC rainfall area (10° great circle arc from TC center) is identified from the TRMM-3B42 precipitation data for every 6-hour interval of the best-track data. The maximum potential range of TC rainfall area is set large enough to contain most of rain cells that are potentially associated with the TC (Jiang et al., 2011, Lin et al., 2015). Herein, a rain cell is defined as adjacent grid boxes showing precipitation rate in excess of 0.5 mm hr^{-1} (Jiang et al., 2011, Lin et al., 2015). Most of previous studies considered that a rain cell is related with the TC, if

the distance between the rain cell and TC center is less than a specific value (e.g., 500 km in Jiang et al., 2011, Matyas, 2013, 2014). However, such definition of TC rainfall area can be affected sensitively by the criterion of the distance from the TC center. If the distance criterion is too small, TC rainfall area will be underestimated (e.g., supertyphoon Tip in 1974; Merrill, 1984). On the other hand, TC rainfall area will be overestimated if the distance criteria is too large, because rain cells which are irrelevant to TC can be included in TC rainfall area.

This study defines the TC rainfall area using two different criteria of the distance from the TC center. If the minimum distance from a rain cell to the TC center is less than the inner zone criterion (300 km), the rain cell is considered as the TC rain cell. For a rain cell satisfying the outer zone criterion (i.e., the minimum distance from the TC center is in the range of 300–900 km), it is not appropriate to classify the rain cell simply according to the distance from the TC center because mesoscale convective systems other than TC may exist in the outer zone. To distinguish effectively the TC rain cells from non-TC rain cells in the outer zone, rain cells are divided into convective and stratiform cells. A rain cell is classified as convective cell if its maximum precipitation exceeds 5 mm hr^{-1}. This threshold value is similar to precipitation observed in convective cells of TC rain bands (Willoughby, 1988, Houze, 2010) and corresponds to heavy rain threshold for TCs in Jiang et al. (2011). If the cell does not meet this criterion, it is classified as stratiform cell. After classification, each convective cell is traced for every 6-hour

during 4 days (i.e., 2 days forward and 2 days backward). During the tracing process, all convective cells that overlap with the traced cell are identified in the next time step and traced continuously, as the traced cell can merge with other cells or be divided into smaller cells. The traced cell is classified as a TC rain cell if the minimum distance between the overlapping cells and the TC center is less than 900 km for more than 2 continuous days. For stratiform cells, a rain cell is classified as the TC rain cell if it is located in the outer zone. Stratiform cells in the outer zone are not traced because they are usually very small and scattered, and last for only a short period of time. In addition, stratiform cells are found to account for a small part of total TC rainfall area (about 9% on average). Finally, the TC rainfall area is defined as the total area of all TC rain cells passing the algorithm.

Figure 2.2.2 shows a sample of TC rainfall area estimated from the TRMM-3B42 precipitation data. The algorithm developed in this study reasonably captures TC rainfall area located at remote region as well as near the center of TC (Figs. 2.2.2f–j). In addition, the algorithms using the double distance criteria (i.e., DDC; 300 and 900 km) which are adopted in this study, and single distance criterion (i.e., SDC; 500 km) which is applied in the most of previous studies (e.g., Jiang et al. 2011; Matyas et al. 2013, 2014) generally show similar results (Figs. 2.2.2k–o). However, the TC rainfall area calculated by the SDC may significantly change according to the distance criterion. For example, the rainfall area expending northeastward is not included in TC rainfall area of Kammuri at 06 UTC, September 27, 2014

when the SDC is used (Fig. 2.2.2n). Thus, the rainfall area calculated using the SDC is underestimated about 60% compare to that using the DDC at that time (Figs. 2.2.2i and n). Such underestimation of TC rainfall area of using the SDC appears frequently in other TC cases, which makes the TC rainfall area of using the SDC smaller than that of using the DDC about 20% on average (significant in the 95% confidence level). This study analyzed both algorithms, but only the results of applying the DDC algorithm are shown since the overall results are similar; correlation coefficient between TC rainfall areas of the two algorithms is 0.83.

In this study, rainfall asymmetry is also defined by applying the Fourier transform to rainfall area (e.g. Lonfat et al., 2004, Chen et al., 2006a). Figure 2.2.3 shows an example of wave component analysis on TC rainfall area. The RA of a TC can be expressed as the equation (1).

$$A = \int_0^{2\pi} a(\theta)\, d\theta, \quad (1)$$

Here, the upper case 'A' indicates the total RA and the lower case 'a' indicates the RA in azimuthal bins. RA is divided into 36 azimuthal bins and decomposed into wave components in azimuthal direction. Then, the azimuthal RA can be decomposed to some wave components as the equation (2) by applying the Fourier transform.

$$a = a_0 + a_1 \cos(\theta - \theta_1) + a_2 \cos(2\theta - \theta_2) + a_3 \cos(3\theta - \theta_3) + \cdots, \quad (2)$$

The rainfall asymmetry is defined as the ratio of the amplitude of each wavenumber to that of wavenumber zero (i.e. $\frac{a_1}{a_0}, \frac{a_2}{a_0}, \frac{a_3}{a_0}, \frac{a_4}{a_0}, \cdots$).. This study focuses on the wavenumber-1 asymmetry which explains most of variability of the total rainfall area (40.1%).

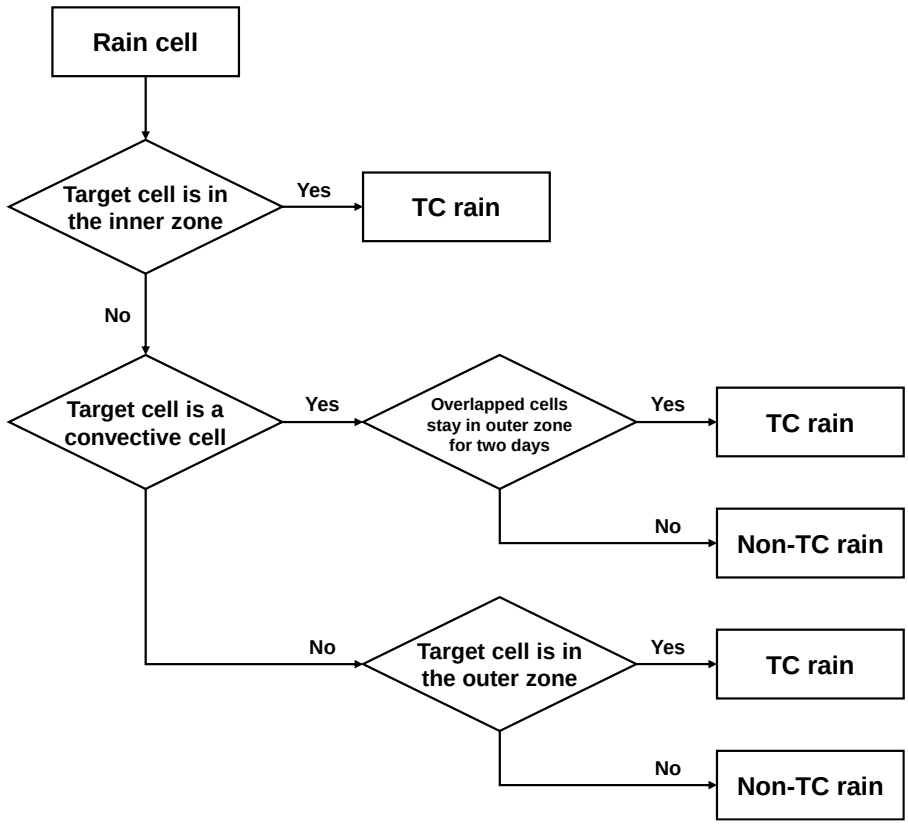

Fig. 2.2.1. Algorithm used to estimate TC rainfall.

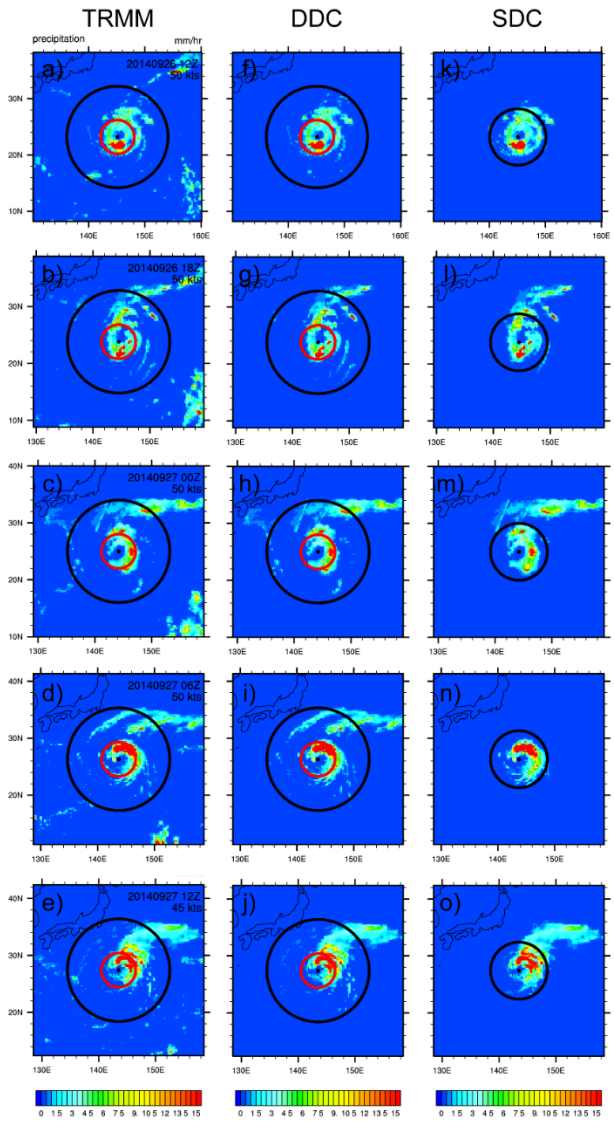

Fig. 2.2.2. Rainfall distribution of TC Kammuri from 12 UTC, September 26, 2014 to 12 UTC, September 27, 2014. The left, middle, and right columns show the a–e) original precipitation data from the TRMM-3B42 data, f–g) TC rainfall area estimated by applying double distance criteria (300 and 900 km; red and black circles, respectively), and k–o) TC rainfall area estimated by applying single distance criteria (500 km; black circle), respectively.

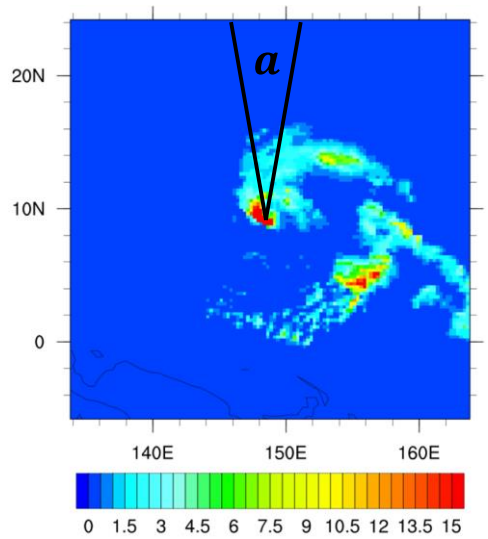

$$A = \int_0^{2\pi} a \, d\theta$$

A: Total rainfall size,
a: Rainfall size in unit angle

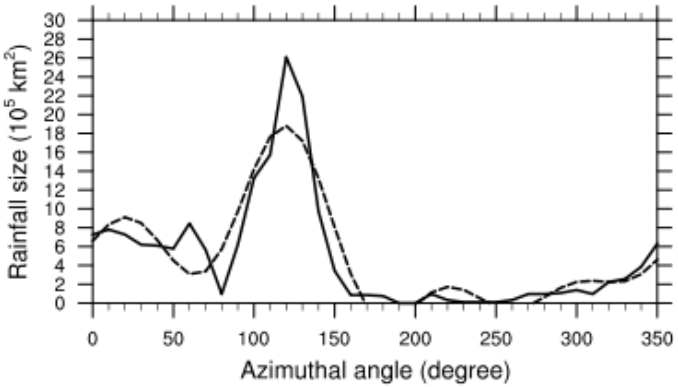

$$a = a_0 + a_1 \cos(\theta - \theta_1) + a_2 \cos(2\theta - \theta_2) + a_3 \cos(3\theta - \theta_3) + \cdots$$

Fig. 2.2.3. A sample of wave component analysis on the rainfall size of a TC. The left figure shows rainfall field of FAXAI (2014) at March 2, 00Z.

b. Factor Analysis

TC rainfall can be affected by multiple environmental conditions which may not be independent of each other. Thus, factor analysis (Woods and Edwards, 2008) is applied to the large-scale environmental conditions to identify independent factors affecting TC rainfall. Factor analysis is a statistical method used to find latent variables, called factors, which explain the common variance of a set of variables examined. The number of potential factors is the same as that of the examined variables. If the number of environmental conditions is 7, the number of potential factors is 7. The correlation between each factor and examined variable is called factor loading. Thus, each factor has 7 factor loadings in the above example. An eigenvalue is the sum of squared factor loadings (i.e., 7 factor loadings) for one factor. All factors are set to be orthogonal to each other and found in the order of eigenvalue. According to the Kaiser criterion, meaningful factor has eigenvalue larger than one.

c. HiFLOR model

HiFLOR has cubed-sphere grid, and physics parameterizations taken from GFDL's Climate Model, version 2.5 (CM2.5; Delworth et al., 2012). The horizontal resolution of HiFLOR is approximately 25 km for atmosphere/land components and 100 km for ocean and ice components. In this study, two experiments performed in Bhatia et al. (2018) were utilized to

investigate future changes in TC rainfall. The control experiment (CTL) represents the observed climate during the period 1986–2005, while the RCP4.5 experiment represents the climate during 2081–2100 under the RCP4.5 scenario (Van Vuuren et al. 2011). HiFLOR was integrated for 70 years in each experiment. During the integration, SSTs were relaxed to the climatological values of the each experiment. In the CTL experiment, the climatological SST was obtained from the Met Office Hadley Centre Sea Ice and SST dataset (HadISST1.1; Rayner et al., 2003) over the years 1986–2005. The RCP4.5 experiment applied the climatological SST of the CTL experiment plus mean SST changes projected by 17 CMIP5 models (ACCESS1.0, ACCESS1.3, CanESM2, CCSM4, CMCC-CM, CSIROMk3.6.0, GFDLCM3, GFDL-ESM2G, GFDLESM2M, GISS-E2-H, GISS-E2-R, HadGEM2-CC, HadGEM2-ES, MIROC-ESM, MIROC-ESM-CHEM, MPI-ESM-LR, and NorESM1-M).

3. Present Characteristics of Tropical Cyclone Rainfall

3.1. Global Climatology of Tropical Cyclone Rainfall

3.1.1. Overview

Understanding spatial and temporal distributions of TC rainfall is required prior to investigating mechanisms for variation of TC rainfall or future changes in TC rainfall. In this section, overall characteristics of TC rainfall over the globe were examined. Figure 3.1.1 shows the mean distributions of TC rainfall over the globe and the six ocean basins. The rainfall composites were obtained in a rotated coordinate system in which the direction of TC motion is oriented due north (i.e., parallel to the y-axis of a rectangular domain). Regardless of the basin, TC rainfall is maximized in the inner-core region (i.e., area within 100 km from the center; dashed circle in Fig. 3.1.1) and decreases with the radius from TC center. Thus, RA is closely related to rainfall structure in outer region of TC. Outside the inner-core, distributions of TC rainfall are generally symmetric (i.e., circular shape) except the NI and SP.

The intensity and spatial scale of TC rainfall are examined based on RS and RA. Table 3.1.1 and 3.1.2 present statistics of RS and RA for the globe and the six ocean basins. The global mean of RS, and RA are 4.43 mm hr^{-1}, and 4.75×10^5 km^2, respectively. The global mean RS in this study is similar

to maximum rainfall rates of TCs (i.e., approximately 4–6 mm hr^{-1}) reported in previous studies (e.g., Lonfat et al., 2004, Jiang et al., 2008a, Rios Gaona et al., 2018). Note that the standard deviations of RS, and RA over the globe are 3.52 mm hr^{-1}, and 3.10×10^{5} km^{2}, respectively. The ratios of mean to standard deviations of RS, and RA over the globe are 0.79, and 0.65, respectively. This indicates wide dispersion of RS, and RA, which is commonly observed in each ocean basin. RS and RA also distinctly vary according to ocean basin. The mean RS is large in order of the WP, SP, NI, SI, NA, and EP. The mean RS of the WP is about 1.4 times larger than that of the EP. Similarly, the mean RA is large in order of the SP, WP, NI, SI, NA, and EP. The mean RA of the SP is about 1.8 times larger than that of the EP. The 25, 75 percentile, and median of RS, and RA also vary by basins in a similar fashion to the mean value.

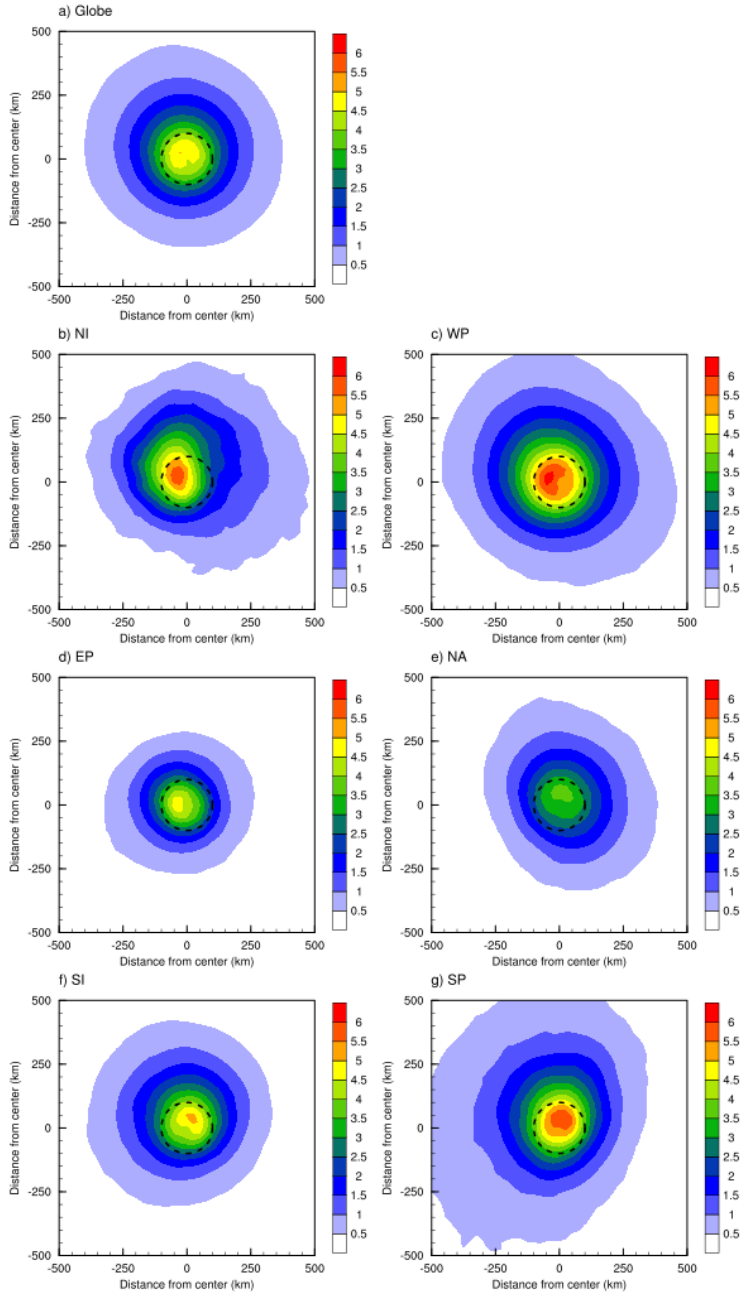

Fig. 3.1.1. Mean distributions of TC rainfall (unit: mm hr^{-1}) over the a) globe, b) NI, c) WP, d) EP, e) NA, f) SI, and g) SP. The directions of x- and y- axis are right and front to TC motion, respectively. The dashed circle indicates the inner-core region of TCs.

Table 3.1.1. Statistics of the RS (unit: mm hr^{-1}) over the globe, and the six ocean basins.

	Mean	Standard deviation	25%	median	75%
Global	4.43	3.52	1.90	3.68	6.03
NI	4.32	3.73	1.70	3.49	5.95
WP	5.22	3.77	2.58	4.47	6.98
EP	3.62	2.87	1.56	2.99	4.89
NA	3.94	3.40	1.50	3.17	5.41
SI	4.18	3.26	1.78	3.55	5.77
SP	4.86	3.90	2.07	4.10	6.62

Table 3.1.2. Same as Table 3.1.1, but for the RA (unit: 10^5 km^2).

	Mean	Standard deviation	25%	median	75%
Global	4.75	3.10	2.40	4.10	6.48
NI	4.67	2.73	2.57	4.21	6.38
WP	5.86	3.29	3.40	5.32	7.45
EP	3.49	2.54	1.44	2.98	5.01
NA	3.70	2.35	1.96	3.23	4.90
SI	4.39	2.79	2.26	3.80	5.89
SP	6.45	3.56	3.65	5.97	8.66

3.1.2. Spatial Distribution

Variability of TC rainfall is large not only between but also within the basins. Figure 3.1.2 illustrates spatial variations of mean RS and RA. It was noted that local maxima of the mean RS and RA appear near the Madagascar, Warm pool over the WP and SP, and Central America regions. These regions generally show high SST, and active tropical convections, which is favorable for TC development. The spatial distributions of RS and RA has not been exactly reported in previous studies. Most studies examined mean characteristics of TC rainfall in global or individual ocean basins. Only a few studies investigated spatial distribution of TC rainfall over the globe. For example, Jiang and Zipser (2010), Jiang et al. (2011), Skok et al. (2013) reported spatial distribution of monthly accumulated precipitation related with TCs which is similar to the distributions of RS and RA. On the other hand, Chavas et al. (2016) showed spatial distribution of wind radii of 12 m s^{-1} which generally increase with latitude, which is significantly different to the spatial distribution of TC rainfall.

Spatial distributions of RS and RA averaged in zonal and meridional directions are shown in Fig. 3.1.3. Generally, RS and RA present similar spatial distributions. For example, RS and RA are the largest in the tropics and decrease with latitude (Figs. 3.1.3a and 3.1.3b). The variations of RS and RA in the west-east direction also resemble each other (Figs. 3.1.3c and 3.1.3d). However, some detailed features of the spatial distributions of RS and RA are different. In the mid-latitudes (i.e., higher than 30°N) of the

Northern Hemisphere, RS slightly decreases but RA significantly increases with latitude, respectively. The local maxima of RS appear near 150, 260, and 290°E, while those of RA appear near 60, 180, and 270°E. Possible reasons for the large variations of RS and RA in space will be discussed in Section 3.2.

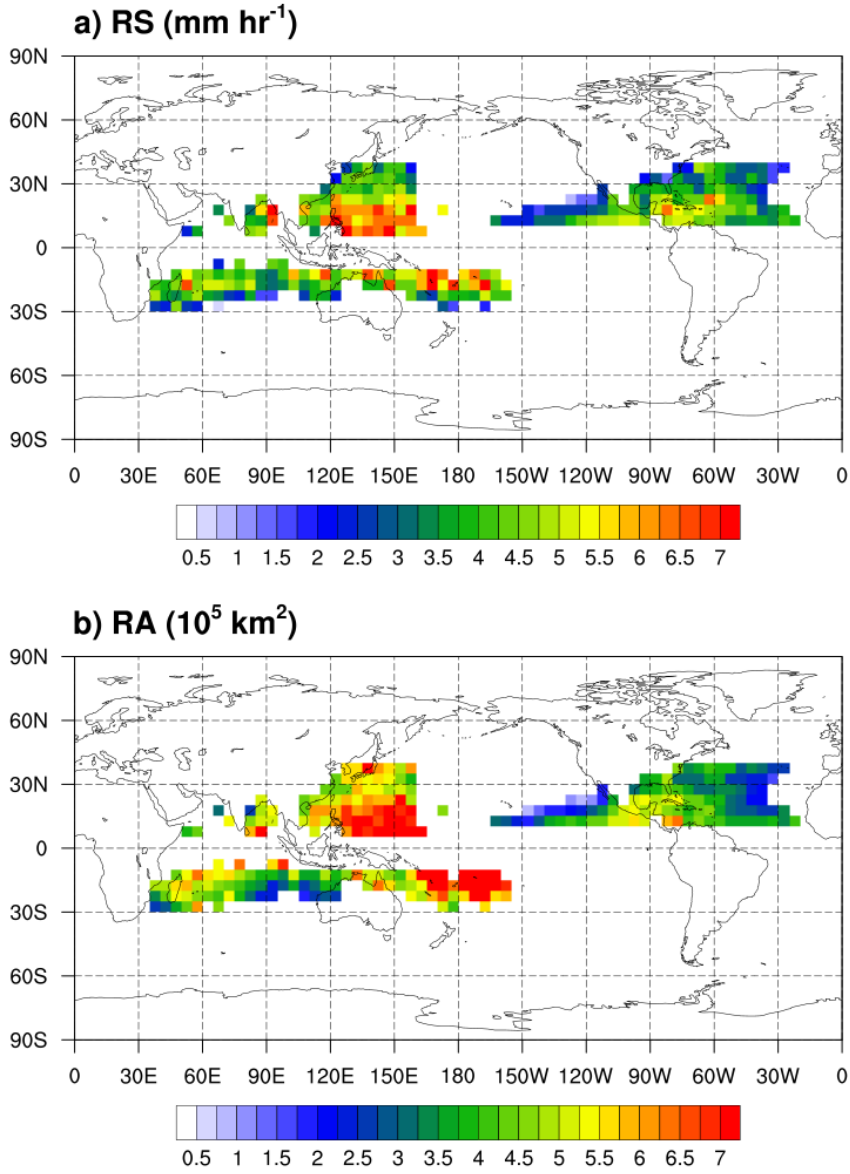

Fig. 3.1.2. Spatial distributions of the mean a) RS, and b) RA. The mean value in each 5-degree grid box is calculated from the TCs of which centers are located in the grid box. Only grid boxes with sample numbers larger than 20 are presented here.

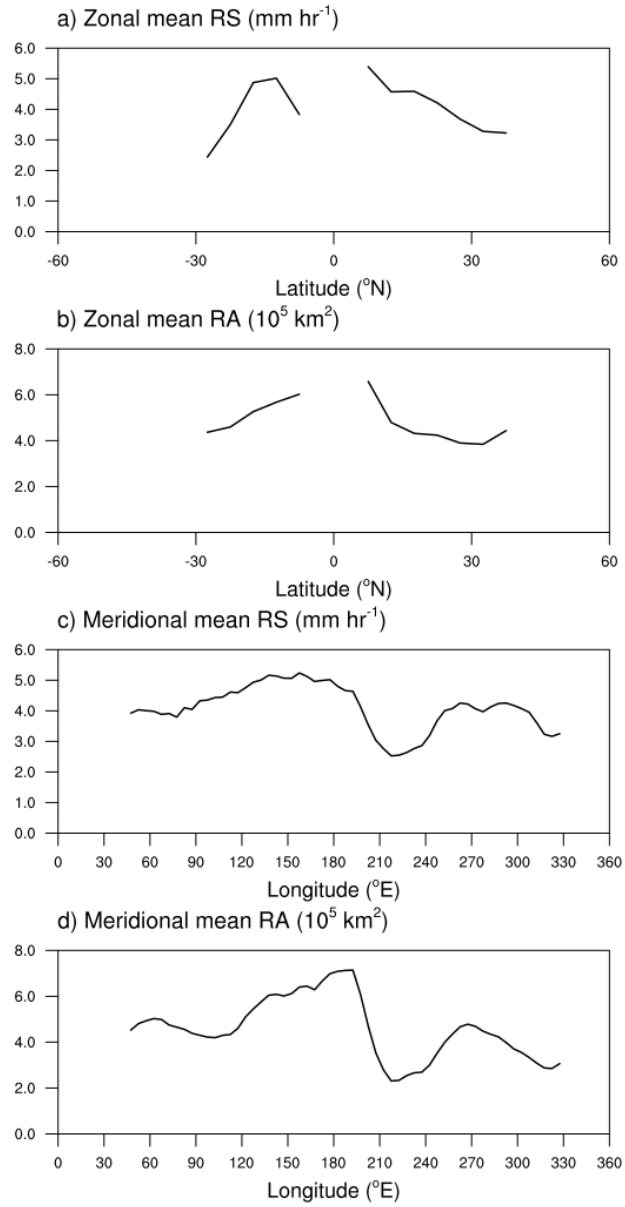

Fig. 3.1.3. a–b) Zonal and a–b) meridional mean of RS, and RA.

3.1.3. Temporal Distribution

Monthly and yearly variations of RS and RA were investigated in this section. Figures 3.1.4 and 3.1.5 show monthly mean RS and RA over the globe and the six ocean basins, respectively. Globally, RS shows very small variation according to the month, and has two peaks in April (4.88 mm hr^{-1}) and December (4.65 mm hr^{-1}). Monthly variation of RA is more pronounced than that of RS over the globe. Global mean RA has three peaks in January (5.20×10^5 km^2), June (5.44×10^5 km^2), and November (4.94×10^5 km^2). In the NI, TC activity occurs in two period of April–June and September–December. The RS in early period is about 1.3 times larger than that in late period, while the difference of RA between two periods is not significant. In the WP, RS shows two peaks in April (6.45 mm hr^{-1}) and December (6.13 mm hr^{-1}), while RA shows one peak in June (6.84×10^5 km^2). Monthly variations of RS and RA in the EP are not clear from May to November. The NA presents the largest monthly variations of RS and RA. The maximum RS appears in September (4.30 mm hr^{-1}), and maxima of RA appear in June (4.73×10^5 km^2) and November (4.98×10^5 km^2). In the SI, RS is maximized in March (4.30 mm hr^{-1}), but the seasonality of RA is not clear. The RS and RA in the SP are maximized in December (5.91 mm hr^{-1} and 7.26×10^5 km^2, respectively) and show weak monthly variations.

Annual variations of RS and RA are insignificant globally, but RS presents significantly decreasing trend with time (Figs. 3.1.6 and 3.1.7). The slope is –0.081 mm hr^{-1} yr^{-1}, which corresponds to –1.8% yr^{-1} relative to the

global mean RS. Decreasing trends of RS were also found in the EP, NA, and SI. The slopes in the EP, NA, and SI are –0.062, –0.141, and –0.071 mm hr^{-1} yr^{-1} (corresponding to –1.7, –3.6, and –1.7% yr^{-1} relative to the mean RS in each basin), respectively. The RS in the NI, WP, and SP show insignificant tendency with time. On the other hand, the NI, and SP show larger annual variations of RS than other basins. Also, there are no linear trends of RA over the globe and each basin (Fig. 3.1.7). Similar to the RS, annual variations of RA in the NI, and SP are larger than those of other basins.

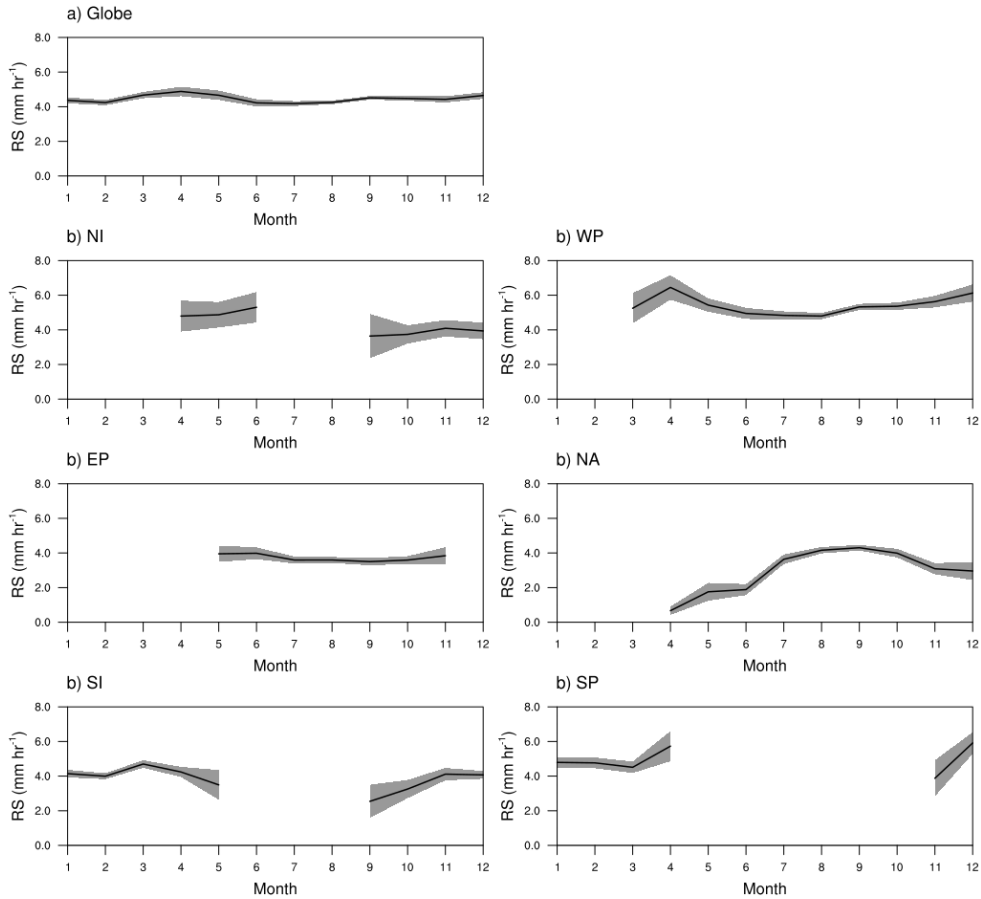

Fig. 3.1.4. Monthly distribution of RS over the globe, and the six basins. The 95% significance interval of the mean value is plotted in dark gray.

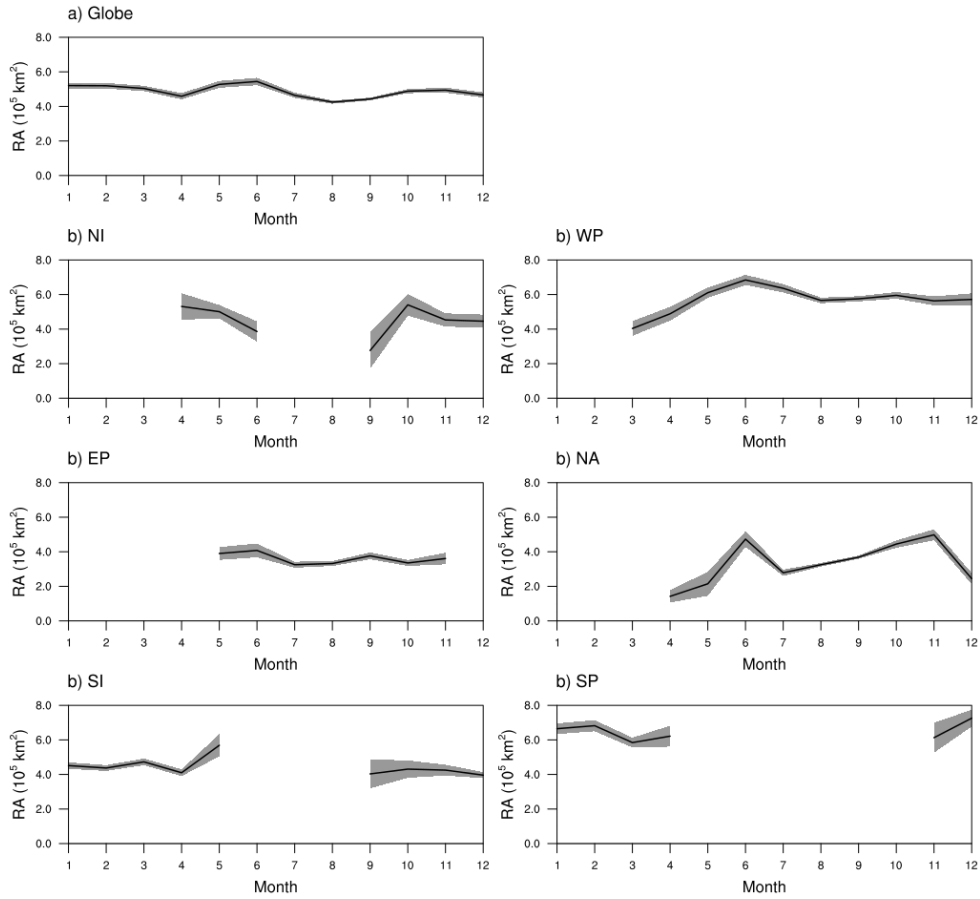

Fig. 3.1.5. Same as Fig. 3.1.4, but for the RA.

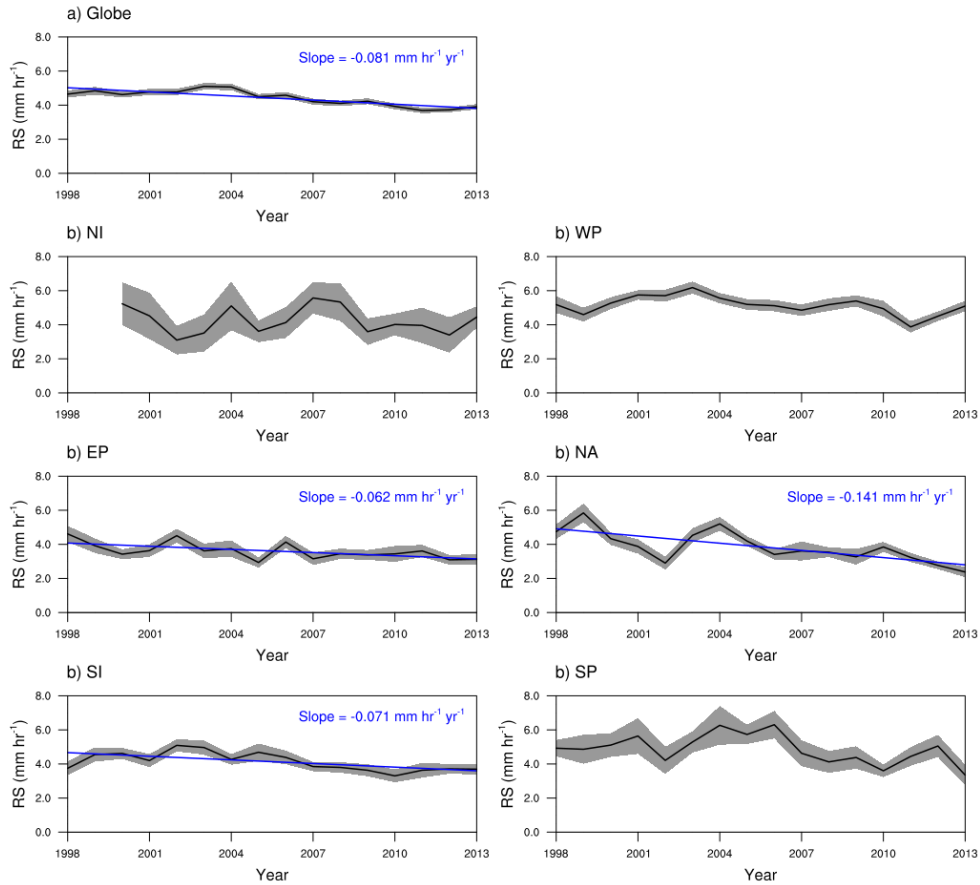

Fig. 3.1.6. Yearly distribution of RS over the globe, and the six basins. The 95% significance interval of the mean value is plotted in dark gray. Blue lines indicate linear regression lines of which slope is significant in 95% confidence level.

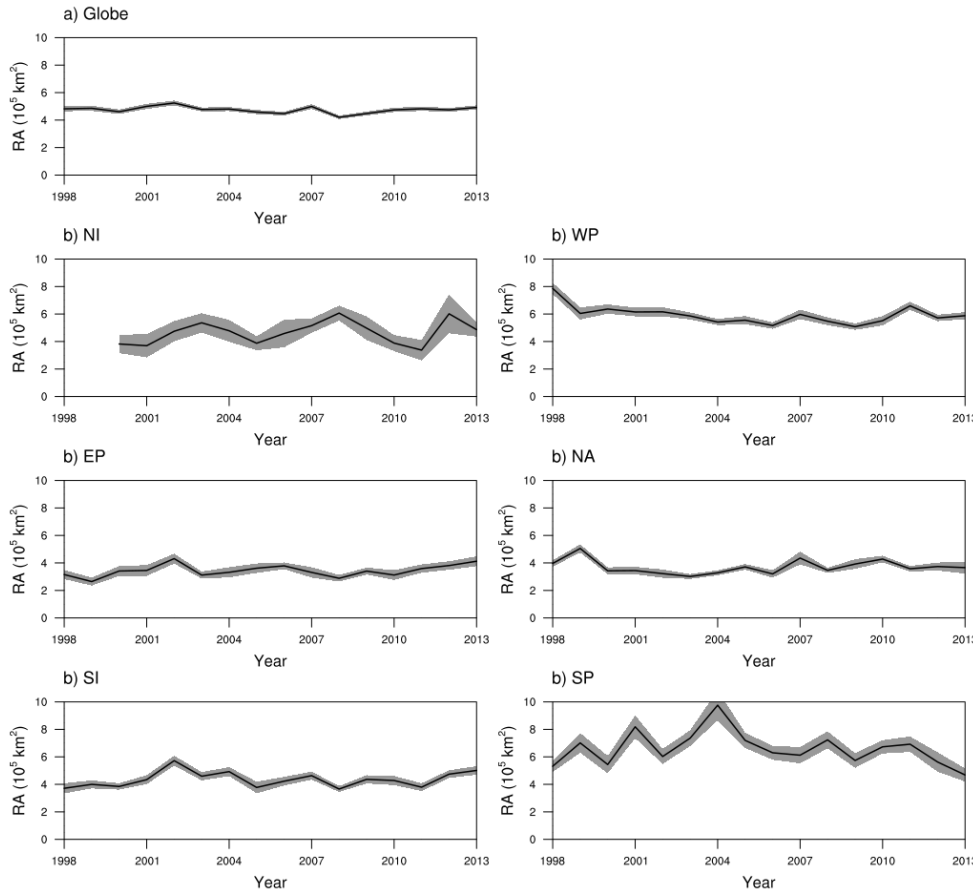

Fig. 3.1.7. Same as Fig. 3.1.6, but for the RA.

3.2. Factors Controlling Tropical Cyclone Rainfall

Rainfall strength and area of tropical cyclones have large variation according to time and space (Section 3.1). In this section, various factors related to the variations of TC rainfall were investigated. Theoretical models and previous observations of TC rainfall suggested that wind and rainfall structures of a TC are closely related together (Section 1). Also, characteristics of a TC can be significantly affected by environmental conditions surrounding the TC. Thus, the relationship between TC rainfall and the primary circulation was revisited first. Then, the influence of multiple environmental conditions on TC rainfall was examined. The non-linear relationships between TC rainfall and environmental conditions, particularly for environmental flows and SST, were also covered in this section. Finally, a statistical model for TC rainfall is developed based on the understanding of the major factors controlling TC rainfall.

3.2.1. Primary Circulation

The primary circulation of a TC, horizontal and cyclonic circulation, approximately satisfies gradient wind balance where pressure gradient, centrifugal, and Coriolis forces are in equilibrium. When the gradient wind balance is broken due to the friction in boundary layer, inflow toward the center of TC is induced. The converged air at the center of TC rises and reaches the upper troposphere. In the upper troposphere, air diverges from the

center of TC. This radial and vertical circulation is called the secondary circulation which induces precipitation of TCs. The stronger the primary circulation, the stronger the secondary circulation. Thus, TC rainfall and the primary circulation can be tightly related. Conventionally, the strength of primary circulation is represented by the V_{max}. Therefore, this section investigates the variation of TC rainfall according to the V_{max}.

Figure 3.2.1 shows the mean distributions of TC rainfall according to the magnitude of V_{max}. The rainfall in the inner-core region (i.e., area within 100 km from the center) clearly increases with the V_{max}, while the variation of rainfall in the outer region is relatively small than that in the inner-core. Table 3.2.1 present the variations of RS and RA according to the V_{max}. The mean RS remarkably increases with the V_{max}. The mean RS increases about 2.6 times from the lower 25 percentile to higher 75 percentile of V_{max}. Also, the increase of RS in each bin of V_{max} quartile is statistically significant. On the other hand, the mean RA increases only about 1.2 times from the lower 25 percentile to higher 75 percentile of V_{max}. The increase of RA according to V_{max} is statistically significant but its magnitude is much smaller than that of RS. The relationship between TC rainfall and the primary circulation is suggested in Table 3.2.2. Regardless of the basin, RS show robust relationship with V_{max} (r = 0.32–0.62), while the relationship between RA and V_{max} is weak (r = 0.01–0.17). The relationships of V_{max} with RS and RA are the strongest in the NA and weakest in the NI, respectively.

Overall results demonstrate that RS is significantly related to V_{max}, while the RA is not. In other words, the primary circulation mainly affect TC rainfall in the inner-core. The vertical motion of the secondary circulation is concentrated in a very narrow region near the center of TC. Thus, rainfall in the inner-core can be more strongly affected by the primary and secondary circulation than other factors. Meanwhile, the air rising from the center of the TC spreads in the upper troposphere and forms anvil clouds. A large proportion of rainfall in the outer region of the TC originates in these anvil clouds (Houze, 2010). The weak relationship between the RA and the primary circulation suggests that rainfall in the outer region of the TC may be more affected by factors (i.e., environmental conditions) other than the primary circulation. This will be discussed in detail in the next section.

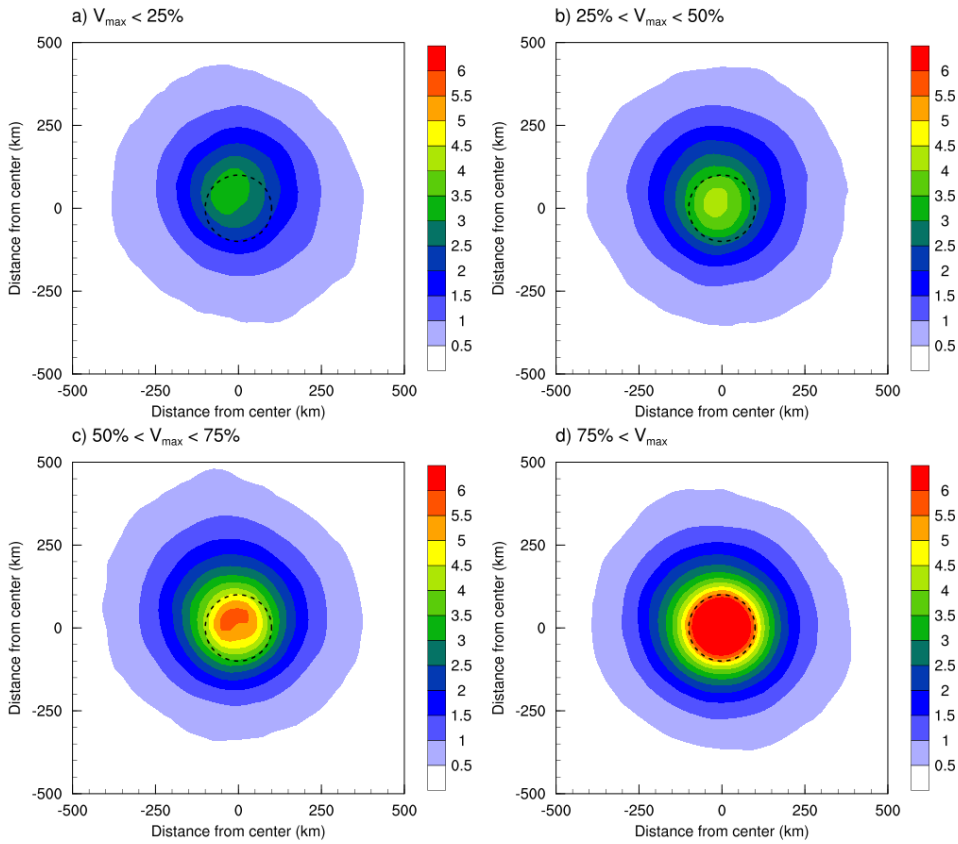

Fig. 3.2.1. Mean distributions of TC rainfall (unit: mm hr^{-1}) according to the quartile bins of V_{max}. The directions of x- and y- axis are right and front to TC motion, respectively. The dashed circle indicates the inner-core region of TCs.

Table 3.2.1. Mean RS and RA according to the quartile bins of V_{max}. The 95% significance intervals of the mean value are provided in parentheses.

		RS (mm hr^{-1})	RA (10^5 km^2)
V_{max}	< 25%	2.66 (±0.067)	4.26 (±0.075)
	25–50%	3.54 (±0.073)	4.61 (±0.075)
	50–70%	4.81 (±0.084)	4.80 (±0.082)
	< 75%	6.91 (±0.103)	5.29 (±0.084)

Table 3.2.2. Pearson's correlation coefficients between TC rainfall (i.e., RS, and RA) and V_{max} over the globe and six ocean basins. Asterisks indicate correlation coefficients significant in 95% confidence level.

	RS	RA
Globe	0.47*	0.13*
NI	0.32*	0.01
WP	0.42*	0.07*
EP	0.41*	0.07*
NA	0.62*	0.17*
SI	0.46*	0.09*
SP	0.38*	0.17*

3.2.2. Influence of Large-scale Environments

In this section, the relationships between TC rainfall and multiple environmental conditions along the TCs were investigated. The multiple environments investigated in this study are SST, relative humidity at 700 hPa (RH700), relative vorticity at 850 hPa (RV850), divergence at 850 and 200 hPa (DV850 and DV200), vertical wind shear between 850 and 200 hPa level (VWS), and steering flow (i.e., pressure weighted mean winds from 900 to 100 hPa level; STEER). All of these environments were suggested to affect key characteristics of a TC; rainfall as well as genesis, track, and intensity (e.g., Gray, 1968, Frank and Ritchie, 1999, Hanley et al., 2001b, Chen et al., 2006b, Jiang et al., 2008b, Hill and Lackmann, 2009). In addition, environmental conditions may not be independent of each other, which makes it difficult to interpret their comprehensive effects on TC rainfall. Thus, we applied factor analysis to the large-scale environmental conditions to identify independent factors affecting TC rainfall.

a. One to One Relationships between TC Rainfall and Environmental Conditions

The relationships between TC rainfall and the seven environmental conditions over the globe are provided in Table 3.2.3. Globally, RS has significant relationships with SST, RH700, DV850, DV200, and VWS, but those relationships are much weaker than the relationship between RS and V_{max} (Section 3.2.1). High SST and RH700 surrounding a TC can increase

RS, since they provide sensible and latent heat to the TC. In addition, large-scale lower convergence and upper divergence can enhance the vertical circulation of TCs (Hanley et al. 2001), which is favorable condition to increase RS. On the other hand, VWS is a major factor inhibiting TC development, because it reduces heat and moisture of TCs by the ventilation effect (Jones, 1995, DeMaria, 1996). Therefore, RS also weakens along with the weakening of the TC.

On the other hand, RA present the strongest relationship with DV850, and DV200. In other words, large-scale vertical circulations associated with DV850 and DV200 may have the largest contribution to the increase of RA by expanding the anvil cloud of a TC. Also, RA has robust relationship with SST, RH700, and RV850. The variation of RA can be associated with SST and RH700, since they are the major sources of TC rainfall. The correlation coefficient between the RA and SST is statistically significant in 95% confidence level but only 0.24. Several studies showed that TC rainfall is intensified as SST increases (e.g., Scoccimarro et al., 2014, Villarini et al., 2014, Lin et al., 2015), but the correlation coefficient between the RA and SST has not been reported in previous studies. Our result suggests that SST can increase RA, but the contribution of SST to changes in RA is much smaller than that of DV850 and DV200. Large-scale RV850 also enhances the cyclonic circulation of TCs by supplying angular momentum to the TC (Hanley et al., 2001), thus facilitating TC rainfall. In contrast to RS, the relationship between RA and large-scale environmental conditions is stronger

than that between RA and V_{max}. This result indicates that rainfall in the outer region of the TC is more sensitive to the influence of large-scale environments than the primary circulation.

Similar to the globe, the relationships between RS (RA) and the seven environmental conditions for the six ocean basins are investigated (Figs. 3.2.2, and 3.2.3). The relationship between RA and large-scale environments (i.e., SST, RH700, RV850, DV850, and DV200) is robust, while that of RS is relatively weak. The relationship between RV850 and RA is negative in the South Hemisphere, since the sign of vorticity for cyclonic circulation is reversed. Such relationships between TC rainfall and environmental conditions are found consistently in all basins, although there are some differences between ocean basins.

Table 3.2.3. Pearson's correlation coefficients between TC rainfall (i.e., RS, and RA) and multiple environmental conditions over the globe. Asterisks indicate correlation coefficients significant in 95% confidence level.

	RS	RA
SST	0.22*	0.24*
RH700	0.14*	0.36*
RV850	0.07*	0.27*
DV850	–0.17*	–0.52*
DV200	0.16*	0.57*
VWS	–0.11*	0.07*
STEER	–0.003*	0.06*

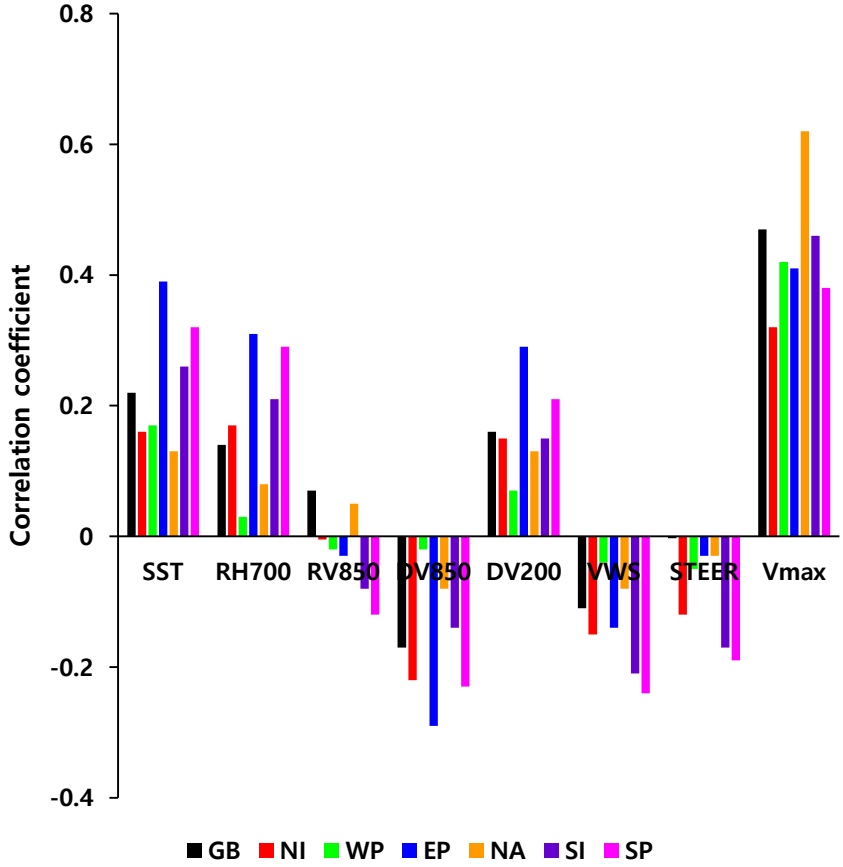

Fig. 3.2.2. Correlation coefficients between RS and multiple parameters (i.e., SST, RH700, RV850, DV850, DV200, VWS, STEER, and V_{max}) for the globe (GB; black bars) and individual ocean basins (NI, WP, EP, NA, SI, and SP; red, green, blue, orange, purple, and pink, respectively).

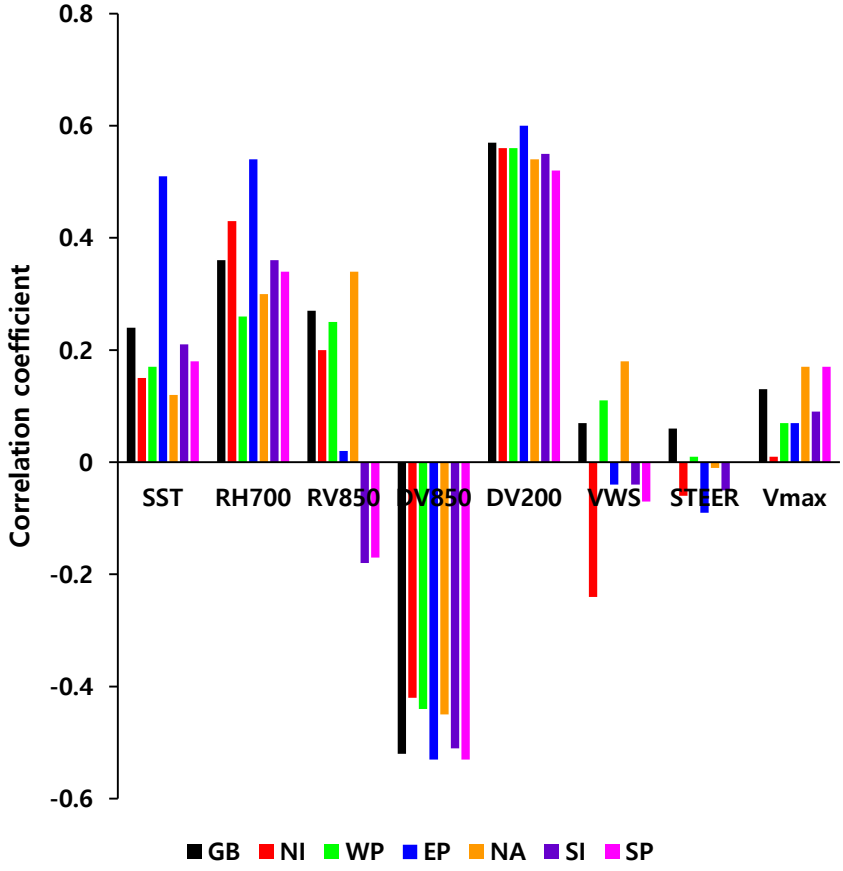

Fig. 3.2.3. Same as the Fig. 3.2.2, but for the RA.

b. Major Factors Affecting TC rainfall

Large-scale environments related to the variations of TC rainfall are not completely independent each other. To identify comprehensive influence of large-scale environments, factor analysis to the seven environmental conditions and V_{max} is applied for each ocean basins. As shown in the previous section, V_{max} can control TC rainfall but its relationship with environmental conditions was not investigated. Thus, V_{max} is also included in the factor analysis. It was noted that there are three meaningful factors which have eigenvalue larger than 1 regardless of region (Fig. 3.2.4). The ratio of explained variance by these three factors is 65.2–78.0% for the six basins.

In most regions, Factor 1 (F1) has significant relationships with DV200, DV850, RV850, RH700, and SST (Fig. 3.2.5). The relationship between F1 and RV850 is positive and negative in the North and South Hemisphere, respectively. Thus, larges-scale cyclonic circulation is enhanced as F1 increases. At the same time, F1 has positive and negative relationship with DV200 and DV850, respectively, which indicates large-scale upward motion is promoted when F1 is high. RH700 and SST also increases as F1 increases. Such relationships between F1 and large-scale environmental conditions means that F1 is related to the variations in large-scale low (or high) pressure systems.

Factor 2 (F2) generally has positive relationships with VWS, and STEER, while it is negatively related to SST (Fig. 3.2.6). In other words, environmental flows (i.e., VWS, and STEER) strengthen when SST decreases.

Such relationship can be associated with climatological distributions of VWS, STEER, and SST in space and time. For example, SST generally decreases but VWS and STEER increase as latitude increases. Similar variations of those environments appear when the seasons change from summer to winter. Thus, the F2 explains changes in environmental flows accompanied with SST.

Lastly, the Factor 3 (F3) is mainly related to the V_{max} (Fig. 3.2.7). In other words, V_{max} is an independent variable for the seven environmental conditions. Generally, V_{max} increases and decrease as a TC develops and decays, which is different to the variations of environmental conditions. For example, SST is very high in early stage of TCs, since TCs are generated over warm tropical oceans. Then, SST gradually decreases if a TC recurves to mid-latitudes. Therefore, V_{max} seems to have a weak linear relationship with other environmental conditions.

Based on the results from factor analysis, relationships between TC rainfall (i.e., RS and RA) and the three major factors were investigated (Figs. 3.2.8–3.2.13). It was noted that RS generally presents significantly positive relationship with the F3. Relationships between RS and other factors are relatively weak and insignificant except the EP. RS presents significantly positive relationship with F1 only in the EP. Thus, RS is mainly determined by the strength of primary circulation (i.e., V_{max}; F3) rather than large-scale environments. In contrast, RA has significantly positive relationship with the F1 regardless of region. Large F1 means that large-scale low pressure system with high humidity, positive vorticity, convergence in lower troposphere, and

divergence in upper troposphere affects TCs, which is a favorable condition for large RA. Also, positive relationship between the RA and the F2 appears strong in the north-west quadrant of NA and north-east quadrant of WP (Figs. 3.2.9d and 3.2.11d) where the environmental flows are strong and significantly vary. This result implies that the relationship between TC rainfall and environmental flows may changes according to other factor (e.g., region, development stage of a TC, and etc.). Such non-linear relationships between TC rainfall and environmental flows will be discussed in the next section. RA also shows positive relationship with the F3 only in the mid-latitudes above 25°N (Figs. 3.2.9f and 3.2.11f). Therefore, F1 (i.e., large-scale low or high pressure systems) primarily affect RA, while F2 (i.e., environmental flows, and SST), and F3 (i.e., V_{max}) partially contribute to the variation of RA.

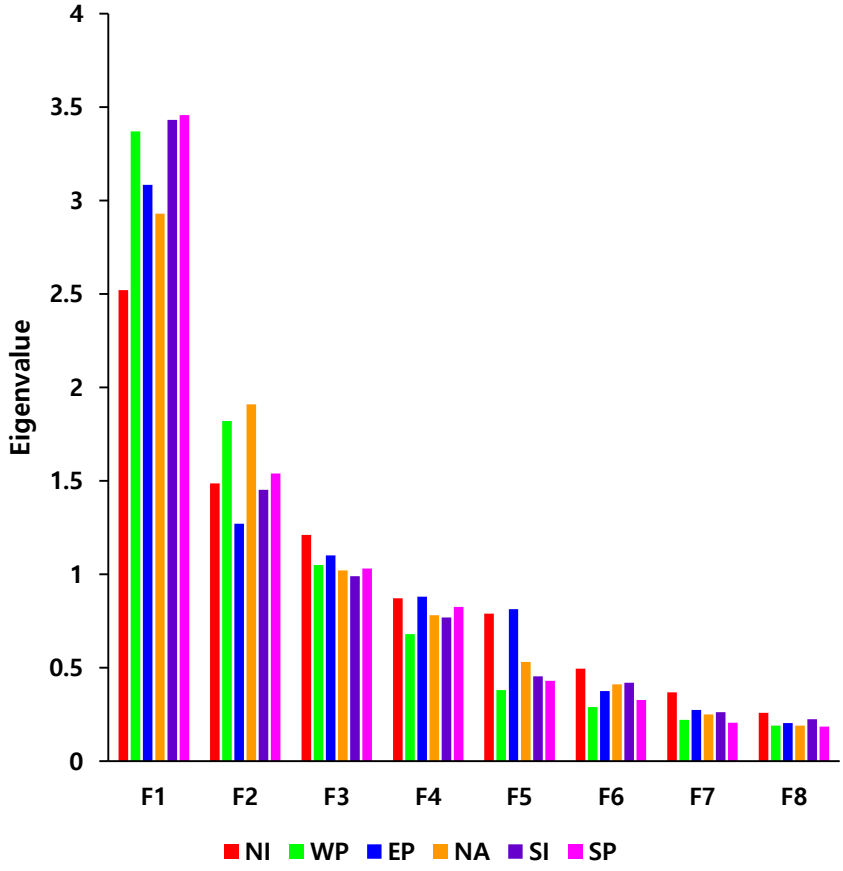

Fig. 3.2.4. Eigenvalue of the eight factors (i.e., F1–F8) for the six ocean basins. Eigenvalue means total sum of squared factor loadings which are the correlation coefficients between factor and analyzed variables.

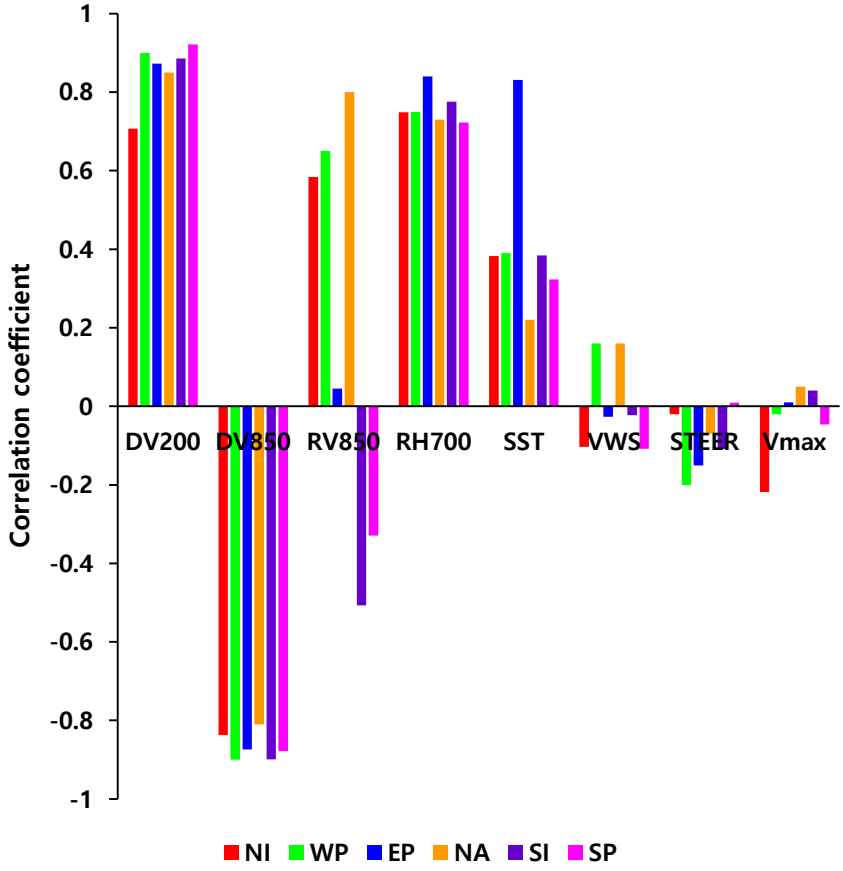

Fig. 3.2.5. Correlation coefficients between F1 and multiple parameters (i.e., SST, RH700, RV850, DV850, DV200, VWS, STEER, and V_{max}) for the six ocean basins.

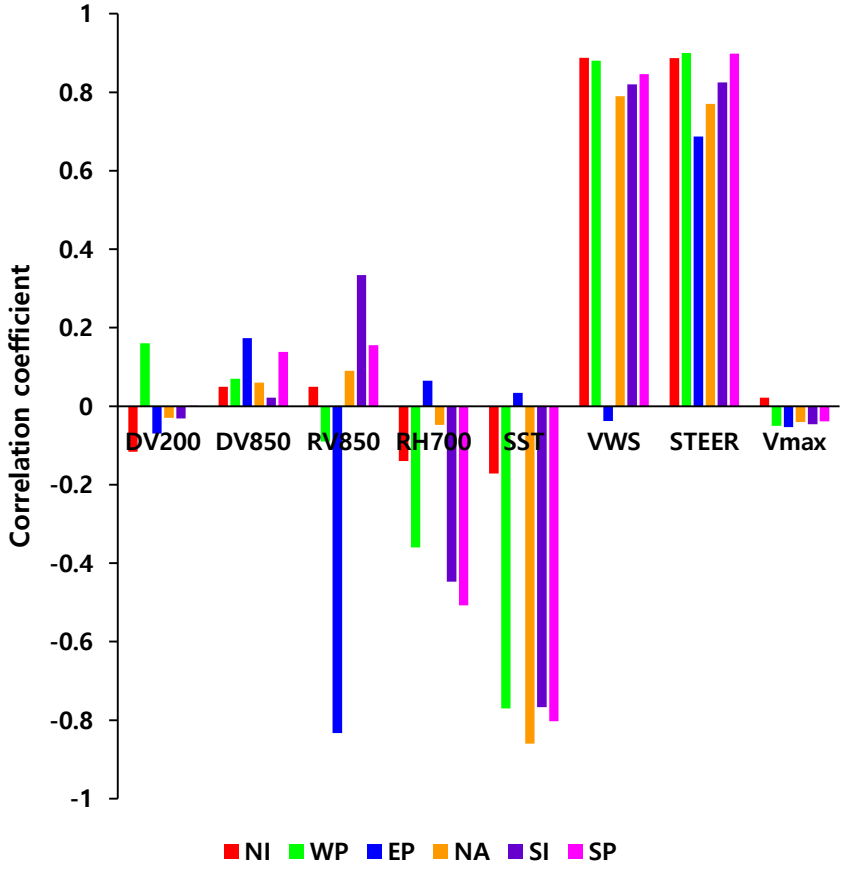

Fig 3.2.6. Same as the Fig 3.2.4, but for the F2.

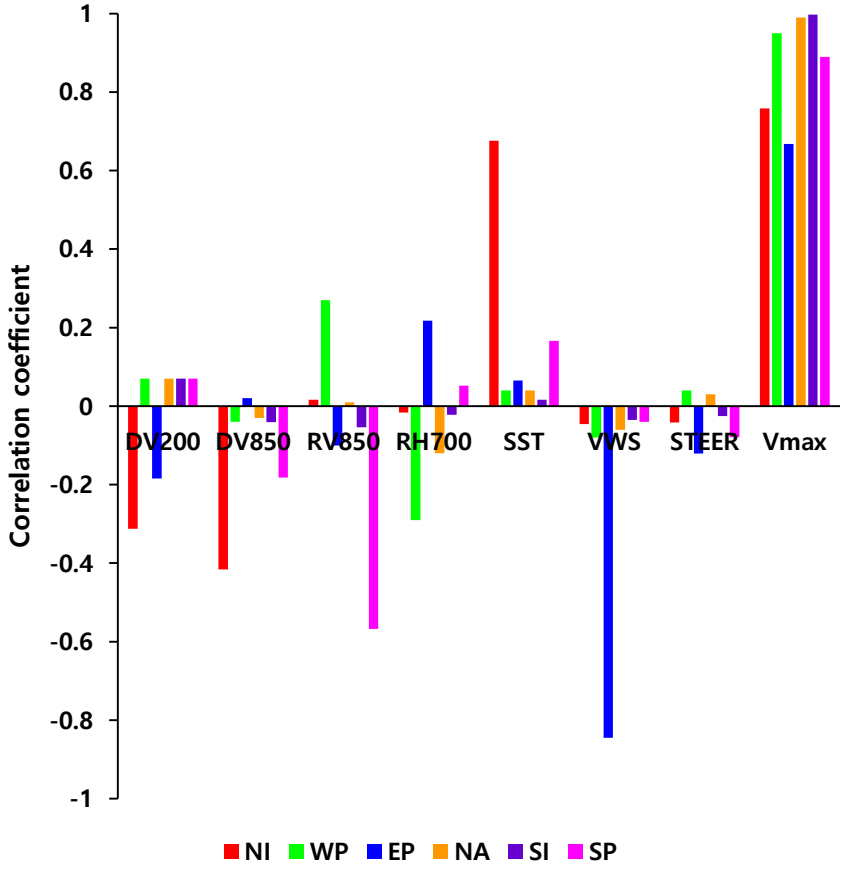

Fig 3.2.7. Same as the Fig 3.2.4, but for the F3.

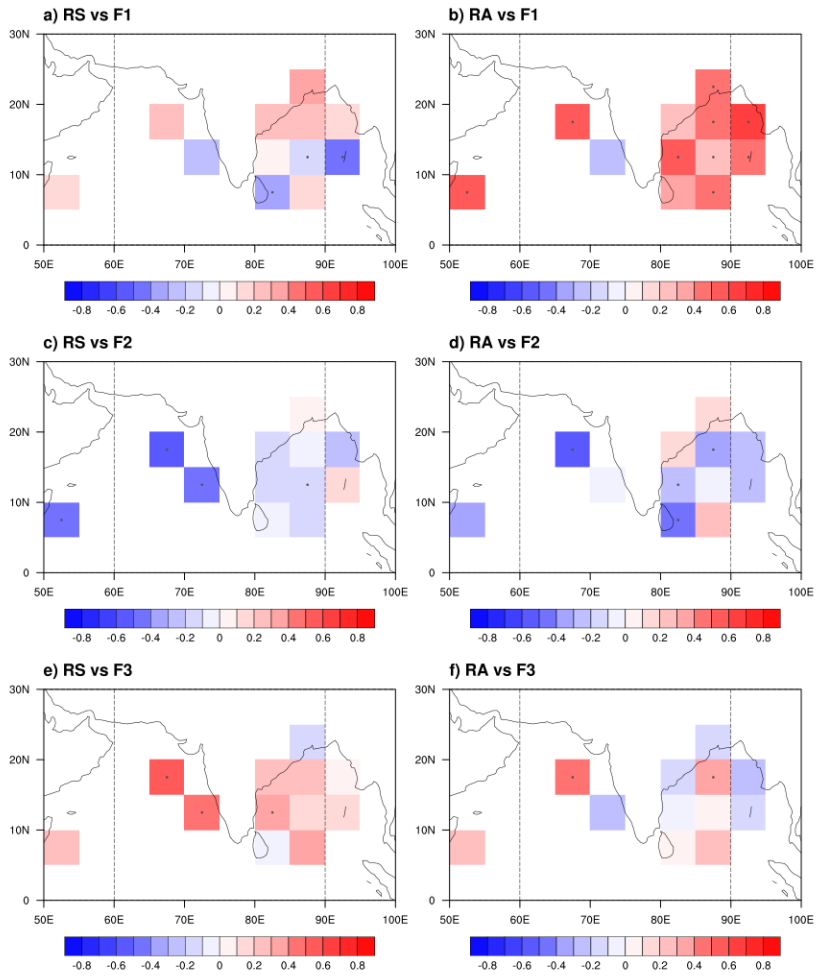

Fig. 3.2.8. Correlation coefficients between TC rainfall (i.e., RS and RA) and three major factors (i.e., F1–F3) in the NI. The correlation coefficient in each 5 degree grid box is calculated from the TCs of which centers are located in the grid box.

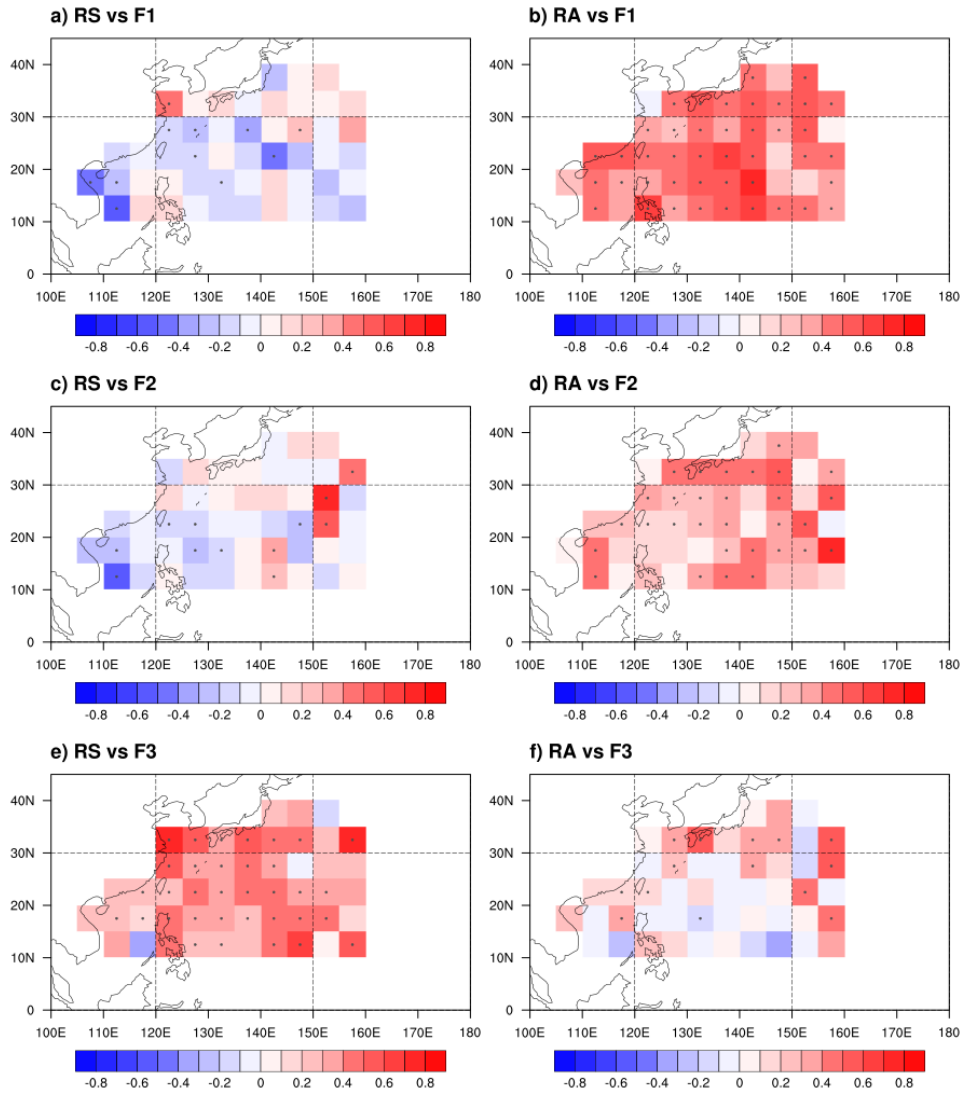

Fig. 3.2.9. Same as the Fig. 3.2.7, but for the WP.

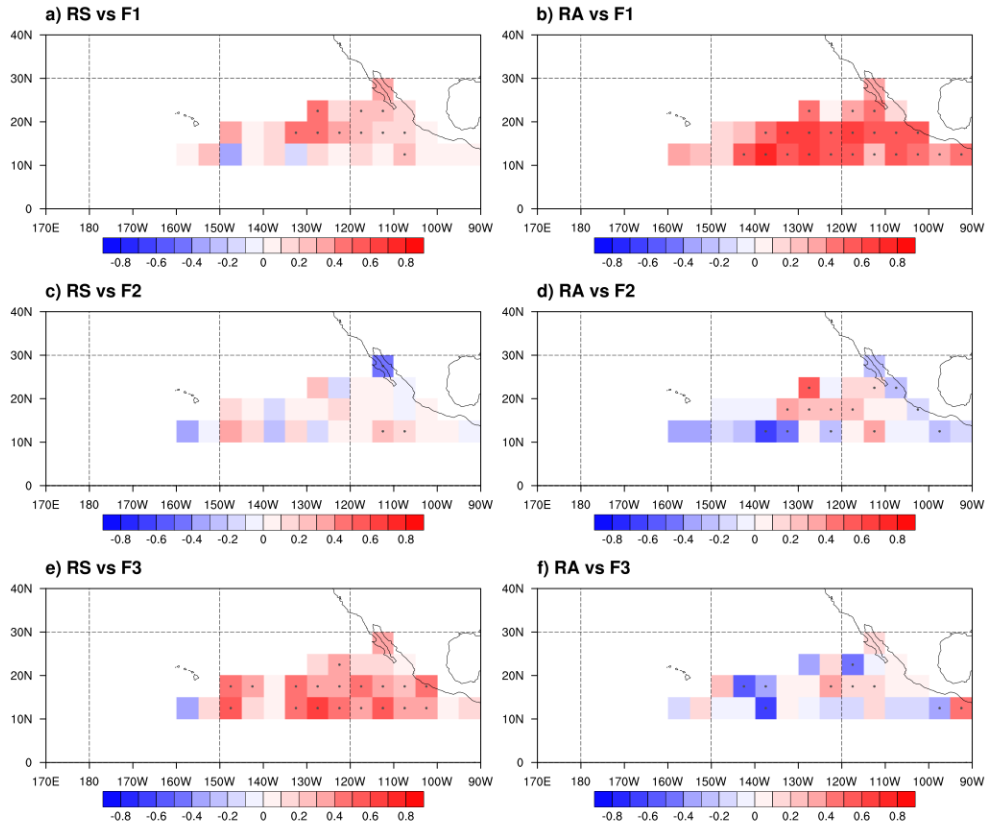

Fig. 3.2.10. Same as the Fig. 3.2.7, but for the EP.

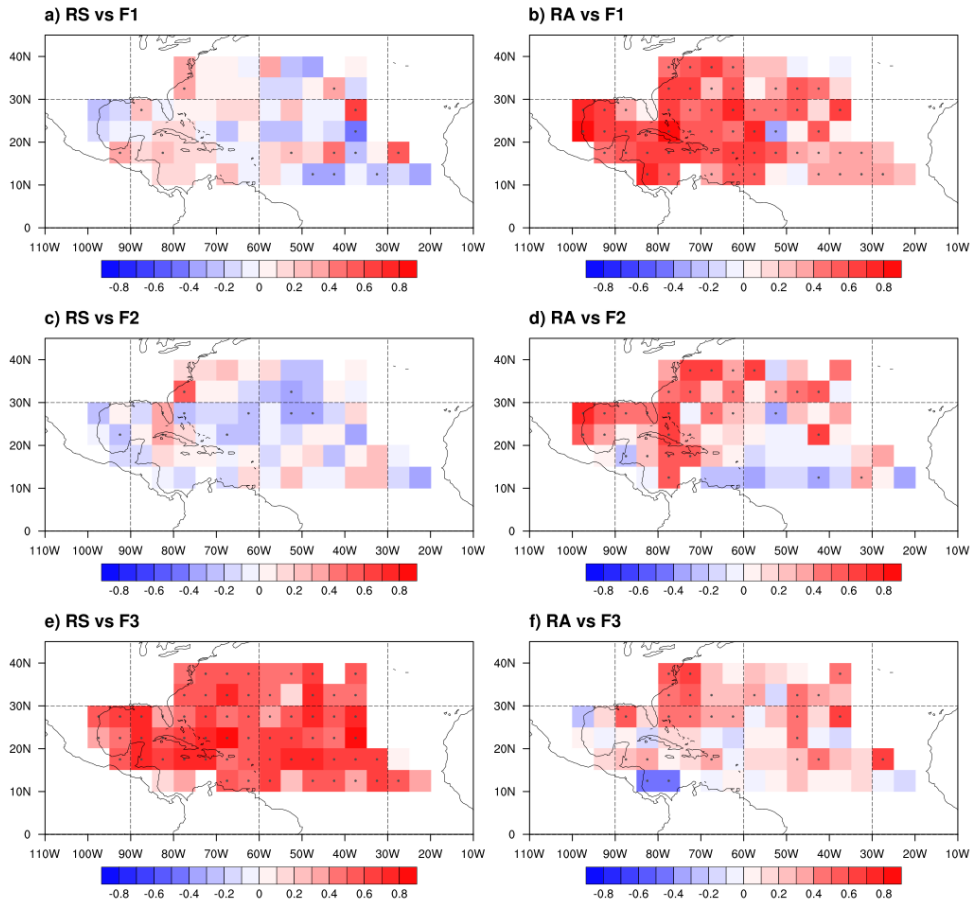

Fig. 3.2.11. Same as the Fig. 3.2.7, but for the NA.

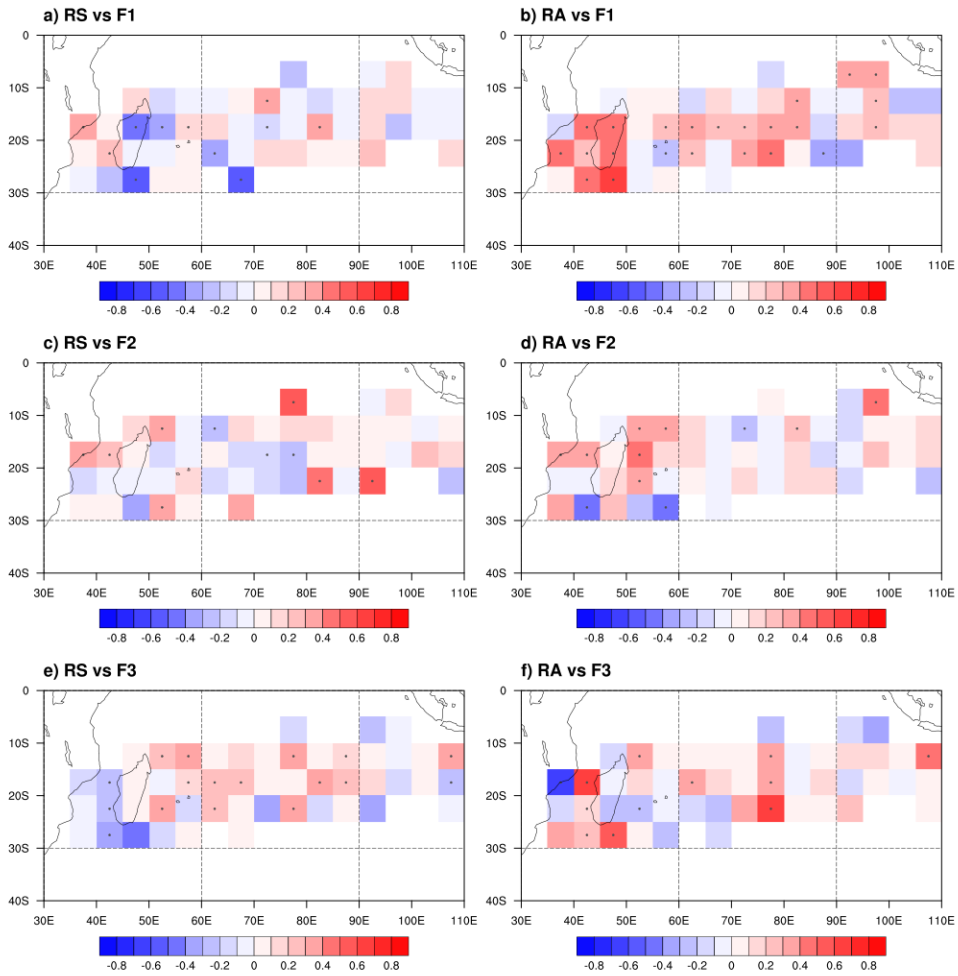

Fig. 3.2.12. Same as the Fig. 3.2.7, but for the SI.

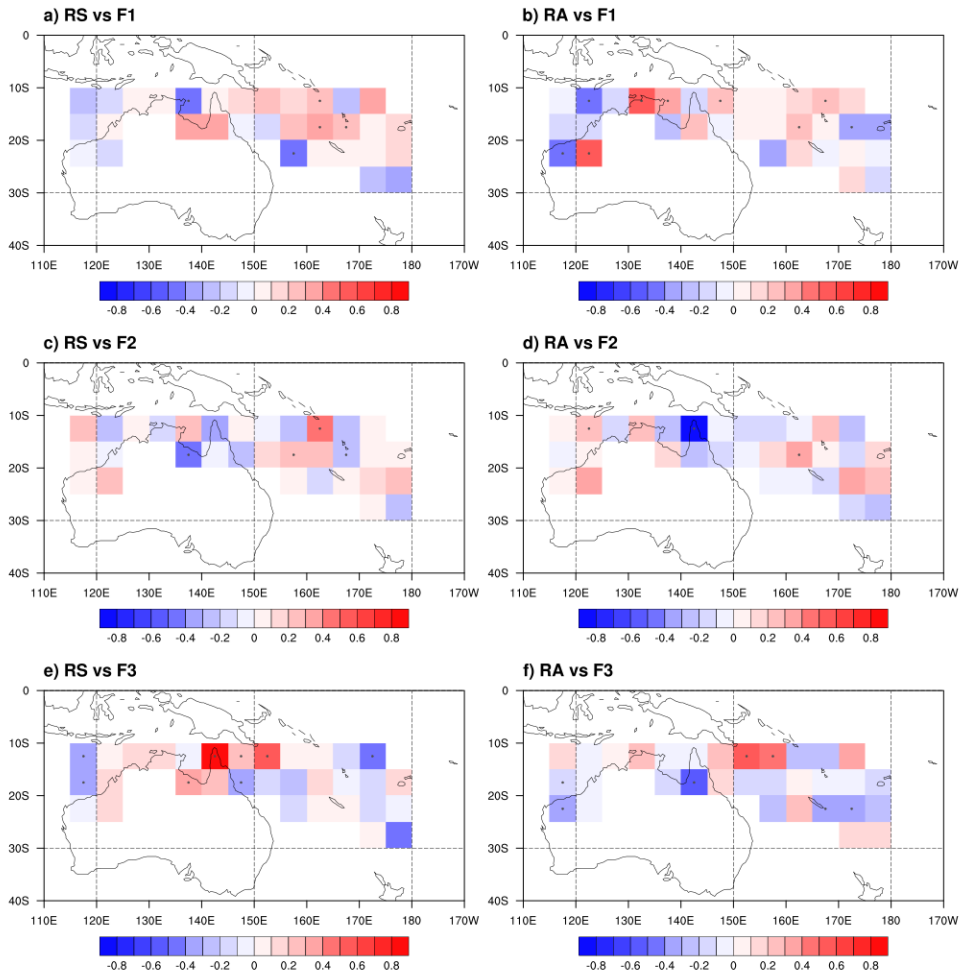

Fig. 3.2.13. Same as the Fig. 3.2.7, but for the SP.

3.2.3. Non-linear Response of Tropical Cyclone Rainfall to Large-scale Environments

a. Tropics and Mid-latitudes

As shown in the previous section, TC rainfall may have non-linear relationship with SST, VWS, and STEER depending on region. In particular, RA presents relationship with SST, VWS, and STEER stronger in mid-latitudes than the tropics. In this section, non-linear response of RA to environmental conditions was investigated by comparing the variation of RA in the tropics and mid-latitudes. The samples of RA were divided into two region according to the location of TC center: 1) tropics from 25°S to 25°N, and 2) mid-latitudes higher than 25°N in the Northern Hemisphere, and lower than 25°S in the Southern Hemisphere. Figure 3.2.14 displays the distributions of samples in the mid-latitudes. Mid-latitude TCs in the EP and NI are excluded in the analysis because of insufficient sample numbers (i.e., less than 87).

Globally, RA in mid-latitudes increases with V_{max}, but its growth rate slows down as TC intensity increases (Fig. 3.2.15a), which is similar to the relationship between wind radii of 12 m s^{-1} and V_{max} (Chavas et al., 2016). Note that RA in the mid-latitudes shows insignificant variations according to SST but clearly increases with STEER and VWS (Figs. 3.2.15b–d). These features are commonly observed in individual ocean basins, although their sample numbers and mean values of RA are different (Figs. 3.2.15e–h). In particular, RA increases with decreasing SST and increasing STEER and

VWS in the WP and the SP. If RA is dominantly controlled by SST, the negative relationship between RA and SST would be hard to appear. Thus, this result suggests that RA in the mid-latitudes is more controlled by dynamic environmental conditions (i.e., STEER and VWS) than thermodynamic one (i.e., SST). In contrast, RA in the tropics is primarily controlled by SST, but not by STEER and VWS (gray color in Figs. 3.2.15b–d), which is consistent with the finding of Lin et al. (2015).

The different variations of RA between the mid-latitudes and the tropics are likely attributed to the different environmental conditions between these two regions. TCs in the tropics are exposed to significantly higher SST than those in the mid-latitudes regardless of STEER and VWS (Fig. 3.2.16). In addition, SST in the tropics shows insignificant variations according to STEER and decreases slowly with VWS (gray color in Fig. 3.2.16), while SST decreases rapidly with STEER and VWS in the mid-latitudes (black color in Fig. 3.2.16). Summing up, TCs in the mid-latitudes generally meet cooler SST with stronger environmental flows (i.e., STEER and VWS) compare to those in the tropics (Table 3.2.4). Because SST is the major energy source of TC, sufficiently warm SST (usually above 26–27℃) is a necessary condition for TC development (Palmen, 1948, Gray, 1968). A TC also can resist the influence of environmental flows when it is strong enough (e.g., Jones, 1995, Wong and Chan, 2004). Thus, the sensitivity of RA to STEER and VWS may increase in cool SST conditions. Indeed, RA in the mid-

latitudes and the tropics show similar variations according to STEER and VWS (Figs. 3.2.15c and 15d) when SST is cooler than 27–28℃ (Fig. 3.2.16).

At this point, it is necessary to discuss about how STEER and VWS affect RA. In the mid-latitudes, TCs show a distinct rainfall asymmetry regardless of ocean basin (Fig. 3.2.17). In particular, RA expends northeastward and southeastward in the Northern (Figs. 3.2.17a and b) and the Southern Hemisphere (Figs. 3.2.17c and d), respectively. It is also notable that the direction of the rainfall asymmetry is located between the directions of STEER (blue arrows in Fig. 3.2.17) and VWS (red arrows in Fig. 3.2.17). This result is consistent with previous studies showing that TC rainfall is enhanced asymmetrically at front-right (front-left) side of TC motion and downshear-left (downshear-right) side in the Northern (Southern) Hemisphere (Corbosiero and Molinari 2002, 2003; Chen et al. 2006). The magnitude of rainfall asymmetry increases with STEEER and VWS (Figs. 3.2.18a and b, respectively). Particularly, rainfall asymmetry doubles when VWS increases from 0 to 26 m s^{-1}. The rainfall asymmetry in the Southern Hemisphere is significantly larger than that in the Northern hemisphere, which is also related to the stronger VWS in the Southern Hemisphere than in the Northern Hemisphere (Table 3.2.5). Changes in rainfall asymmetry due to STEER are relatively small compared to those induced by VWS. In addition, there is no clear increase in rainfall asymmetry when STEER is lower than 5 m s^{-1}. These results may imply that VWS develops asymmetric rainfall more efficiently than STEER does, which is similar to the results of

Chen et al. (2006). Lastly, the relationship between RA and asymmetries also shows that RA tends to increase (by up to a factor of 2) with rainfall asymmetry (Fig. 3.2.18c), and the increasing rate levels off above certain asymmetry values. The RA generally increases in the rainfall asymmetry range of 0.5–1.4. Therefore, higher STEER and VWS are likely to enlarge RA by encouraging asymmetric rainfall structure. All the results above are consistently found in each ocean basin.

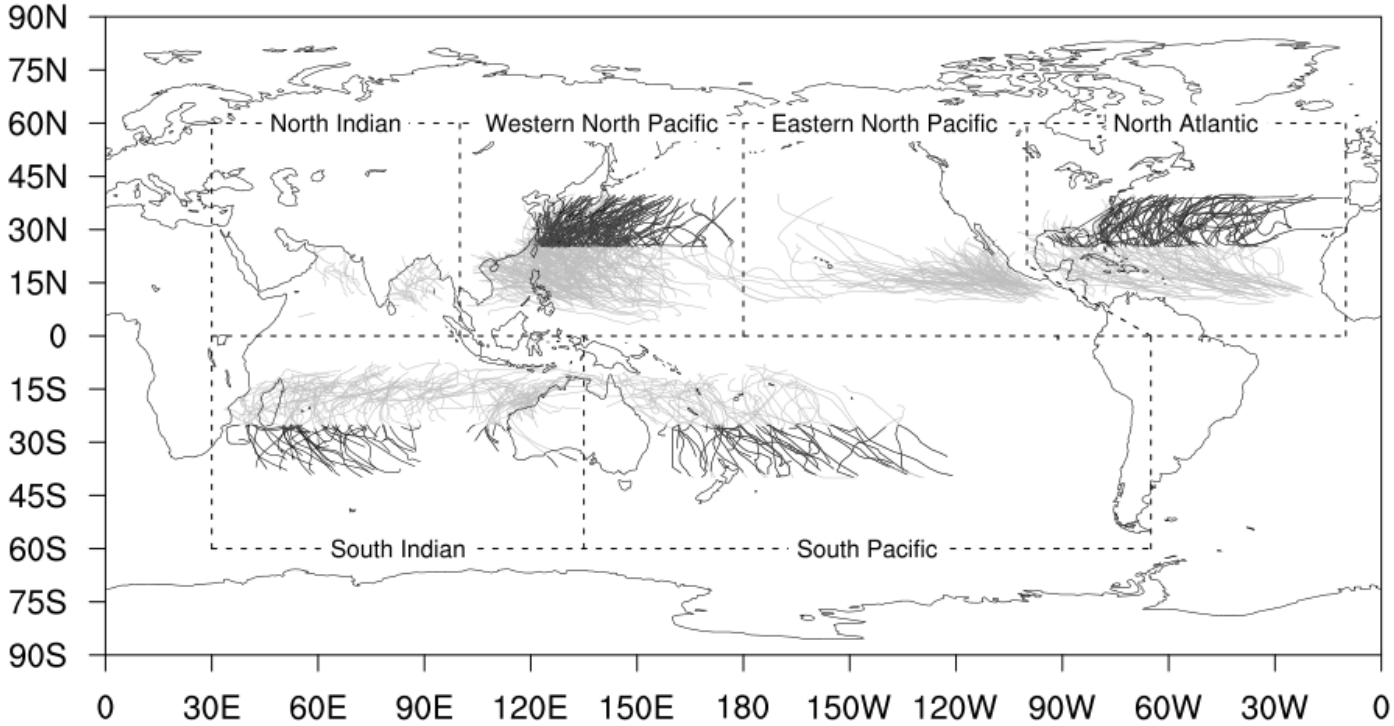

Fig. 3.2.14. Global TC tracks during 1998–2013 and locations of six ocean basins. The black lines indicate TC tracks of mid-latitudes analyzed in this study.

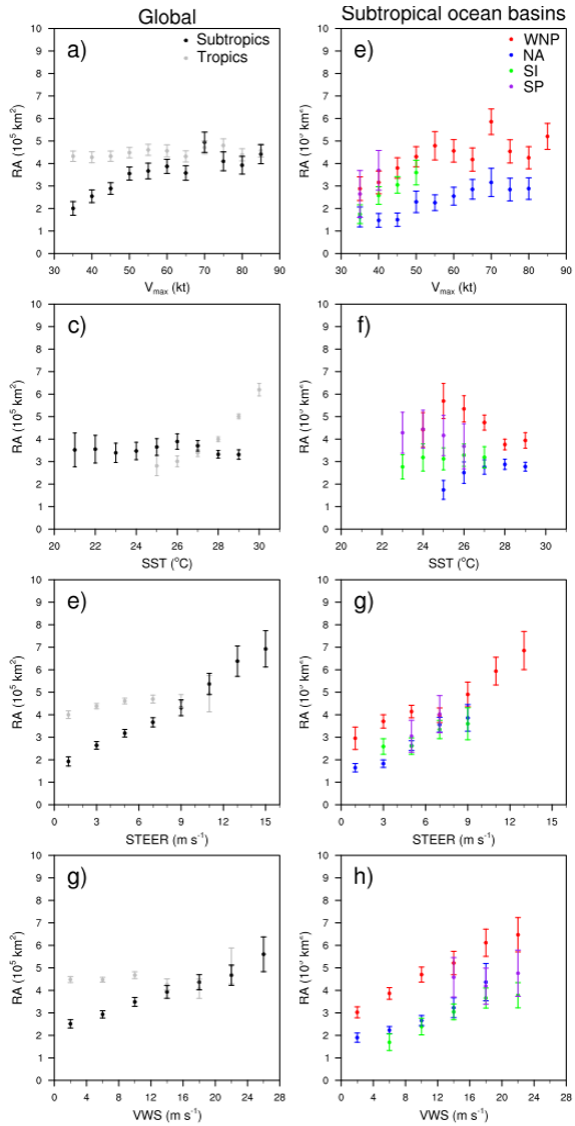

Figure 3.2.15. Distributions of RA with varying a–b) V_{max}, c–d) SST, e–f) STEER, and g–h) VWS. Left and right columns present the analysis result for global and individual subtropical ocean basins, respectively. Dots and error bars denote the mean and 95% confidence interval of the mean, respectively. Only bins with sample numbers larger than 50 are presented here.

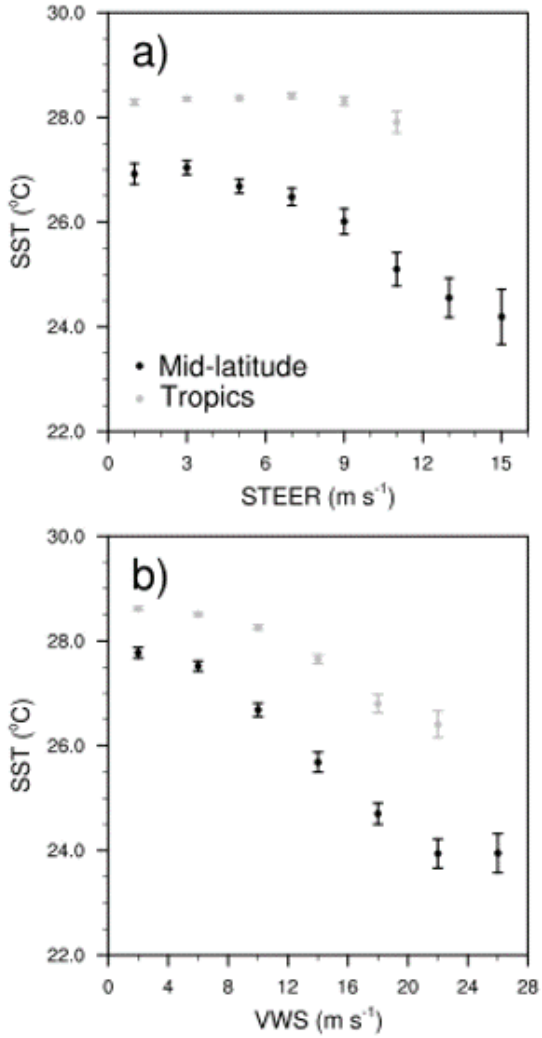

Figure 3.2.16. Distributions of SST with varying a) STTER, and b) VWS in the mid-latitudes and the tropics of global oceans. Dots and error bars denote the mean and 95% confidence interval of the mean, respectively. Only bins with sample numbers larger than 50 are presented here.

Table 3.2.4. Average environmental conditions in the mid-latitudes and the tropics. All environmental conditions in the two regions show significant difference at the 99% confidence level.

	SST (°C)	STEER ($m\ s^{-1}$)	VWS ($m\ s^{-1}$)
Mid-latitudes	26.4	6.0	10.8
Tropics	28.3	5.5	6.8

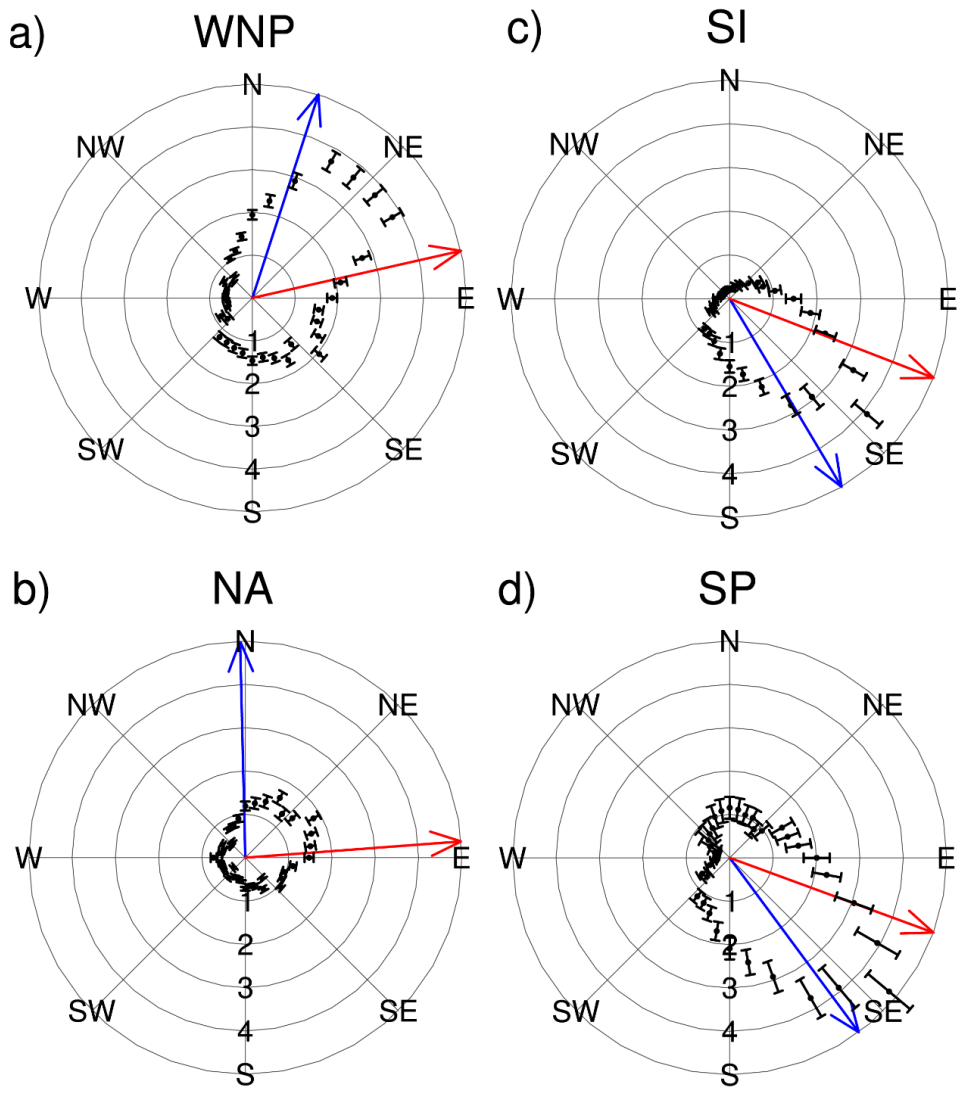

Figure 3.2.17. Average RA in azimuthal bins (unit: 10^4 km^2) in the a) WP, b) NA, c) SI, and d) SP. Blue and red arrows indicate the direction of TC motion and vertical wind shear, respectively. Dots and error bars denote the mean and 95% confidence interval of the mean, respectively.

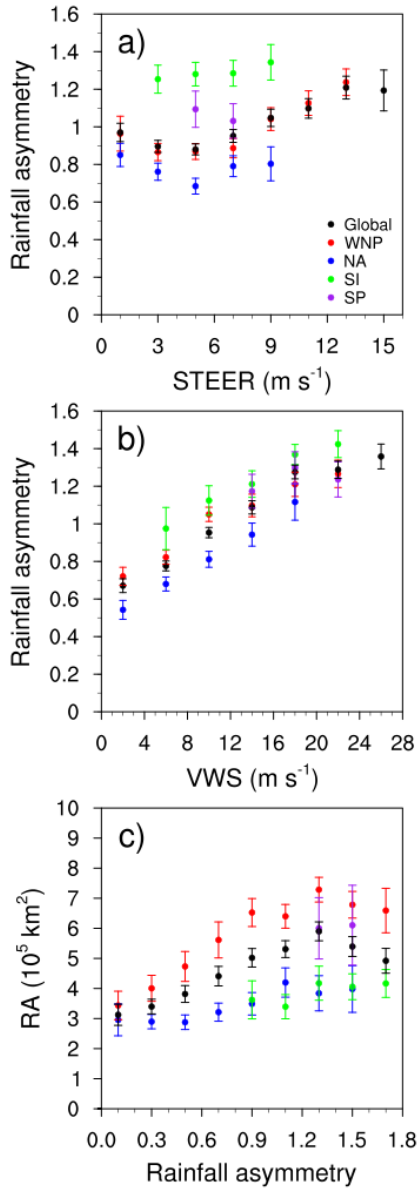

Figure 3.2.18. Rainfall asymmetry distributions of mid-latitude TCs in global and individual ocean basins with varying a) STEER, and b) VWS. The relationship between RA and asymmetry are shown in c). Dots and error bars denote the mean and 95% confidence interval of the mean, respectively. Only bins with sample numbers larger than 50 are presented here.

Table 3.2.5. Average environmental conditions in the individual subtropical ocean basins.

	SST (°C)	STEER ($m\ s^{-1}$)	VWS ($m\ s^{-1}$)
WP	27.1	6.4	9.1
NA	27.2	4.9	8.8
SI	24.4	5.9	15.4
SP	23.9	8.3	16.7

b. South Korea

In this section, influence of VWS on TC wind and rainfall over the South Korea is investigated. South Korea is frequently affected by TCs, about 3 TCs a year to suffer considerable damages. For example, TCs Rusa in 2002 and Maemi in 2003 caused economic losses of 41 and 35 billion USD, respectively. In addition, large baroclinic environments prevail over South Korea and significantly affects the characteristics of TCs (e.g., track, wind and rainfall intensity) in this region (Kim et al., 2005, Kim et al., 2006, Choi et al., 2009). For example, Kim et al. (2006) suggested the effects of an upper-tropospheric trough can significantly contribute to the variations of TC rainfall over South Korea. Park et al. (2016) also showed that extratropical transition (ET) occurs frequently over South Korea, and the spatial distributions of winds and rainfall are significantly different between TCs with and without ET process. Previous studies were based on weather station data in South Korea and did not examine the details of the wind and rainfall structures. This study focused on the influence of baroclinic environment (i.e., VWS) on wind and rainfall structures of landfalling TCs.

The TC landfall over South Korea is defined as the period during which the distance between the TC center and the nearest coastline of South Korea is less than 500 km. This definition deviates from the strict definition of TC landfall (i.e., the timing when the TC center encounters a coastline), but is consistent with a number of studies because the impact of a TC can occur even before the TC hits the coastline (Kim et al., 2006, Park et al., 2015, Park

et al., 2016). Figure 3.2.19 shows the tracks of 57 TCs selected based on this definition for the analysis period 1998–2013. The number of 6 hourly sample of TC wind and rainfall are 283 during the landfall period.

Prior to analyzing the variation of TC wind and rainfall, composite structures of horizontal winds and rainfall for the entire 283 samples during the landfall periods were examined. The mean 10-m wind field depicts well-organized cyclonic circulation with distinct asymmetry in the left and right sides of the TC motion (Fig. 3.2.20a). This wavenumber-1 asymmetry is a well-known feature of moving TCs (Shapiro, 1983, Frank and Ritchie, 1999, Peng et al., 1999, Chen et al., 2006a). The rainfall area lies mainly in the front side of the TC (Fig. 3.2.20b) and is attributed to the asymmetric wind structure inducing surface convergence and upper-tropospheric divergence to promote vigorous convection and heavy rainfall there (Figs. 3.2.20c and d). Note that most of TCs present their maximum wind and rainfall in the right and front side, respectively (Table 3.2.6). In addition, southwesterlies are dominant in the upper troposphere (Fig. 3.2.20d), implying that TCs were strongly affected by the westerly jet prevailing in the mid-latitudes. Figure 3.2.21 shows the environmental VWS over East Asia during the landfall period. It is noteworthy that the VWS over South Korea is very strong (mean value > 20 m s^{-1}; Fig. 3.2.21a) and shows large variation between samples (standard deviation > 10 m s^{-1}; Fig. 3.2.21b). This implies that TCs landfalling in South Korea can be significantly affected by baroclinic environments (i.e., environmental VWS); this will be discussed later. The direction of VWS (Fig

3.2.21a) is similar to the direction of TC motions, since the moving direction of TCs landfalling in South Korea is generally north-eastward (Fig. 3.2.19).

Figure 3.2.22 displays the variations of wind and rainfall area of landfalling TCs according to the VWS. Similar to the RA, wind area (WA) is defined as the total area in which wind speed exceeds 14 m s^{-1} within 1000 km from a TC center. No significant relationship is found between the WA and VWS (r = 0.07); however, the RA significantly increases with vertical wind shear (r = 0.37; significant at the 95% confidence level). To examine the detailed effects of the VWS, TCs in strong shear cases (i.e., SS cases) are compared against those in weak shear cases (i.e., WS cases). The mean and standard deviation of the VWS surrounding TCs are 11.03 m s^{-1} and 5.95 m s^{-1}, respectively. The SS and WS are defined as VWS stronger than the mean value plus half of the standard deviation of VWS (14.01 m s^{-1}), and weaker than the mean value minus half of the standard deviation of VWS (8.05 m s^{-1}), respectively. Applying the conditions, 82 (102) SS (WS) cases are identified.

The wind and rainfall structures distinctly vary between the SS and WS cases. Figure 3.2.23 displays the composite structures of surface wind at 10-m level and rainfall for the two cases, as well as their differences. Both cases show the cores of maximum wind in the right side of the TC moving direction (Figs. 3.2.23a and c). The SS cases show weaker (stronger) winds in the right (left) side compared to the WS cases (Fig. 3.2.23e). Thus, there is no significant difference in the WA between the two cases (Table 3.2.7). On the

other hand, the SS cases shows a notable asymmetric rainfall structure, while WS cases show nearly symmetric rainfall (Figs. 3.2.23b and d). The RA in the SS cases is significantly enhanced (slightly reduced) in front (behind) of TCs compared to the WS cases (Fig. 3.2.23f). Consequently, the RA is significantly larger (about 1.5 times on average) in the SS cases than in the WS cases (Table 3.2.7). The TC intensities are similar in the two cases.

The SS and WS cases also show significantly different dynamic structures. The SS cases show anomalous rising and sinking motions in the front and rear side of the TC, respectively, compared to the WS cases (Fig. 3.2.24). It is notable that the difference of the vertical velocity (Fig. 3.2.24c) matches closely the difference of rainfall (Fig. 3.2.23e). This dipole pattern of vertical velocity difference indicates the occurrence of asymmetric convection within TCs. A number of studies showed that the asymmetric convection in TCs can be induced by vertical tilting by VWS (Flatau et al., 1994, Jones, 1995, DeMaria, 1996, Frank and Ritchie, 1999, 2001, Wong and Chan, 2004); a TC experiencing strong environmental vertical wind shear can induce rising and sinking motions in the downshear-left and upshear-right side, respectively (Corbosiero and Molinari, 2002, 2003, Wong and Chan, 2004, Chen et al., 2006a). Note that the average VWS vectors (black arrows in Fig. 3.2.24) and associated vertical motions in TCs found in this study are consistent with the results reported in earlier studies. In both cases, strong rising motions appear in the downshear-left side while there are almost no rising motions in the upshear-right side. The SS cases shows stronger VWS

(18.6 m s^{-1}) than the WS case (5.2 m s^{-1}) (Table 3.2. 7; Figs. 3.2.23a and b). Thus, the difference of shear vector (19.0 m s^{-1}) between the two types of TCs can induce the relative rising and sinking motions at the front and rear side of TC, respectively (Fig 3.2.24c).

The difference of the environmental condition in the mid-latitude East Asia between the SS and WS cases supports that the difference of the VWS within TCs (Fig. 3.2.24) are induced by the large-scale circulation. For the SS cases, significantly stronger vertical wind shear appears in the mid-latitude East Asia compared to the WS cases (Fig. 3.2.25). This strong vertical wind shear is associated with the upper-level trough located in the northeastern China near Beijing. The upper-level trough plays a key role in rapid intensification of TCs (Molinari and Vollaro, 1989, Bosart et al., 2000, Ritchie and Elsberry, 2003) as well as the changes in the TC structure such as extratropical transition (ET) (Klein et al., 2002, Ritchie and Elsberry, 2003). In particular, Hanley et al. (2001a) showed that the vertical circulation of a TC can be significantly changed while horizontal wind is not intensified when the TC is affected by the upper-level trough accompanied by strong VWS (larger than 10 m s^{-1}) as also found in this study. In addition, the ET process can be closely related to the findings in this study. In the mid-latitudes, a number of TCs show significant changes such as frontogenesis, vertical tiling, abrupt intensification of wind and rainfall, during the ET process (Harr and Elsberry, 2000, Klein et al., 2000, Jones et al., 2003). Indeed, most of the TCs (about 90%) reaching the mid-latitude (> 30°N) region in the WNP show ET

processes during the analysis period in this study (1998–2013). The vertical tilting and asymmetric vertical motion are also frequently observed in the ET process (Evans and Hart, 2003, Evans et al., 2017).

Figure 3.2.26 presents the spatial distribution of TC centers for the SS and WS cases. The mean latitude of the TC centers in the SS cases (34.1°N) is significantly higher (95% confidence level) than that for the WS cases (31.9°N) consistently with the distribution of environmental VWS (i.e. stronger shear in higher latitude; Fig. 3.2.21). There is no significant difference of the mean longitude of the TC center between the SS and WS cases (128.1°E and 127.7°E, respectively). In the landfall period, the wind area of TCs can be reduced due to the increasing surface friction while the rainfall area of TCs can be enhanced by topography (Chan and Liang, 2003, Chen and Yau, 2003, Yang et al., 2008, Li et al., 2014). Such effects of topography may contribute to the variation of RA in the SS and WS cases. However, TCs are not confined within land areas for both the SS and WS cases (Fig. 3.2.26). Thus, the overall results in this study would remain valid even with topographic effects.

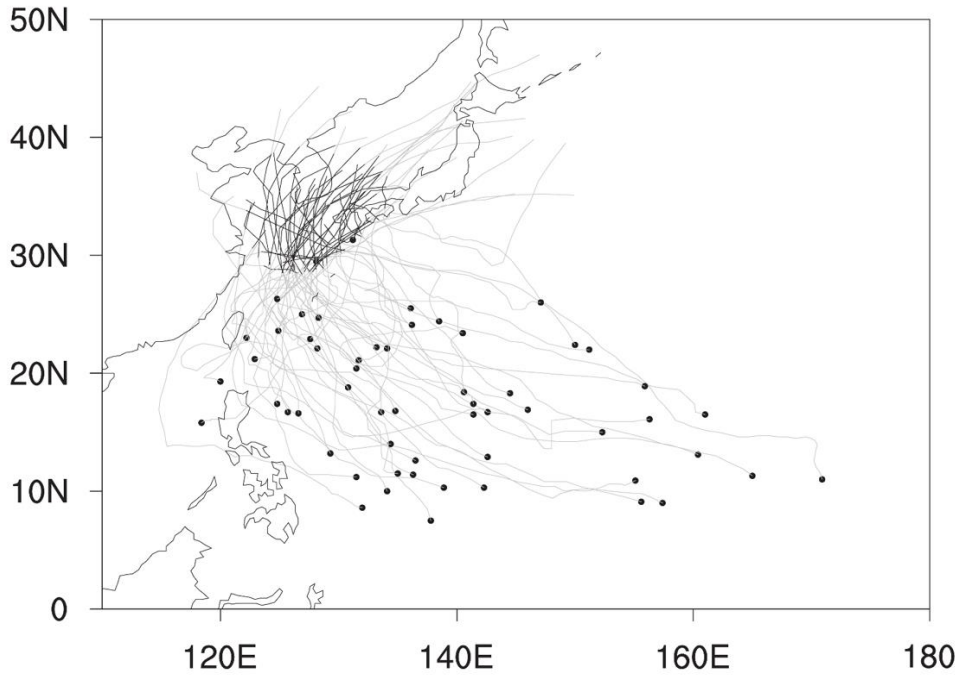

Fig. 3.2.19. Tracks of TCs making landfall over South Korea during 1998–2013. The black and gray lines indicate tracks of landfall period and entire life time of each TC, respectively. Dots denote the genesis locations of TCs.

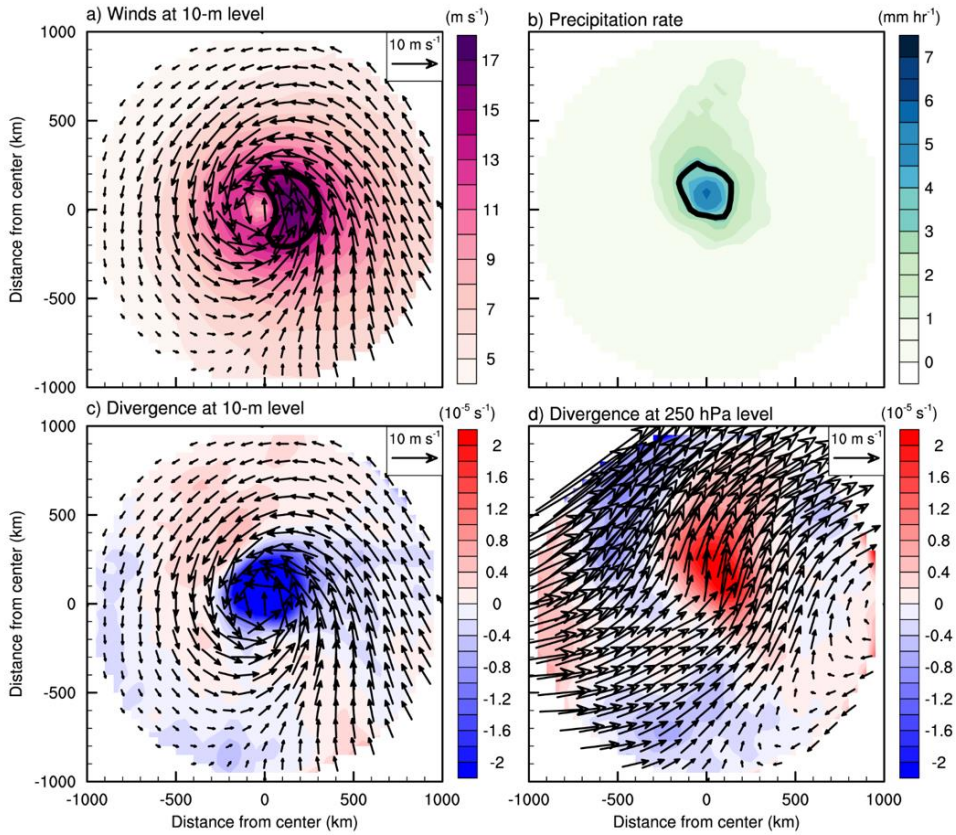

Fig. 3.2.20. The averaged horizontal TC structures of (a) wind at 10-m level (arrows, unit: m s^{-1}) with its speed (shaded, unit: m s^{-1}), (b) precipitation rate (unit: mm hr^{-1}), and divergence (shaded, unit: 10^{-5} s^{-1}) and wind (arrows, unit: m s^{-1}) at (c) 10-m and (d) 250 hPa level during the landfall period. The directions of x- and y- axis are right and front to TC motion, respectively.

Table 3.2.6. The occurrence numbers of maximum wind and rainfall in the center region, and four quadrants (front, right, rear, and left) out of the center region. The center region is defined as the region within 100 km from the TC center. The direction of four quadrants are based on the direction of TC motion.

	Center	Front	Right	Rear	Left
Maximum wind	26	39	172	29	17
Maximum precipitation	53	114	55	41	20

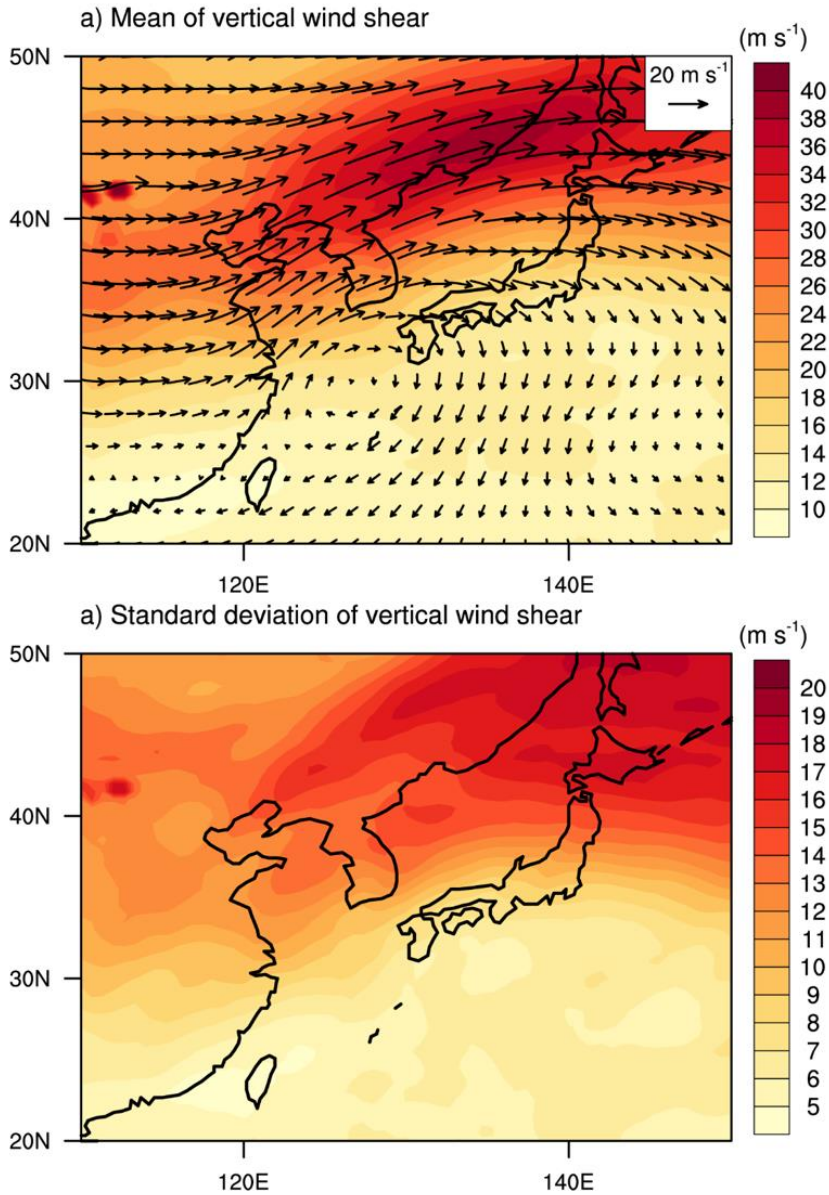

Fig. 3.2.21. The (a) mean and (b) standard deviation of vertical wind shear over the East Asia region during the landfall period.

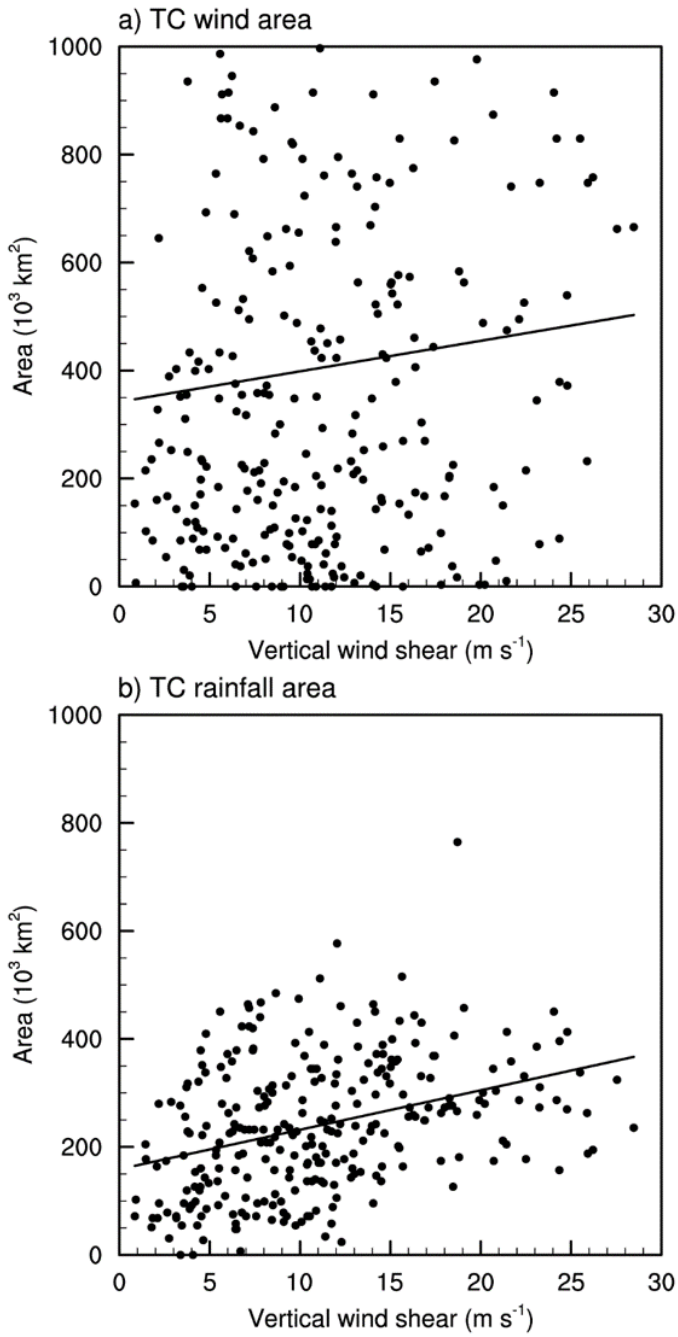

Fig. 3.2.22. Distributions of the (a) wind area, and (b) rainfall area according to the vertical wind shear. The solid line in each plot denotes the linear regression line.

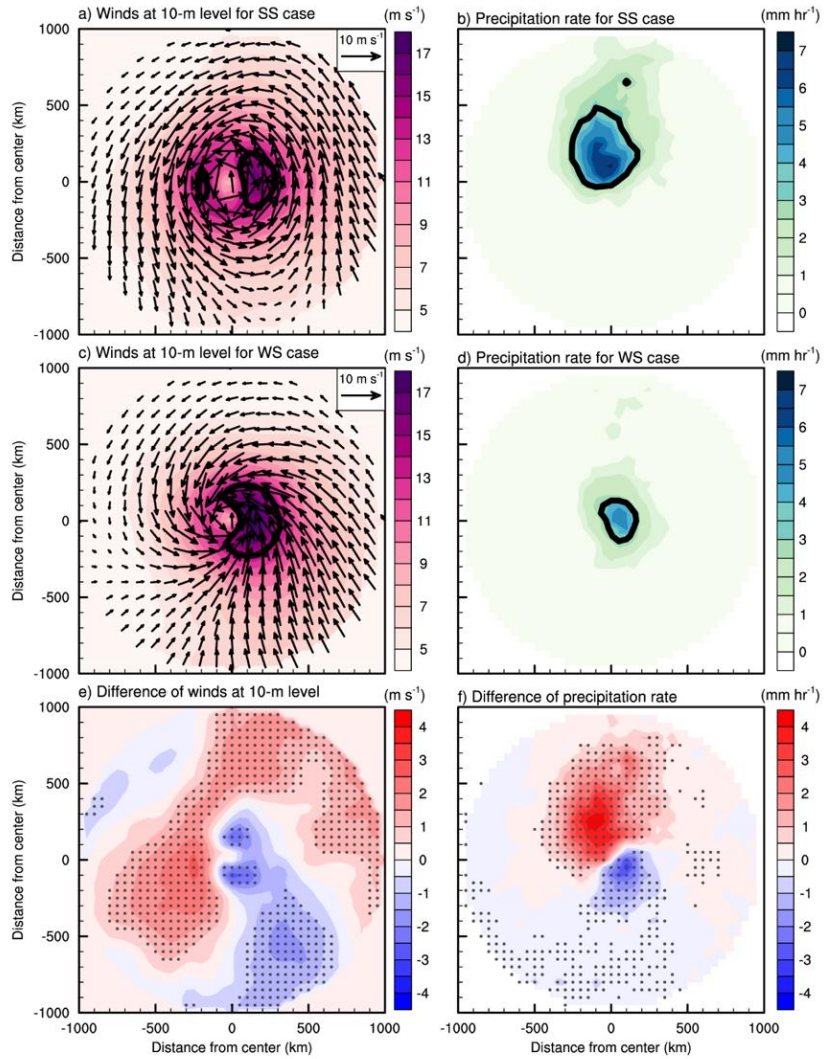

Fig. 3.2.23. The averaged horizontal TC structure of wind at 10-m level (arrows, unit: m s^{-1}) with its speed (shaded, unit: m s^{-1}), and precipitation rate (unit: mm hr^{-1}) for the (a, b) strong shear (SS) case, (c, d) weak shear (WS) case, and (e, f) their differences (SS minus WS) during the landfall period. The directions of x- and y- axis are right and front to TC motion, respectively. The gray dots indicate the statistically significant differences at the 95% confidence level evaluated with Student's *t*-test.

Table 3.2.7. The average vertical wind shear, wind area, rainfall area, and minimum sea level pressure of TCs for the strong and weak shear cases. Statistically significant differences between the two cases for vertical wind shear and rainfall area appear at the 95% confidence level evaluated with Student's *t*-test.

Case	Sample number	Vertical wind shear (m s^{-1})	Wind area (10^3 km^2)	Rainfall area (10^3 km^2)	Min SLP (hPa)
Strong shear	82	18.6	324.6	276.4	976.7
Weak shear	102	5.2	304.9	176.4	977.3

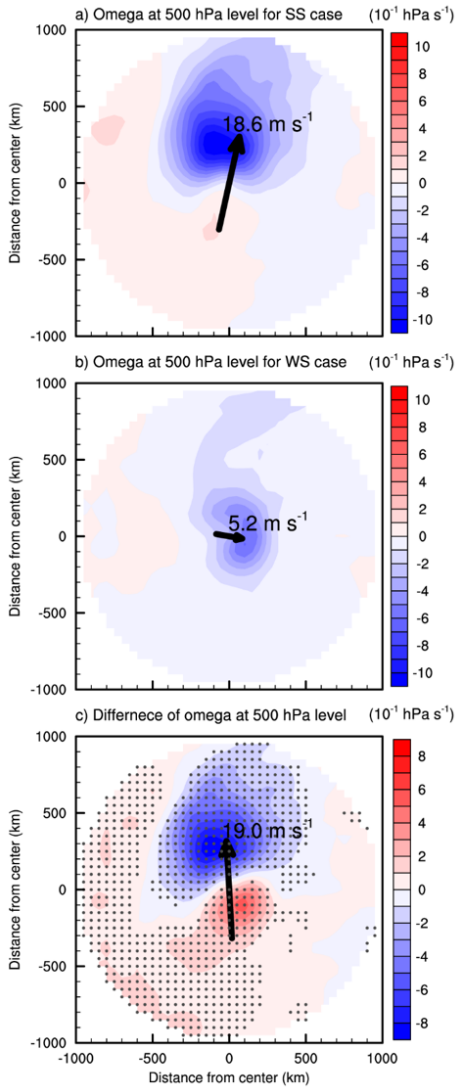

Fig. 3.2.24. The vertical velocity (shaded, unit: 10^{-1} hPa s^{-1}) at 500 hPa level and the vertical wind shear vector (arrow, unit: m s^{-1}) in the (a) SS case, (b) WS case, and (c) their differences (SS minus WS) during the landfall periods. The directions of x- and y- axis are right and front to TC motion, respectively. The gray dots indicate the statistically significant differences at the 95% confidence level evaluated with Student's *t*-test.

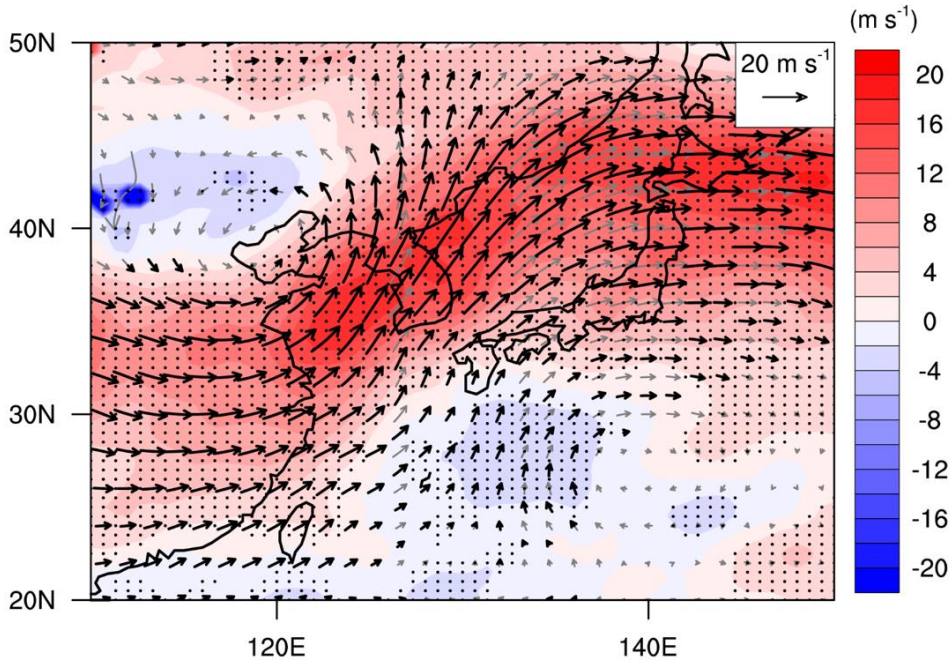

Fig. 3.2.25. The difference composite (SS minus WS) of vertical wind shear (arrows, unit: m s^{-1}) and its magnitude (shaded, unit: m s^{-1}) between 850 and 250 hPa level. The thick black arrows and gray dots indicate the statistically significant differences at the 95% confidence level evaluated with Student's *t*-test.

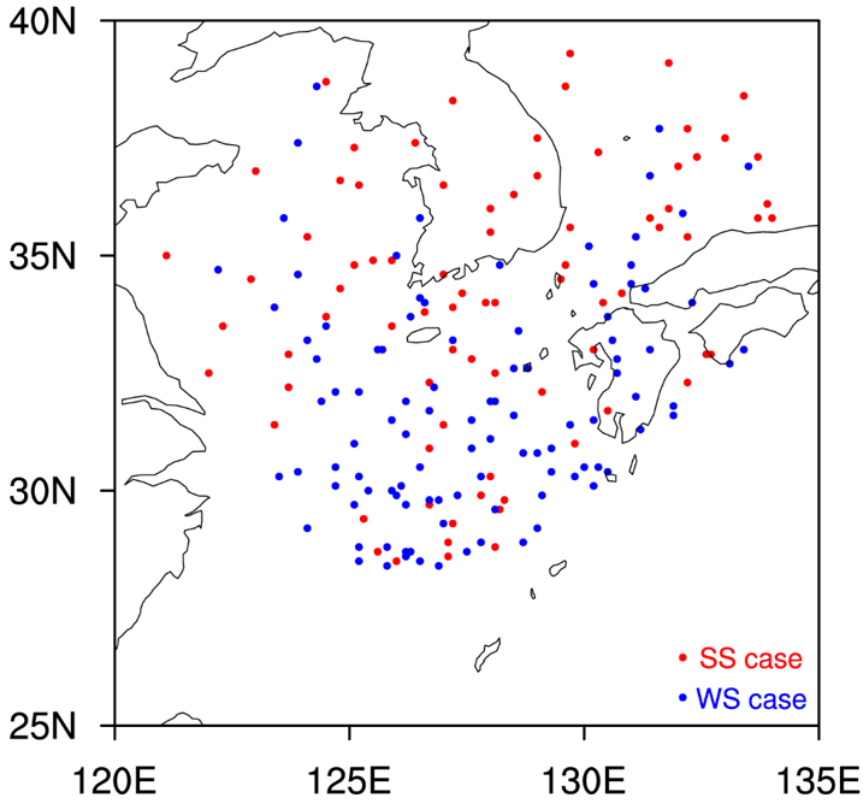

Fig. 3.2.26. The distribution of TC center for the SS (red) and WS (blue) cases.

3.2.4. Development of Statistical Models for Tropical Cyclone Rainfall

This study investigated factors affecting TC rainfall from the Section 3.2.1 to 3.2.3. Using the controlling factors (i.e., F1–F3) obtained from the Section 3.2.2, multi-variable linear regression models for RS and RA over the six basins were constructed. The regression models using the three major factors explain 10.9–37.2% and 27.0–41.0% variability of the RS and RA over the six basins, respectively (Tables 3.2.8–3.2.13). The factor showing the largest partial regression coefficient in the RS models is the F3 (r = 0.27–0.60), while that in the RA model is the F1 (r = 0.51–0.64). For the RS models, the model of the NA shows the best performance. The NA presents the strongest relationship between TC rainfall and the primary circulation among the six basins (Table 3.2.2), which can be the reason for the good performance of the model for the NA. The worst RS model is for the NI where the relationship between RS and V_{max} is the weakest. On the other hand, RA models for the six basins present similar performance.

The spatial distributions of mean RS and RA estimated from the model are similar to those from the observation, except the SI and SP (Figs. 3.2.27––3.2.32). The pattern correlations of RS and RA between the observation and regression model in the NI, WP, EP, and NA are 0.52–0.95, and 0.74–0.95, respectively. Therefore, current statistical models successfully explain climatological spatial distributions of RS and RA in the Northern Hemisphere. In addition, the correlation coefficient of RS or RA between the observation and model in each 5 degree grid box is statistically significant in overall

region of the NI, WP, EP, and NA. Thus, the models are feasible to explain the variations as well as mean value of RS and RA. On the other hand, RS and RA models for the SI, and SP show low performance to estimate climatological distributions and variations of RS and RA. The reason for the failure of models for the two basins should be investigated in detail in further study.

Table 3.2.8. Results of multi-variable linear regression models for the RS and RA over the NI. The R indicates correlation coefficient between the model and observation.

	R	Standardized regression coefficient		
		F1	F2	F3
RS model	0.33	0.139	-0.131	0.272
RA model	0.54	0.525	-0.14	-0.016

Table 3.2.9. Same as Table 3.2.8, but for the WP.

	R	Standardized regression coefficient		
		F1	F2	F3
RS model	0.35	0.045	–0.084	0.332
RA model	0.52	0.510	0.076	0.061

Table 3.2.10. Same as Table 3.2.8, but for the EP.

	R	Standardized regression coefficient		
		F1	F2	F3
RS model	0.48	0.369	-0.041	0.311
RA model	0.64	0.638	0.008	0.045

Table 3.2.11. Same as Table 3.2.8, but for the NA.

	R	Standardized regression coefficient		
		F1	F2	F3
RS model	0.61	0.088	–0.083	0.598
RA model	0.56	0.530	0.059	0.160

Table 3.2.12. Same as Table 3.2.8, but for the SI.

	R	Standardized regression coefficient		
		F1	F2	F3
RS model	0.51	0.132	-0.213	0.442
RA model	0.55	0.541	0.021	0.068

Table 3.2.13. Same as Table 3.2.8, but for the SP.

	R	Standardized regression coefficient		
		F1	F2	F3
RS model	0.43	0.179	-0.225	0.323
RA model	0.56	0.531	0.017	0.16

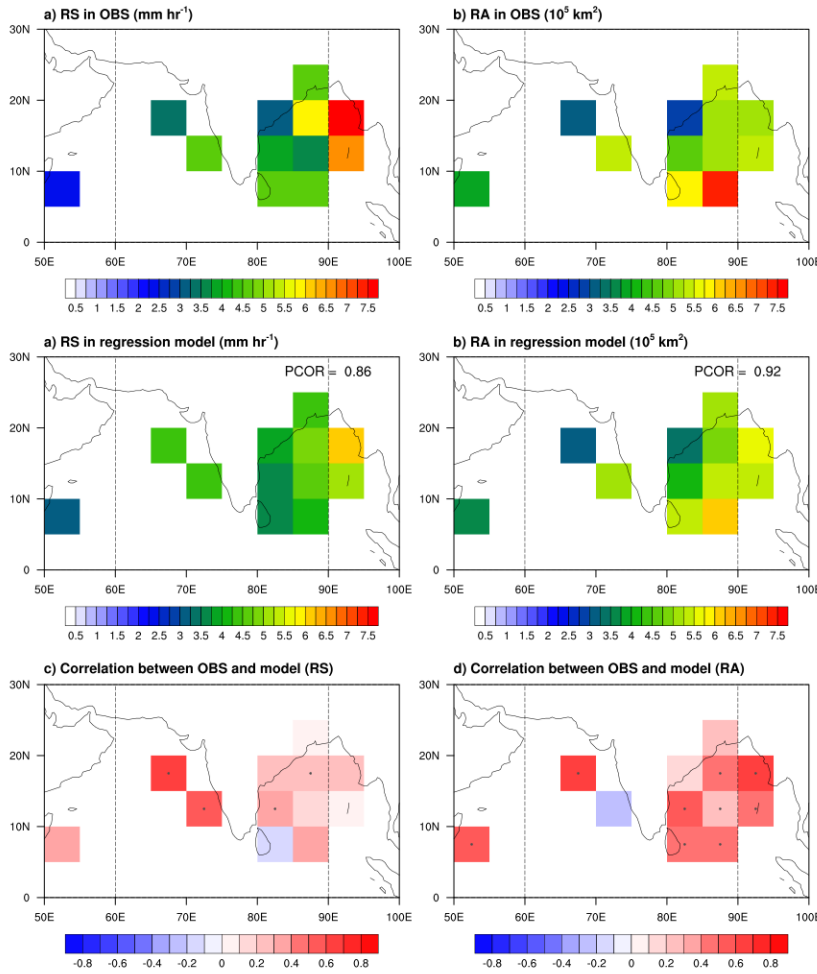

Fig. 3.2.27. Mean a) RI, and b) RA in each 5 degree grid box estimated by the statistical model for the NI. The correlation coefficient between the observation and estimation in each grid box is presented in c), and d).

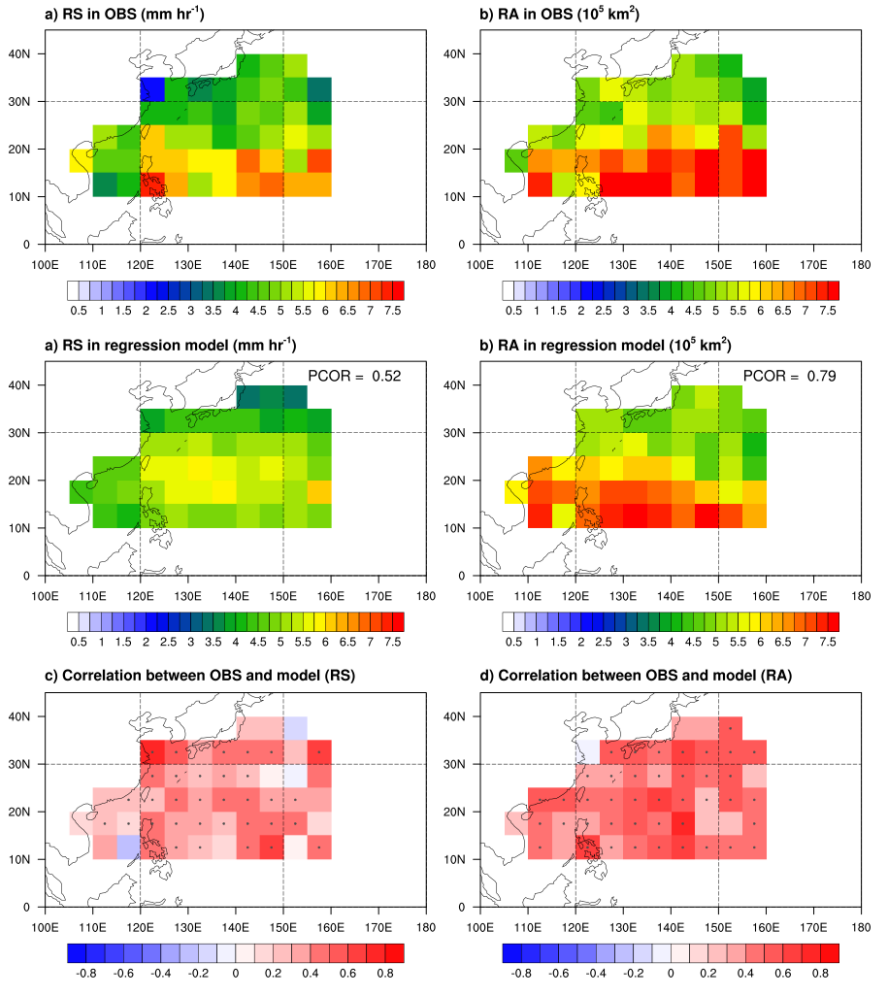

Fig. 3.2.28. Same as Fig. 3.2.27, but for the WP.

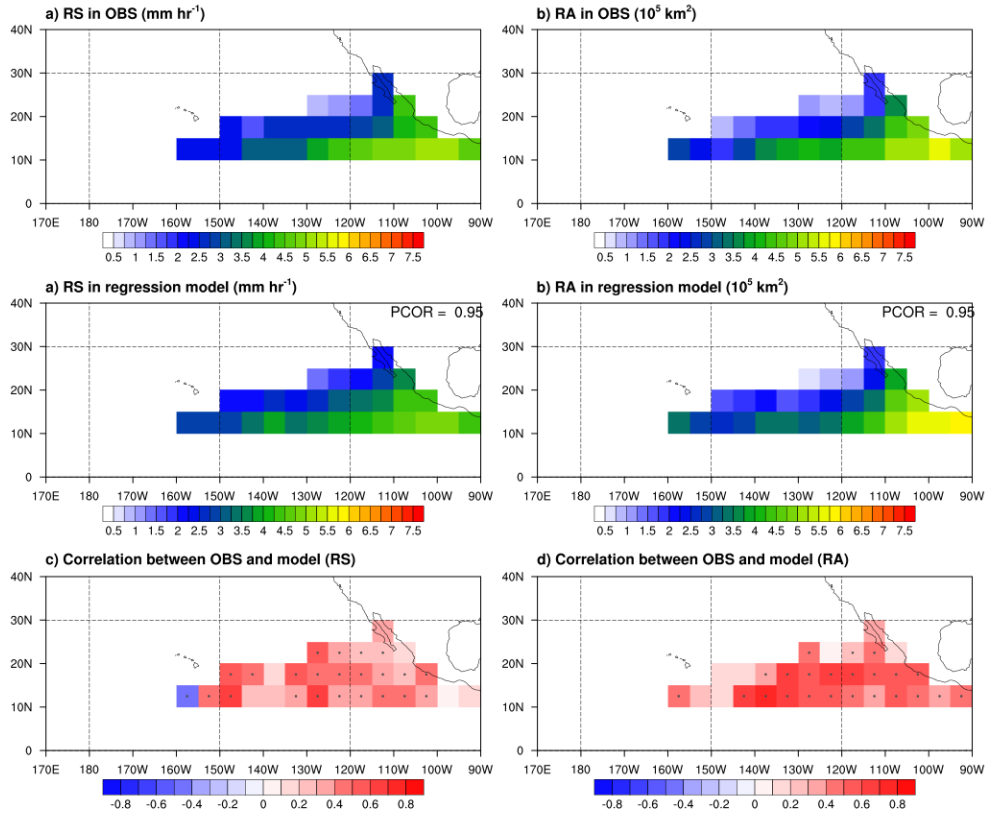

Fig. 3.2.29. Same as Fig. 3.2.27, but for the EP.

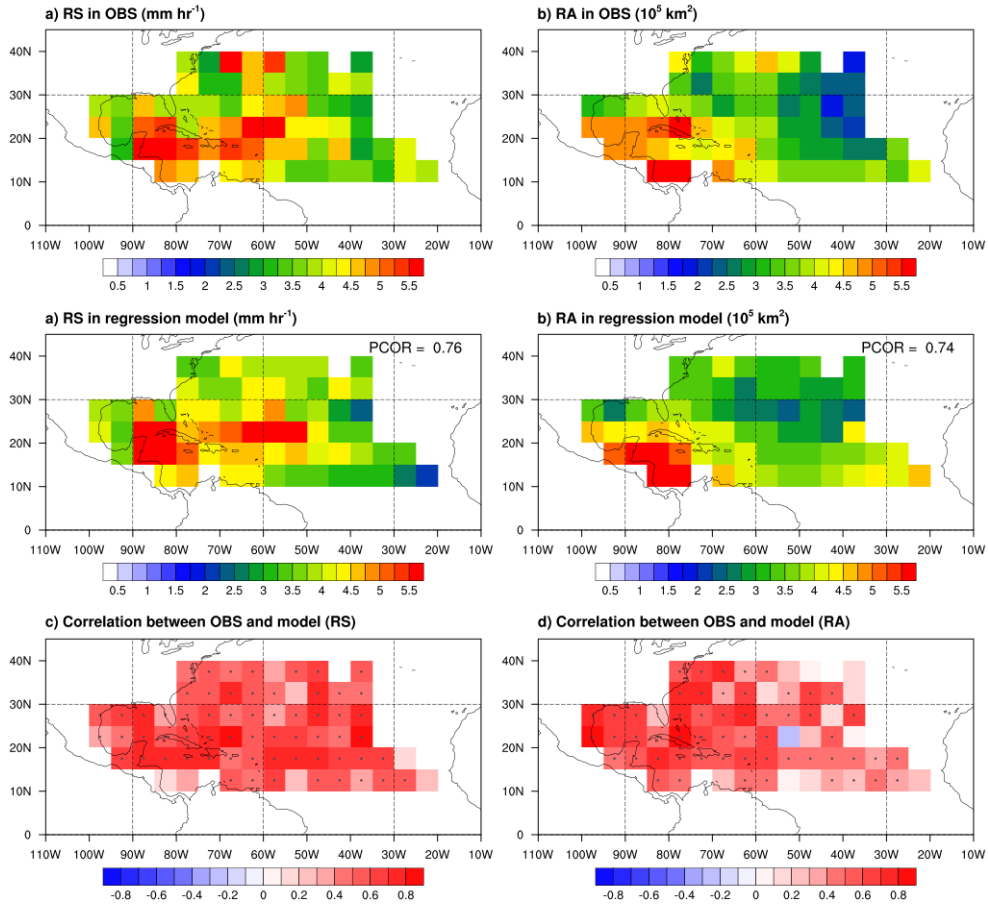

Fig. 3.2.30. Same as Fig. 3.2.27, but for the NA.

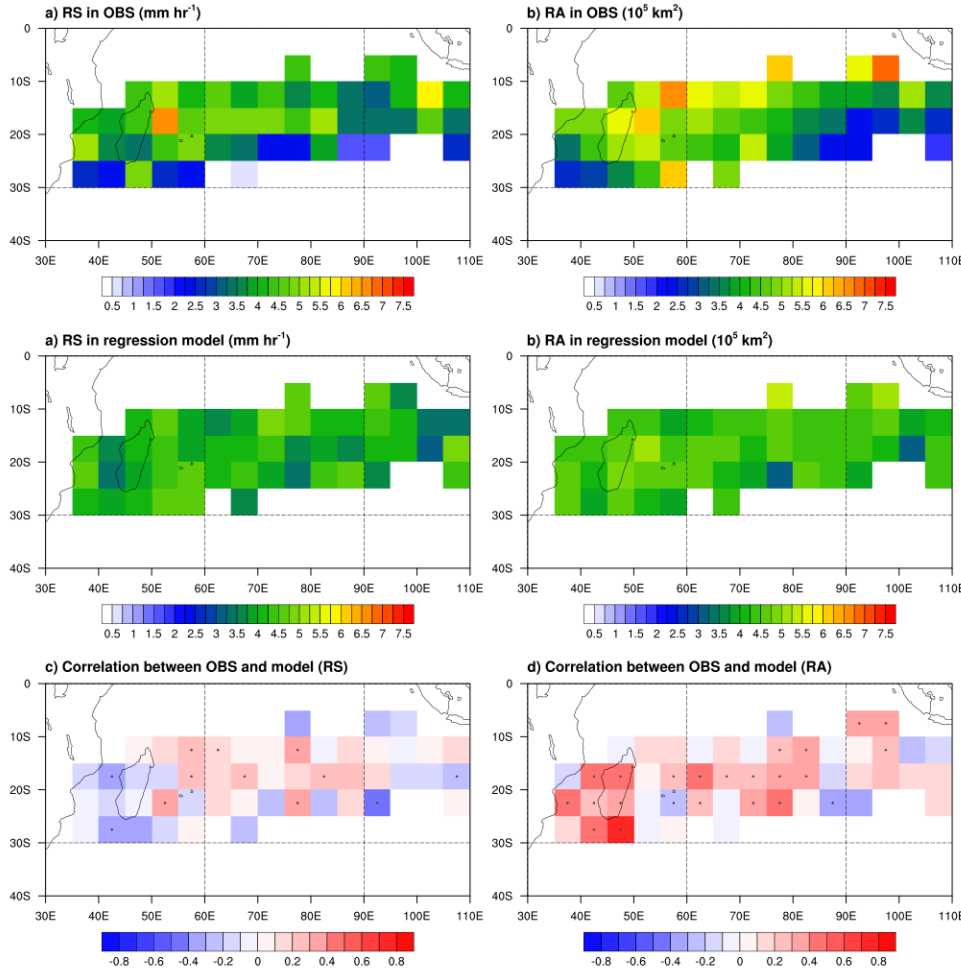

Fig. 3.2.31. Same as Fig. 3.2.27, but for the SI.

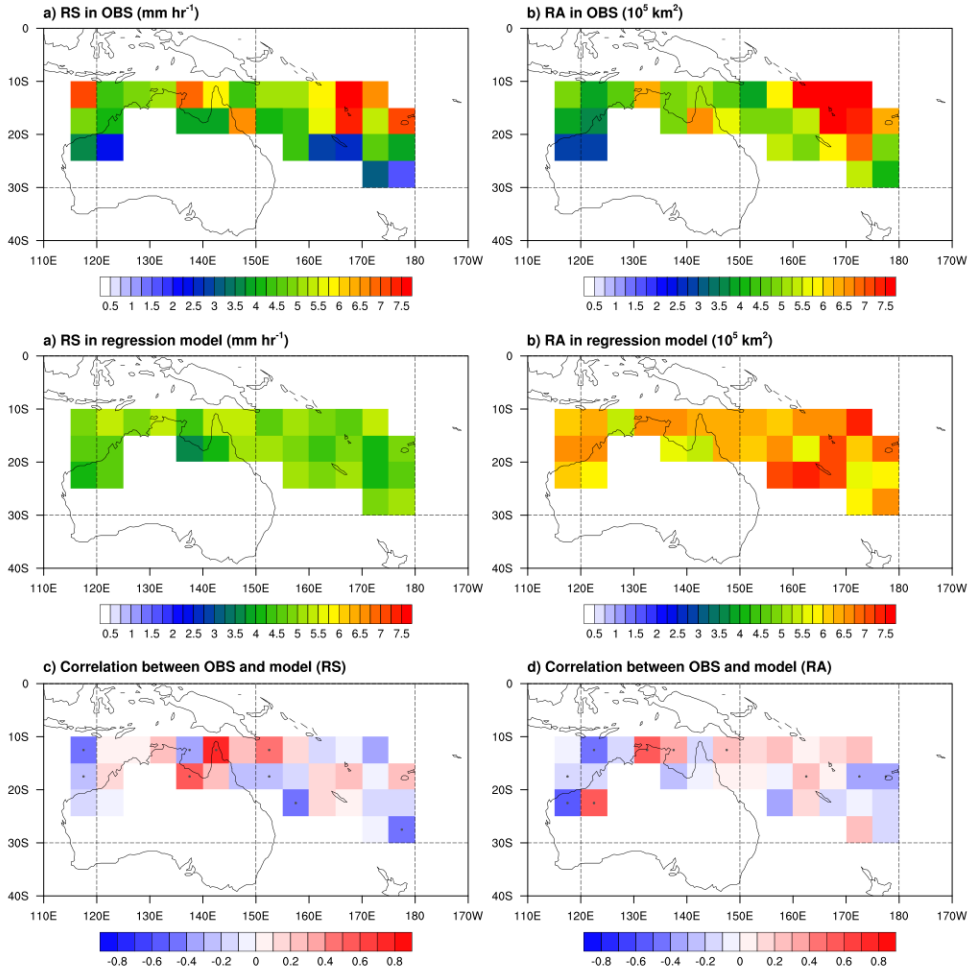

Fig. 3.2.32. Same as Fig. 3.2.27, but for the SP.

4. Future Changes in Tropical Cyclone Rainfall

4.1. Evaluation of Tropical Cyclone Rainfall in the HiFLOR Model

Prior to investigate future changes in TC rainfall projected by the HiFLOR, feasibility of the model to simulate TC rainfall should be evaluated. To check whether the model simulates realistic TC rainfall, global climatology of TC rainfall in the CTL experiment of HiFLOR was validated. The climatology of large-scale environmental conditions related to the variation of TC rainfall in the model were also evaluated. Lastly, the relationships between TC rainfall and controlling factors in the model were compared with those in the observation. Track and intensity of TCs simulated by the HiFLOR will not covered in this section, since they have been validated in previous studies (Murakami et al., 2015, 2016).

4.1.1. Climatology of TC Rainfall

Figure 4.1.1 presents the mean distributions of TC rainfall over the globe and the six ocean basins in CTL experiment of HiFLOR. Overall characteristics of TC rainfall in CTL experiment, such as intense rainfall in the inner-core region, rainfall pattern of outer region, variations of rainfall intensity and spatial scale according to basins, resemble those in observation (Fig. 3.1.1). The most distinct difference of TC rainfall between the model

and observation appears in the inner-core region. The global mean and standard deviation of RS in the model are 9.00 and 8.70 mm hr^{-1}, respectively. Thus, RS in the model is about 2 times larger than that in the observation (Table 3.1.1). Overestimation of the RS in the model appears regardless of the basin. The ratio of mean RS in the model to that in the observation ranges from 1.3 to 2.0 according to basins (Table 4.1.1). On the other hand, the RA in the model is more realistic than the RS. The global mean and standard deviation of RA in the model are 4.40 and 2.38 $\times 10^5$ km^2, respectively, which is similar to the values in observation (Table 3.1.2). The ratio of mean RS in the model to that in the observation ranges from 0.8 to 1.0 according to basins (Table 4.1.2).

The overestimation of RS in the HiFLOR may be attributed to the following reason. Most studies and operational forecast on TC activity focus on the accuracy of the TC track and intensity (i.e., V_{max}). Numerical models with high resolution of several kilometers is required to simulate TC intensity realistically (e.g., Fierro et al., 2009; Gentry and Lackmann, 2010; Manganello et al., 2012). HiFLOR model reasonably simulates TC intensity (Murakami et al. 2016), although this model has 25 km resolution. The resolution of HiFLOR is finer than that of other GCMs used in climate simulation, but not enough to simulate TC intensity in real world. Thus, physics schemes of HiFLOR may be tuned to enhance TC intensity. As more latent heat is released near the center of TCs, the kinetic energy (i.e., V_{max}) also increases. In other words, the model may be able to simulate the V_{max}

close to observed value by overestimating the rainfall in the inner-core region. Therefore, caution is needed to interpret the quantitative change in RS predicted by the model.

Figure 4.1.2 shows the spatial distribution of mean RS and RA in the model. Although the model generally overestimates RS, spatial patterns of RS and RA is similar to those in the observation (Figs. 3.1.2 vs. 4.1.2). Note that the observation is limited from 40°S to 40°N, and the model overestimates TC activity over the Central Pacific. Thus, the comparisons of the model and observation were made only for regions where TC activity exist in both model and observation. The pattern correlations of RS and RA between the model and observation are 0.50 and 0.83, respectively. The model particularly overestimates RS in the western part of the WP, which can reduce the pattern correlation of RS. On the other hand, the distribution of RA in the model is remarkably similar to that in the observation in terms of magnitude and pattern.

Zonal and meridional distributions of RS, and RA in CTL experiment are displayed in Fig. 4.1.3. The meridional variations of RS and RA in the model are similar to those in the observation (Figs. 3.1.3a–b vs. 4.1.3a–b). It is notable that RA in mid-latitudes increases with latitude in the model, which can be found in observed TCs in the Northern Hemisphere. There is distinct difference in zonal distribution of RS between the model and observation, particularly from 120 to 210°E due to the westward shifted location of maximum RS over the WP. The model and observation generally show

similar distributions of RA in zonal direction, except the location of maximum RA near 150–200°E. General characteristics of monthly variations in RS and RA in the model (Figs. 4.1.4 and 4.1.5) also resemble those in the observation (Figs. 3.1.4 and 3.1.5). Overall results suggest that HiFLOR can reasonably simulate spatial and temporal variations of RS and RA.

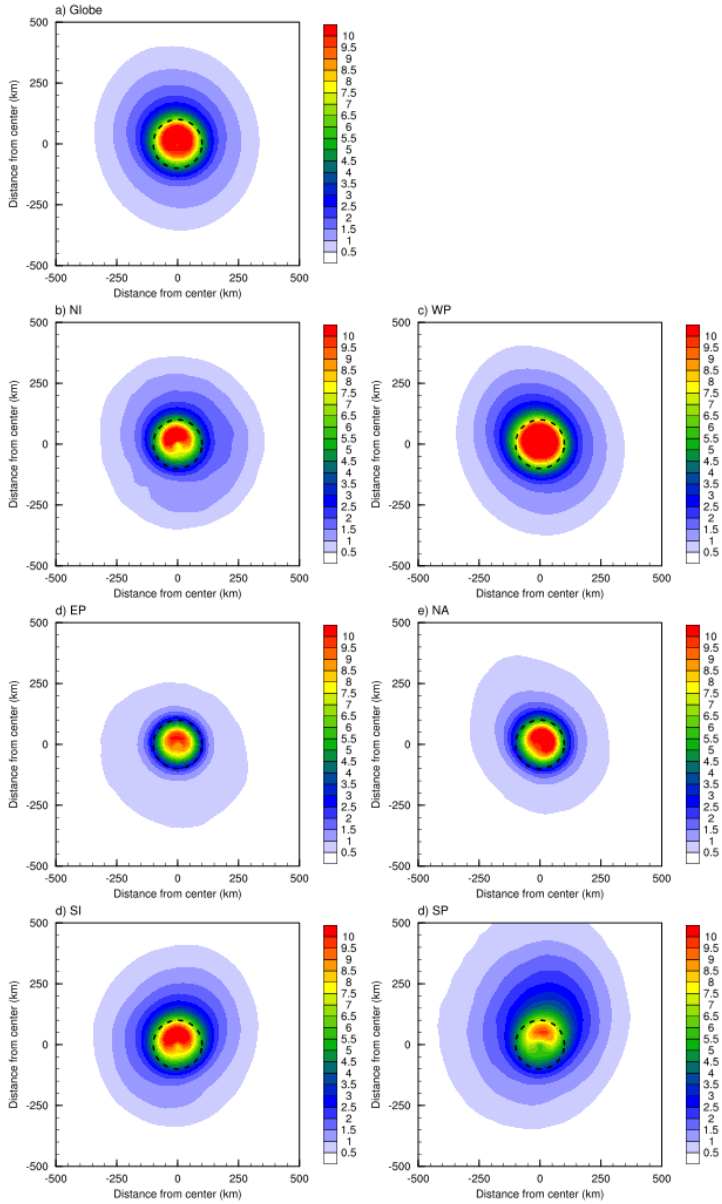

Fig. 4.1.1. The mean distribution of TC rainfall (unit: mm hr^{-1}) over the a) globe, b) NI, c) WP, d) EP, e) NA, f) SI, and g) SP in the CTL experiment. The directions of x- and y- axis are right and front to TC motion, respectively. The dashed circle indicates the inner-core region of TCs.

Table 4.1.1. Statistics of the RS (unit: mm hr^{-1}) over the globe, and the six ocean basins in the CTL experiment.

	Mean	Standard deviation	25%	median	75%
Global	9.00	8.70	4.70	7.72	12.03
NI	7.47	3.70	4.89	6.96	9.40
WP	10.34	8.25	5.44	9.07	13.92
EP	6.40	3.75	3.79	5.66	8.22
NA	7.72	4.82	4.18	6.65	10.29
SI	7.89	12.66	4.41	7.12	10.58
SP	6.52	4.59	3.13	5.73	8.87

Table 4.1.2. Same as Table 4.1.2, but for the RA (unit: 10^5 km^2).

	Mean	Standard deviation	25%	median	75%
Global	4.40	2.38	2.63	4.05	5.81
NI	3.95	1.93	2.54	3.68	5.14
WP	4.70	2.40	2.91	4.35	6.11
EP	3.06	2.20	1.19	2.56	4.50
NA	3.21	1.69	1.98	2.93	4.14
SI	4.28	2.24	2.60	3.95	5.62
SP	5.46	2.56	3.57	5.13	7.05

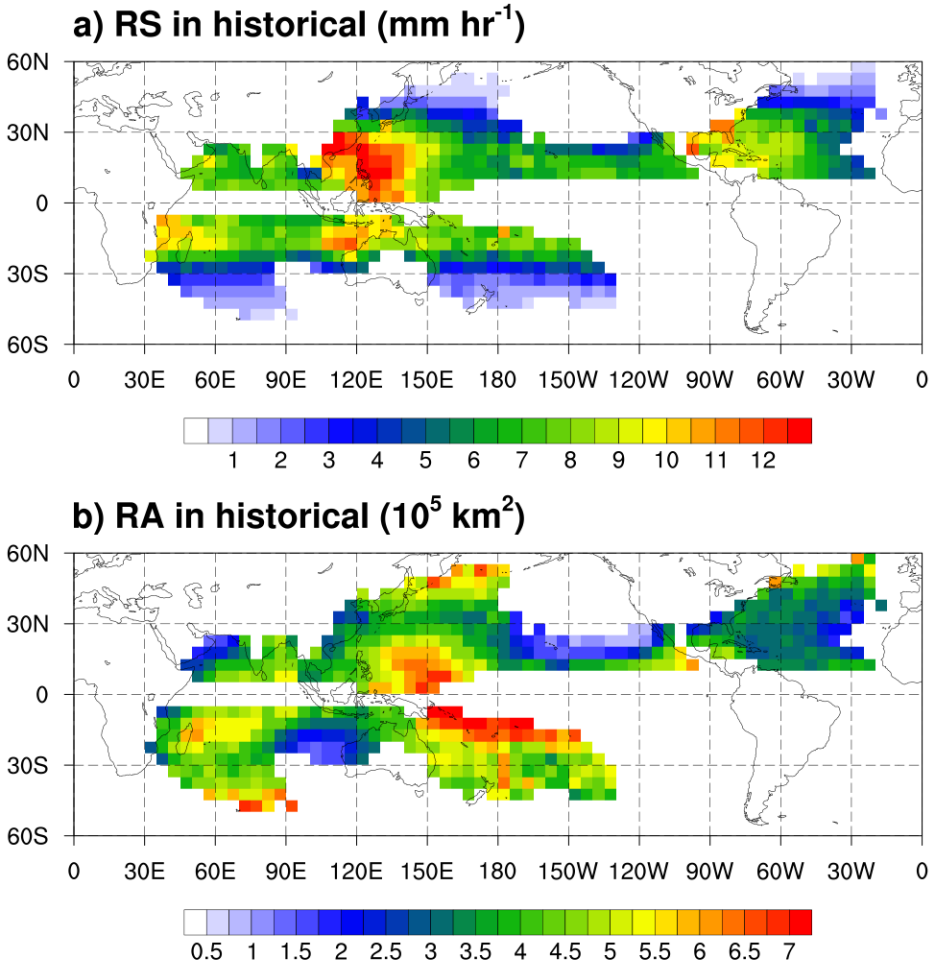

Fig. 4.1.2. Spatial distributions of the mean a) RS, and b) RA in the CTL experiment. The mean value in each 5-degree grid box is calculated from the TCs of which centers are located in the grid box. Only grid boxes with sample numbers larger than 20 are presented here.

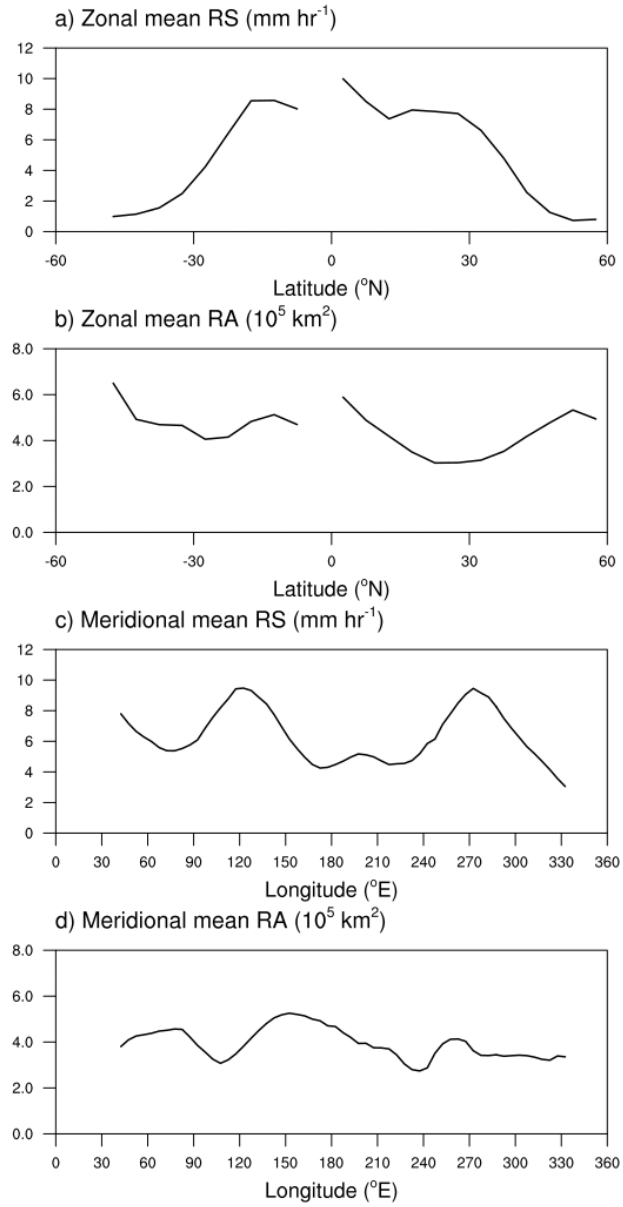

Fig. 4.1.3. a–b) Zonal and a–b) meridional mean of RS, and RA in the CTL experiment.

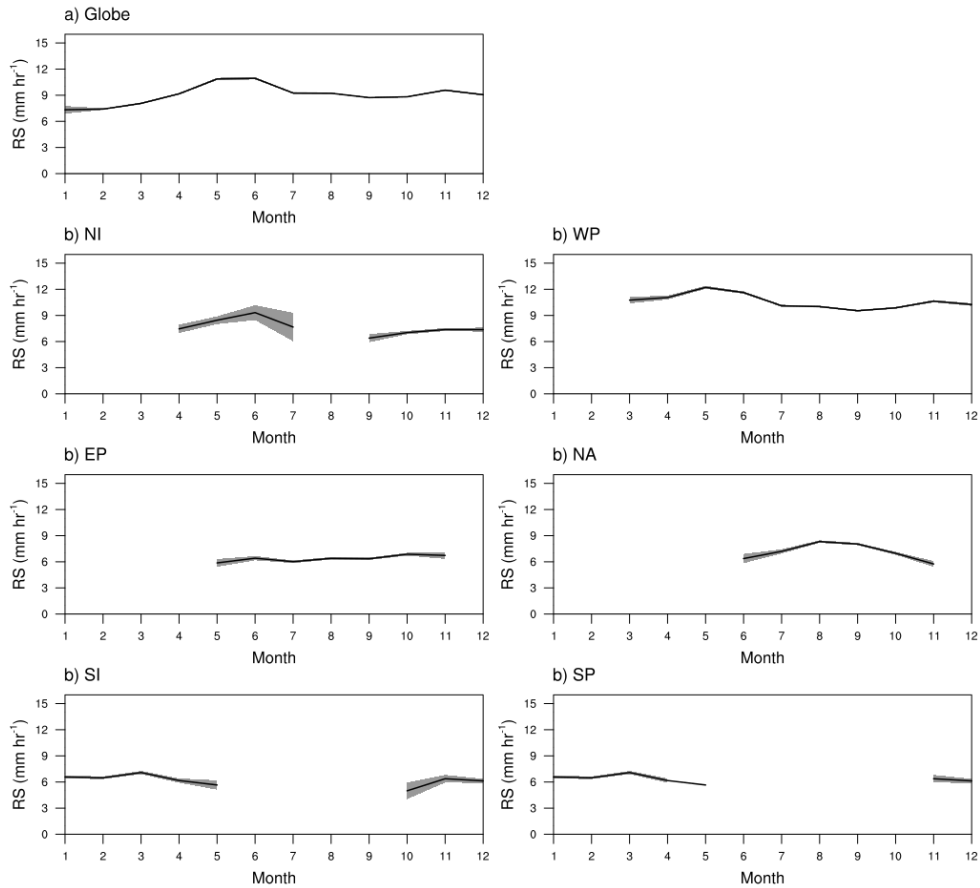

Fig. 4.1.4. Monthly distribution of RS over the globe, and the six basins. The 95% significance interval of the mean value is plotted in dark gray.

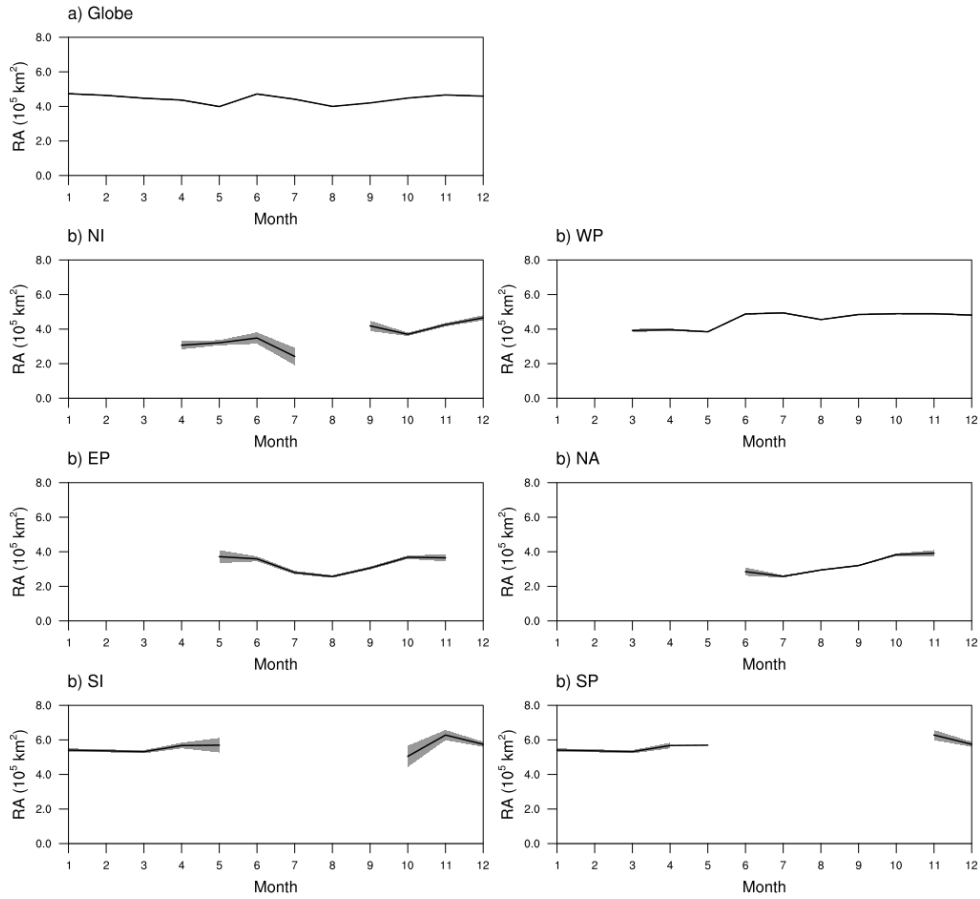

Fig. 4.1.5. Monthly distribution of RA over the globe, and the six basins. The 95% significance interval of the mean value is plotted in dark gray.

4.1.2. Climatology of Large-scale Environments

For reliable projection of future changes in TC rainfall according to global warming, the model should simulate controlling factors related to TC rainfall reasonably. Figures 4.1.3 and 4.1.4 show the mean distributions of V_{max} and seven environmental conditions in the observation and CTL experiment. The pattern correlations between the model and observation rage from 0.51 to 0.97. Therefore, the model generally simulates reasonable distributions of controlling factors related to TC rainfall. Similar to the RS, the model overestimates V_{max} in the western part of the WP. The similarity between observation and model for the distribution of V_{max} is the lowest (i.e., pattern correlation = 0.51). This result implies the biased distributions of RS and V_{max} may be related together.

Figures 4.1.8–4.1.10 suggest the relationships between TC rainfall and its controlling factors in the observation and simulations. The RS in CTL experiment show the strongest relationship with V_{max}, and has relatively weak relationship with environmental conditions (white bars in Fig. 4.1.8). In contrast, RA in CTL experiment has robust relationship with large-scale environments rather than V_{max} (white bars in Fig. 4.1.9). These results are consistent to the observation (black bars in Figs. 4.1.8 and 4.1.9). In particular, non-linear relationship between RA and environmental conditions is accurately simulated in the model. The relationship between RA and environmental flows (i.e., VWS and STEER) get stronger in the mid-latitudes than tropics (white bars in Figs 4.1.9 vs. 4.1.10). Meanwhile, the relationship

between RA and thermodynamic environments (e.g., SST and RH700) become significant in the tropics. These relationships between TC rainfall and controlling factors are consistently found in RCP4.5 experiment (gray bars in Figs. 4.1.8–4.1.10). The overall results indicate that HiFLOR can realistically simulate the factors and mechanisms associated with variation of TC rainfall. Thus, possible reasons for future changes in TC rainfall can be suggested from the change in the controlling factors.

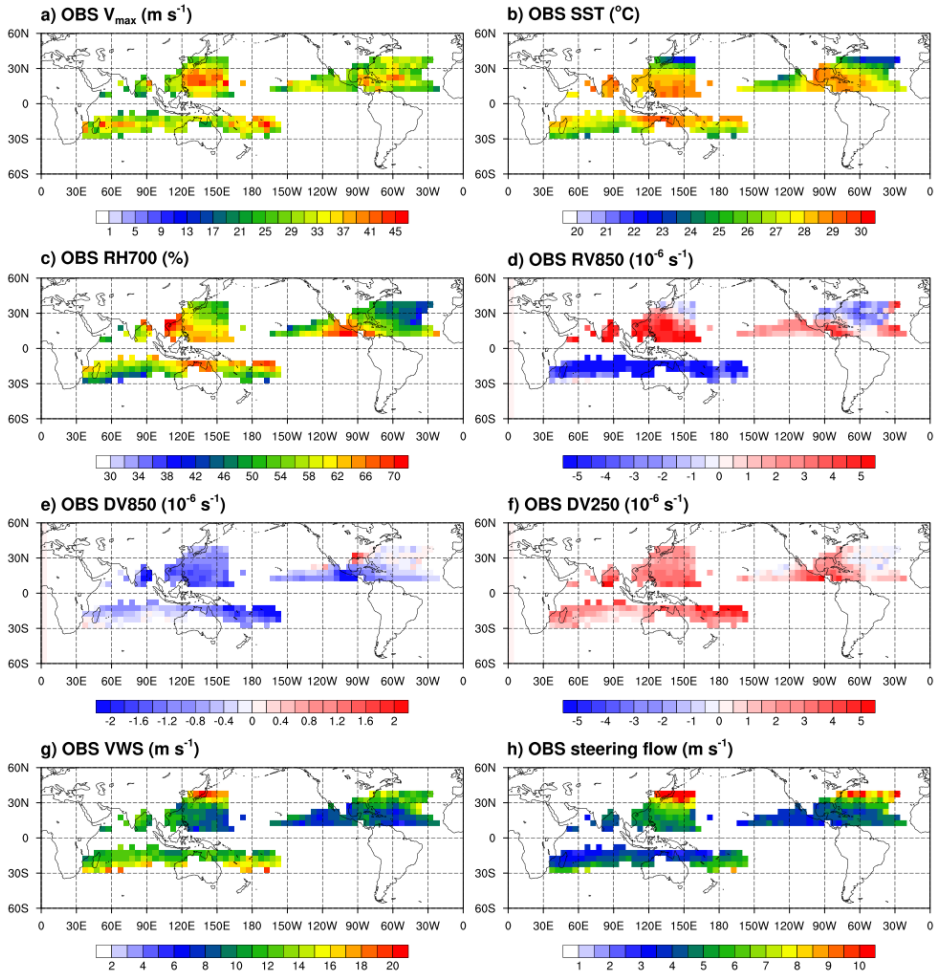

Fig. 4.1.6. Spatial distributions of the mean a) Vmax, b) SST, c) RH700, d) RV850, e) DV850, f) DV250, g) VWS, and h) STEER in the observation. The mean value in each 5-degree grid box is calculated from the TCs of which centers are located in the grid box. Only grid boxes with sample numbers larger than 20 are presented here.

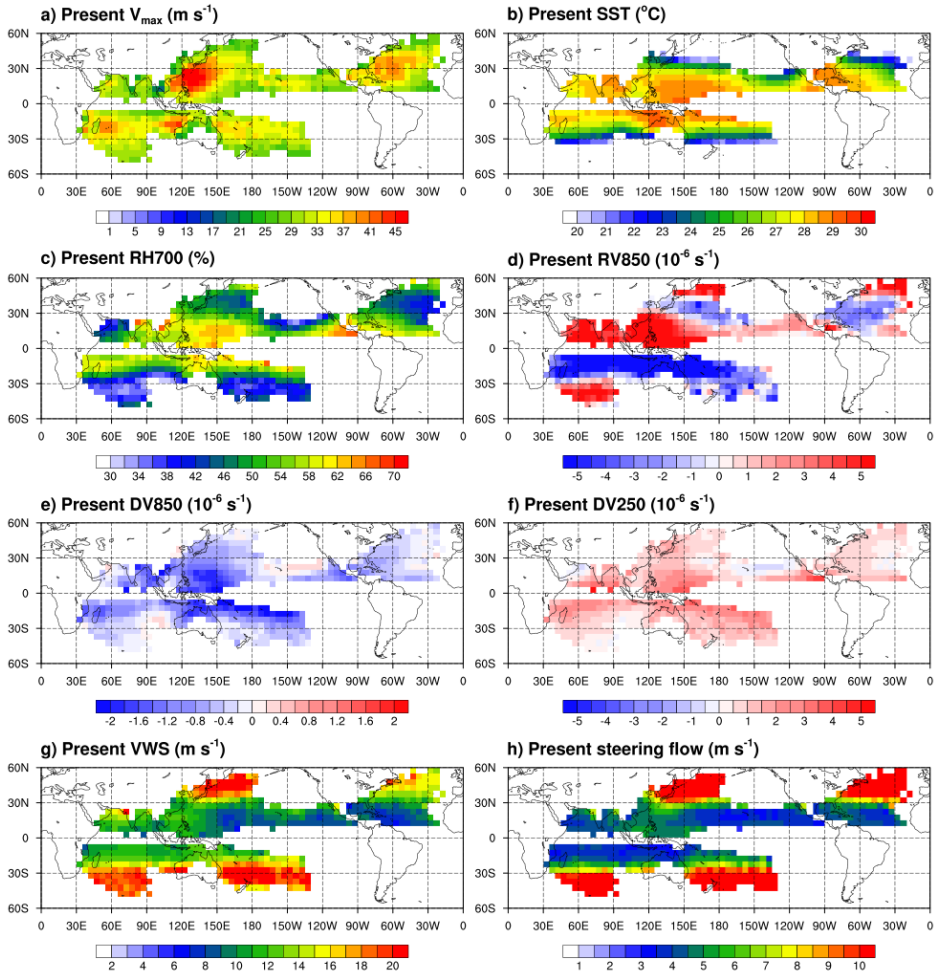

Fig. 4.1.7. Same as Fig. 4.1.6, but for the CTL experiment.

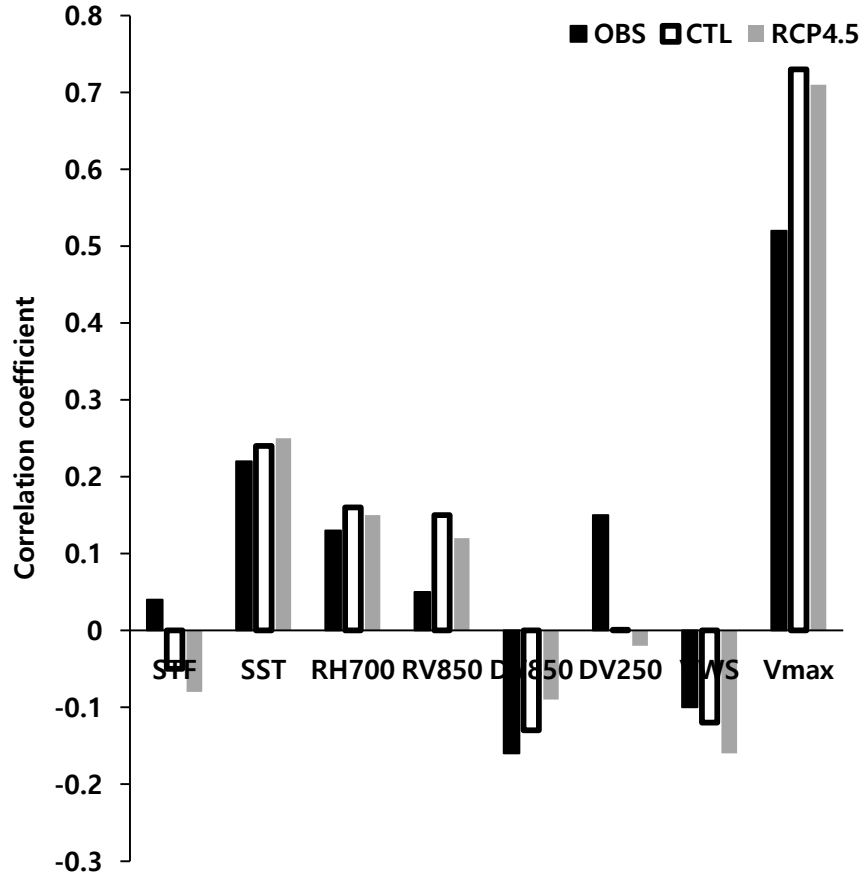

Fig. 4.1.8. Correlation coefficients between RS and multiple parameters (i.e., SST, RH700, RV850, DV850, DV200, VWS, STEER, and V_{max}) for the observation, control, and RCP 4.5 experiments (OBS, CTL and RCP4.5; black, white, and gray, respectively).

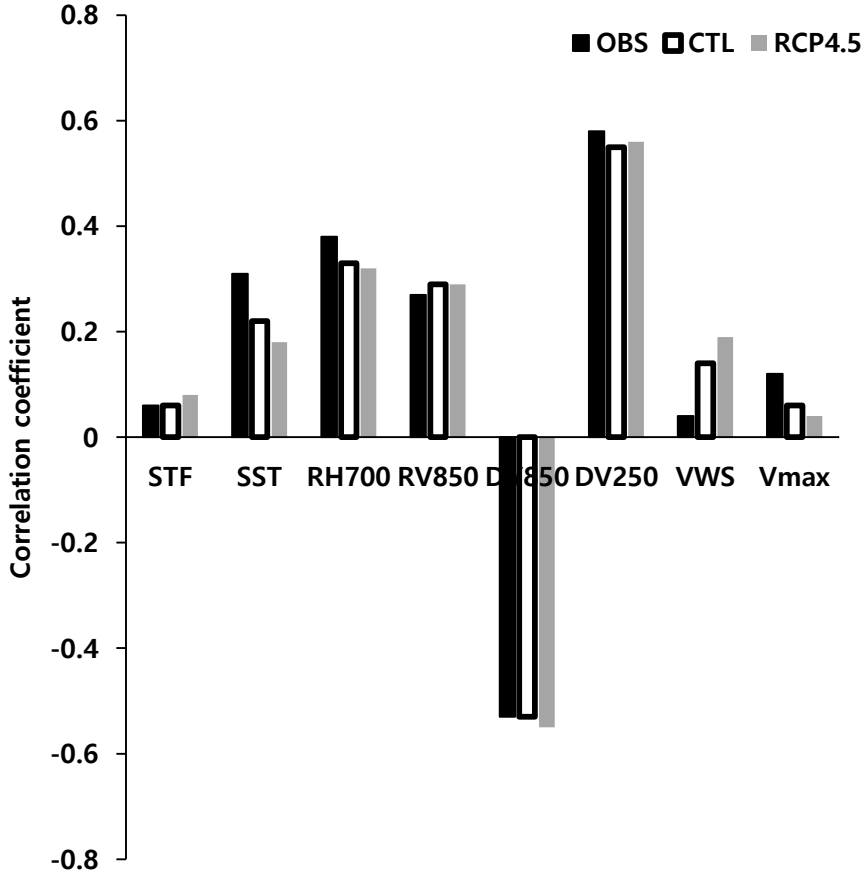

Fig. 4.1.9. Same as Fig. 4.1.8, but for the RA in the tropics.

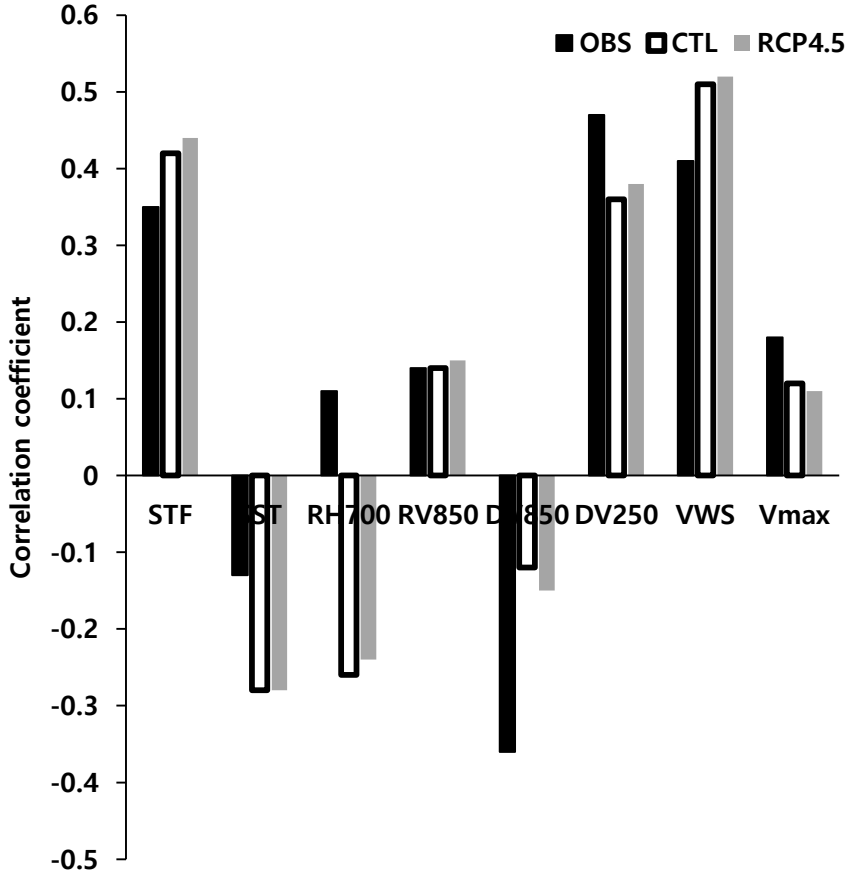

Fig. 4.1.10. Same as Fig. 4.1.8, but for the RA in the mid-latitudes.

4.2. Tropical Cyclone Rainfall under Global warming

Characteristics of TC rainfall are related to TC wind, and various environmental conditions (Section 3.2). A number of global warming scenarios projected changes in TC wind and large-scale environmental conditions in future climate. Thus, it is natural to expect TC rainfall to change under global warming. In this section, future changes in TC rainfall under RCP4.5 scenario were projected by HiFLOR. Possible mechanisms for future changes in TC rainfall were investigated based on the understanding of factors controlling TC rainfall.

4.2.1. Changes in TC Rainfall

Table 4.2.1 presents future changes in RS and RA in the globe and six ocean basins. Globally, RS significantly increases by 1.59 mm hr^{-1} (17.7% relative to CTL) in future climate. Also, RS increases in all ocean basins, and the increasing rates range from 16.3 to 28.3%. On the other hand, RA shows very small change in global (3.0×10^3 km^2, 0.7% increase from CTL). The NI, EP, NA, and SI present statistically significant increase of RA, but only the EP shows large increasing rate (10.8%). Figure 4.2.1 shows spatial distributions of changes in RS and RA. The RS presents homogeneous increase in global with changing rate from 10 to 40%. In contrast, change in RA appears inhomogeneous with regional increase and decrease. In other

words, the RA does not change greatly across the globe or individual basin, but the change can be significant locally.

Future changes in RA seems complicated in spatial pattern, but this pattern can be simplified if the samples are divided into mid-latitudes and tropical regions (Fig. 4.2.2). RS increases in both tropics and mid-latitudes, but increases more in the tropics than in mid-latitudes. On the other hand, the change in RA is a wave-like pattern in the east-west direction in the tropics, but increases uniformly in the mid-latitudes. The increases of RA in 30–80°E, 180–260°E are closely related to TCs in the Arabian Sea, and the EP (Figs. 4.2.1 and 4.2.2b). The decrease of RA in 100–180°E, 260–300°E are closely related to TCs in the Maritime Continent (MC), and the NA (Figs. 4.2.1 and 4.2.2b). As discussed in Section 3.2.3, factors affecting RA differ in the tropics and mid-latitudes. Thus, the causes of changes in RA in the two regions may be different.

Table 4.2.1. Mean RS and RA in RCP4.5 experiment, and their differences from CTL experiment. Asterisks denote differences significant in 95% confidence level. Ratio of the difference to the mean value of CTL experiment is provided in parentheses.

	RS ($mm\ hr^{-1}$)		RA ($10^5\ km^2$)	
	Mean	Difference from CTL	Mean	Difference from CTL
Global	10.59	1.59* (17.7%)	4.43	0.03* (0.7%)
NI	9.16	1.69* (22.6%)	4.03	0.08* (2.0%)
WP	12.03	1.69* (16.3%)	4.68	–0.02 (–0.4%)
EP	8.21	1.81* (28.3%)	3.39	0.33* (10.8%)
NA	9.43	1.71* (22.2%)	3.29	0.08* (2.5%)
SI	9.68	1.79* (22.7%)	4.33	0.05* (1.2%)
SP	8.13	1.61* (24.7%)	5.40	–0.06 (–1.1%)

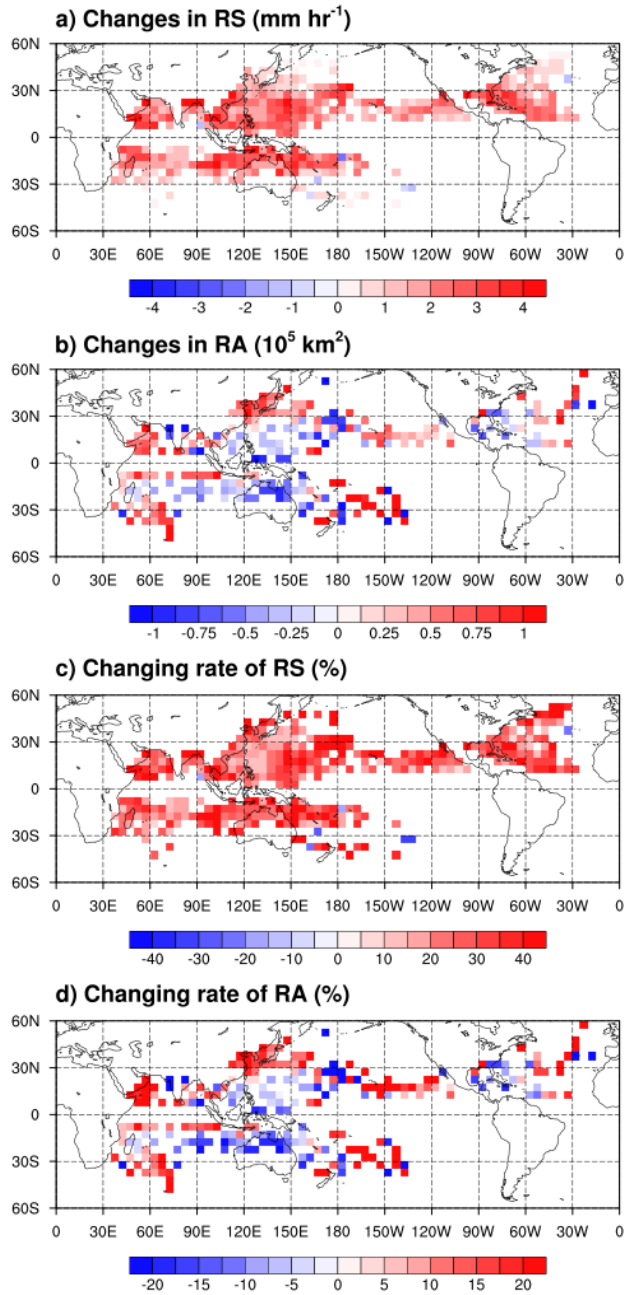

Fig. 4.2.1. Difference of mean a) RS and b) RA between RCP4.5 and CTL experiments (RCP4.5 minus CTL). Changing ratios of RS and RA are provided in c) and d). Only grid points in which the difference is significant in 95% confidence level.

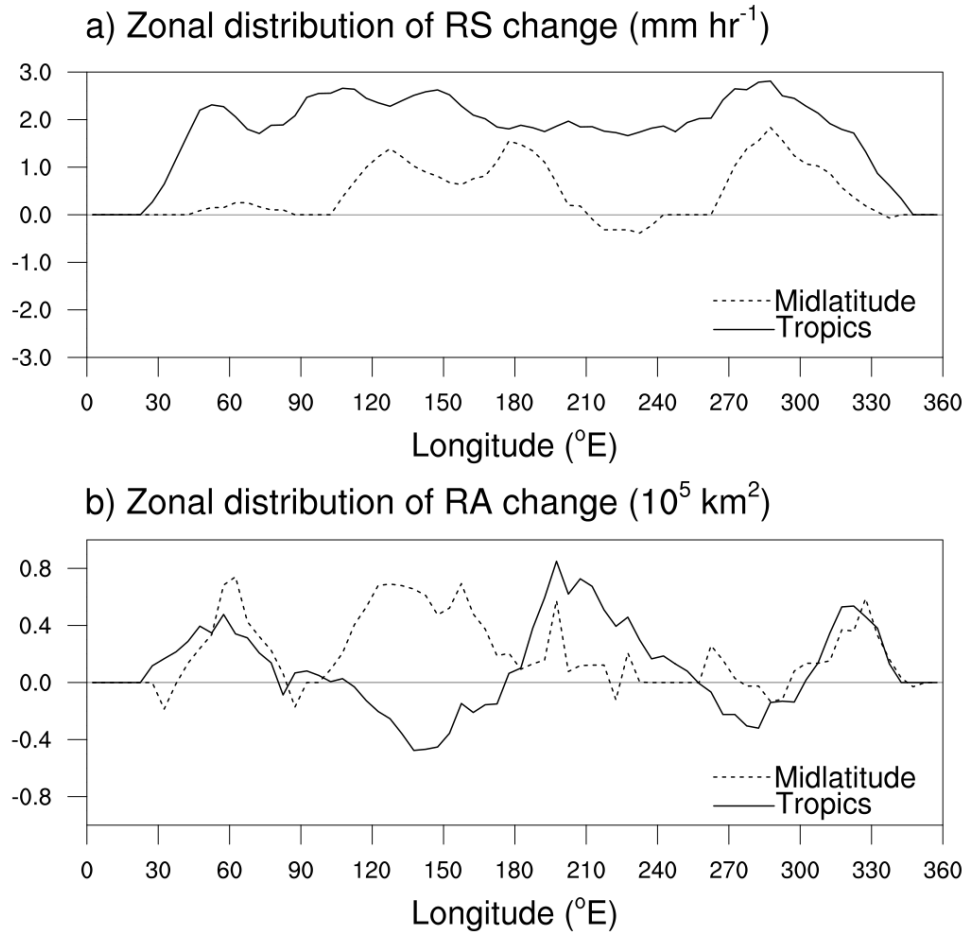

Fig. 4.2.2. Zonal distribution of changes in a) RS and b) RA averaged in the tropics (solid line) and mid-latitudes (dashed line).

4.2.2. Possible Mechanisms for the Changes in TC Rainfall

Future changes in TC rainfall can be associated to changes in controlling factors. Figure 4.2.3 shows the future changes in factors affecting TC rainfall. Under global warming, V_{max} and SST increase globally and homogeneously, which is also common in previous studies (e.g., Vecchi and Soden, 2007a, Knutson et al., 2010, Emanuel, 2013). The most influential factor for RS is the V_{max} (Sections 3.2.1 and 3.2.2). Variation of RS is also related to SST. Thus, global increase in V_{max} and SST can cause a homogeneous increase in RS.

Since RA is strongly affected by surrounding environmental conditions, future changes in large-scale environmental conditions may be crucial for RA change. Figure 4.2.4 displays changes in large-scale circulation in the lower and upper troposphere. In the lower troposphere, divergent flows appear the Maritime Continent (MC). Easterly toward the Indian Ocean, and westerly toward the EP occurs from the MC. In the EP, on the other hand, the wind from east and west converges. In the upper troposphere, air converges to the MC and diverges from the EP. This change in tropical circulation is a typical pattern of the Weakening of Walker Circulation (WWC). The emergence of WWC in future climates is associated with El-Niño like SST warming and is commonly predicted in various global warming scenarios (e.g., Held and Soden, 2006, Vecchi et al., 2006, Vecchi and Soden, 2007b).

The impact of the WWC appears not only in the tropical Pacific but also in the Indian and Atlantic Ocean. In the lower troposphere, the easterlies from

the MC to the Indian Ocean induce anti-cyclonic gyres in the North and South Indian Oceans. The westerlies from the MC to the EP induce cyclonic gyres in the North and South EP. On the continent of North America, anti-cyclonic gyres associated with cyclonic gyres in the North EP appear. In the upper troposphere, the gyres in the opposite direction to the lower ones appear, except for the South Indian Ocean.

In the Arabian Sea (AS), located on the western boundary of the anti-cyclonic gyre, lower convergence and upper divergence are induced (Figs. 4.2.3e–f). Increase of SST and RH700 is also significant in this region (Figs. 4.2.3b–c). Thus, the easterlies from the MC converges moisture and heat and promotes upward motion in the AS, which is a favorable condition for RA increase. In the MC, WWC causes lower divergence and upper convergence, leading to large-scale downward motion and decreasing RH700. Therefore, the RA of the MC decreases. The cyclonic gyre appears in the north EP, especially the TC activity appears over the eastern boundary of the cyclonic gyre. To the east of the cyclonic gyre, RH700, RV850, and lower convergence significantly increase, which can increase RA. In the NA, TCs are affected by anti-cyclonic gyres. In this region, RH700 and RV850 decrease, and downward motion are enhanced due to lower divergence and upper convergence. Such environmental conditions can reduce RA in the NA. Overall results suggest that WWC are responsible for the wave-like pattern of changes in RA in the tropics.

TCs in mid-latitudes do not appear to be directly affected by the WWC. In mid-latitudes, influence of the V_{max}, VWS, and STEER on RA is significant. The V_{max} increases homogeneously. The VWS and STEER in mid-latitudes also markedly increase in the Southern Hemisphere. This change can contribute to the homogeneous increase of RA in mid-latitude.

Summing up, a homogeneous increase in RS in future climates can be associated with a homogeneous rise in V_{max} and SST. Wave-like changes in RA in the tropics may be affected by changes in the large-scale environmental conditions associated with the WWC. In addition, homogeneous increase in V_{max} and environmental flows in the Southern Hemisphere may increase RA in mid-latitudes.

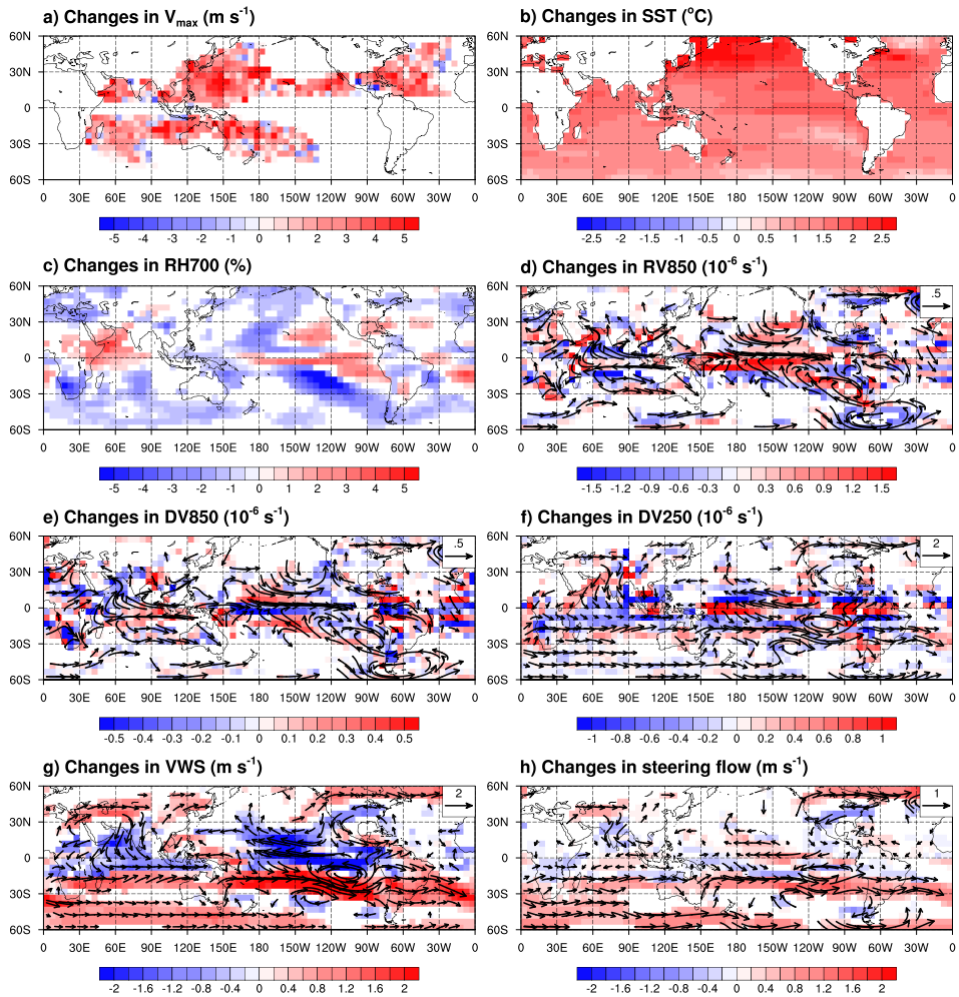

Fig. 4.2.3. Future changes in a) Vmax, b) SST, c) RH700, d) RV850, e) DV850, f) DV250, g) VWS, and h) STEER. Arrows indicate the vectors of wind, shear, and steering flow in d–h). Only grid points in which the difference is significant in 95% confidence level.

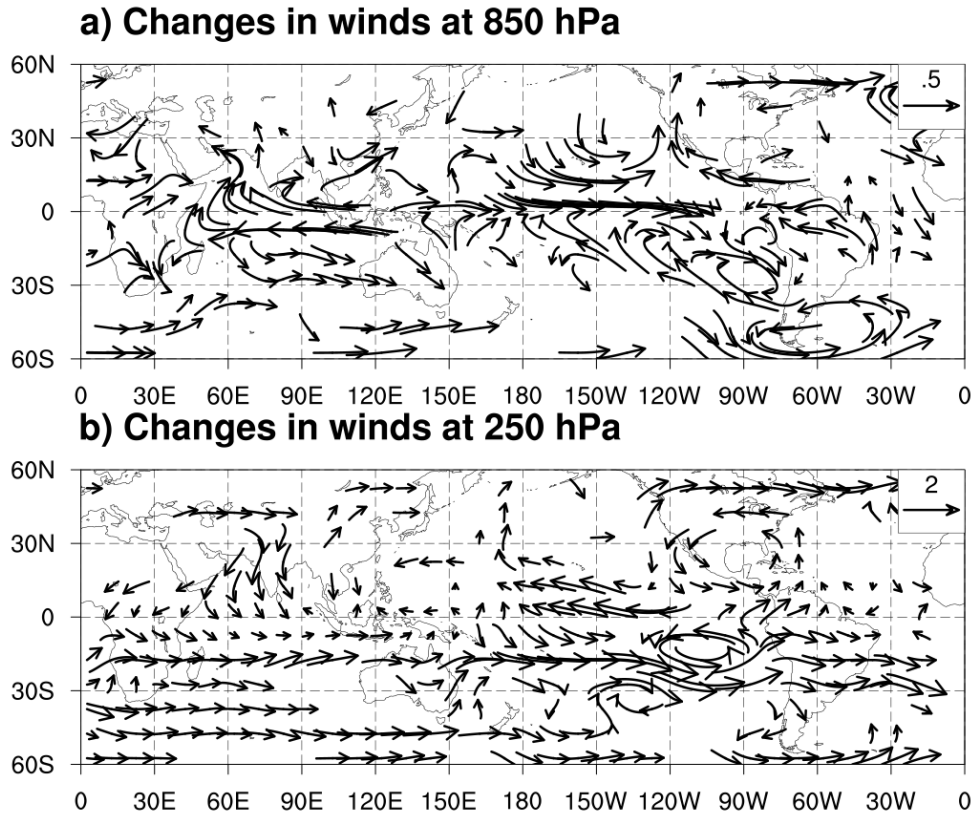

Fig. 4.2.4. Future changes in winds at a) 850 hPa, and b) 250 hPa level. Only wind vector in which the change is significant in 95% confidence level.

5. Concluding Remarks

The first goal of this study is to reveal climatology of TC rainfall and mechanisms for its variation over the globe. Characteristics of TC rainfall were investigated based on two indices, inner-core rainfall strength (RS) and total rainfall area (RA) obtained from TRMM-3B42 precipitation data during 1998–2013. Globally, the mean RS, and RA are 4.43 mm hr^{-1}, and 4.75×10^{5} km^{2}, respectively. RS and RA significantly vary according to ocean basin. RS (RA) is large in order of the WP, SP, NI, SI, NA, and EP (SP, WP, NI, SI, NA, and EP). RS and RA generally decrease with latitude in the tropics, while RA increases with latitude in mid-latitudes. RS and RA also show large variation in zonal direction. Temporal variability of RS and RA was also significant. Monthly variations of RS and RA are noticeable in the NI, WP, NA, while those in the EP, SI, and SP is unclear. It was noted that RS significantly decreases with time (–0.081 mm hr^{-1} yr^{-1}; –1.8% yr^{-1}) in global, while RA does not change. The decrease of RS is evident in the EP, NA, and SI. The global climatology of TC rainfall suggested in this study can be used as a basic information for development or evaluation of TC rainfall forecast.

This study investigated various factors which can affect rainfall structure of TCs, to understand the mechanisms for the variation of TC rainfall. First of all, the relationship between TC rainfall and the primary circulation (i.e., V_{max}) was investigated. Regardless of the basin, RS show robust relationship

with V_{max} (r = 0.32–0.62), while the relationship between RA and V_{max} is weak (r = 0.01–0.17). The upward motion induced by the primary circulation is the strongest in a very narrow region near the center of TC (e.g., eye wall). Thus, RS can be primarily affected by the primary circulation than other factors. On the other hand, the weak relationship between RA and the primary circulation suggests that rainfall in the outer region of the TC may be more affected by environmental conditions other than the primary circulation.

The relationships between TC rainfall and multiple environmental conditions were also investigated. Generally, RS has significant relationships with SST, RH700, DV850, DV200, and VWS, but they are weaker than the relationship between RS and V_{max}. On the other hand, RA has robust relationship with environmental conditions, particularly for DV850, DV200, SST, RH700, and RV850. This result confirms that rainfall in the outer region of a TC is more sensitive to environments surrounding the TC than the primary circulation. In addition, factor analysis reveals that the environmental conditions affecting TC rainfall can be classified as large-scale low (or high) pressure systems, and environmental flows with sea surface temperature.

Non-linear response of TC rainfall to environments was also found in the tropics and mid-latitudes. In mid-latitudes, RA is primarily affected by environmental flows (i.e., VWS and STEER) rather than SST. The influence of environmental flows results in expansion of RA between the VWS and STEER. In contrast, RA has significant relationship with SST instead of environmental flows in the tropics. The different relationship between RA and

environmental flows is attributed to the different SST in the two region. TCs hardly get energy from cool SST in mid-latitudes, and become sensitive to environmental flows, which is vice versa in the tropics. Thus, environmental flows can be an important factor controlling RA in the mid-latitudes. The environmental flows also significantly affect wind and rainfall structure of TCs over South Korea where strong environmental flows prevail. TCs over South Korea has asymmetric wind and rainfall structures affected by the strong VWS. It was found that asymmetric convection within TC (i.e., rising/sinking motion in the downshear-left/upshear-right side) induced by the vertical wind shear. Consequently, RA over South Korea significantly increases with VWS.

Understanding on global climatology of TC rainfall and controlling factors of its variation can be useful for developing prediction models for TC rainfall. As an application of this study, multi-variable linear regression models for RS and RA over the six ocean basins were developed. The statistical models significantly explain variations of RS and RA in the NI, WP, EP, and NA including spatial distributions of mean and their variations. The predictors suggested in this study can be applied to other statistical models such as the R-CLIPER. In addition, the information of relationships between TC rainfall and controlling factors can help to improve TC rainfall prediction by numerical models. For accurate prediction of TC rainfall, the relationships between TC rainfall and controlling factors need to be simulated reasonably.

Thus, current results can be used in evaluation of TC rainfall predicted by numerical models.

Lastly, this study investigated changes in TC rainfall according to RCP4.5 scenario using a high-resolution coupled GCM (GFDL's HiFLOR). The HiFLOR reliably simulates spatial and temporal variations of TC rainfall in present climate, although RS is overestimated by the model. Climatology of controlling factors affecting TC rainfall simulated by the model resemble that in the observation. The relationships between TC rainfall and controlling factors in the model are also realistic. Thus, the model can be utilized in projection of future changes in TC rainfall. RS homogeneously increases over the globe, which is related to homogeneous increase of V_{max} and SST in future climate. On the other hand, the weakening of the Walker Circulation in future may cause the wave-like changes of RA in the tropics. Increase of RA in mid-latitudes seems to be related to homogeneous increase of V_{max} and environmental flows in the Southern Hemisphere.

References

Bender MA, Knutson TR, Tuleya RE, Sirutis JJ, Vecchi GA, Garner ST et al. (2010) Modeled impact of anthropogenic warming on the frequency of intense Atlantic hurricanes. Sci. 327(5964):454-458

Bhatia K, Vecchi G, Murakami H, Underwood S, and Kossin J (2018) Projected Response of Tropical Cyclone Intensity and Intensification in a Global Climate Model. Journal of Climate 31(20):8281-8303

Bosart LF, Bracken WE, Molinari J, Velden CS, and Black PG (2000) Environmental influences on the rapid intensification of hurricane Opal (1995) over the gulf of Mexico. Mon. Weather. Rev. 128(2):322-352

Chan JCL and Liang XD (2003) Convective asymmetries associated with tropical cyclone landfall. Part I: f-plane simulations. J. Atmos. Sci. 60(13):1560-1576

Chan KTF and Chan JCL (2015) Global climatology of tropical cyclone size as inferred from QuikSCAT data. Int. J. Climatol. 35(15):4843-4848

Chan KTF and Chan JCL (2012) Size and strength of tropical cyclones as inferred from QuikSCAT data. Mon. Weather Rev. 140(3):811-824

Changnon SA (2008) Assessment of flood losses in the United States. J. Contemp. Water. Res. Educ. 138(1):38-44

Chavas DR and Emanuel KA (2010) A QuikSCAT climatology of tropical cyclone size. Geophys. Res. Lett. 37(18):10.1029/2010gl044558

Chavas DR, Lin N, Dong W, and Lin Y (2016) Observed tropical cyclone size revisited. J. Climate 29(8):2923-2939

Chen SS, Knaff JA, and Marks FDJ (2006a) Effects of vertical wind shear and storm motion on tropical cyclone rainfall asymmetries deduced from TRMM. Mon. Weather Rev. 134(11):3190-3208

Chen SYS, Knaff JA, and Marks FD (2006b) Effects of vertical wind shear and storm motion on tropical cyclone rainfall asymmetries deduced from TRMM. Mon. Weather Rev. 134(11):3190-3208

Chen Y, Ebert EE, Walsh KJE, and Davidson NE (2013) Evaluation of TRMM 3B42 precipitation estimates of tropical cyclone rainfall using PACRAIN data. J. Geophys. Res. Atmos. 118(5):2184-2196

Chen Y and Yau MK (2003) Asymmetric structures in a simulated landfalling hurricane. J. Atmos. Sci. 60(18):2294-2312

Choi K-S, Kim B-J, Kim D-W, and Byun H-R (2009) Interdecadal variation of tropical cyclone making landfall over the Korean Peninsula. Int. J. Climatol. 30(10):1472-1483

Corbosiero KL and Molinari J (2002) The effects of vertical wind shear on the distribution of convection in tropical cyclones. Mon. Weather Rev. 130(8):2110-2123

Corbosiero KL and Molinari J (2003) The relationship between storm motion, vertical wind shear, and convective asymmetries in tropical cyclones. J. Atmos. Sci. 60(2):366-376

Czajkowski J, Simmons K, and Sutter D (2011) An analysis of coastal and

inland fatalities in landfalling US hurricanes. Nat. Hazards 59(3):1513-1531

Czajkowski J, Villarini G, Montgomery M, Michel-Kerjan E, and Goska R (2017) Assessing current and future freshwater flood risk from North Atlantic tropical cyclones via insurance claims. Sci. Rep. 7:41609

Dee DP, Uppala SM, Simmons AJ, Berrisford P, Poli P, Kobayashi S et al. (2011) The ERA-Interim reanalysis: configuration and performance of the data assimilation system. Quarterly Journal of the Royal Meteorological Society 137(656):553-597

Delworth TL, Rosati A, Anderson W, Adcroft AJ, Balaji V, Benson R et al. (2012) Simulated Climate and Climate Change in the GFDL CM2.5 High-Resolution Coupled Climate Model. Journal of Climate 25(8):2755-2781

DeMaria M (1996) The effect of vertical shear on tropical cyclone intensity change. J. Atmos. Sci. 53(14):2076-2088

Emanuel KA (2013) Downscaling CMIP5 climate models shows increased tropical cyclone activity over the 21st century. Proc. Natl. Acad. Sci. USA 110(30):12219-12224

Evans C, Wood KM, Aberson SD, Archambault HM, Milrad SM, Bosart LF et al. (2017) The extratropical transition of tropical cyclones. Part I: Cyclone evolution and direct impacts. Monthly Weather Review 145(11):4317-4344

Evans JL and Hart RE (2003) Objective indicators of the life cycle evolution

of extratropical transition for Atlantic tropical cyclones. Mon. Weather Rev. 131:909-925

Flatau M, Schubert WH, and Stevens DE (1994) The role of baroclinic processes in tropical cyclone motion: The influence of vertical tilt. J. Atmos. Sci. 51(18):2589-2601

Frank WM and Ritchie EA (1999) Effects of environmental flow upon tropical cyclone structure. Mon. Weather Rev. 127(9):2044-2061

Frank WM and Ritchie EA (2001) Effects of vertical wind shear on the intensity and structure of numerically simulated hurricanes. Mon. Weather Rev. 129(9):2249-2269

Fu B, Peng MS, Li T, and Stevens DE (2012) Developing versus Nondeveloping Disturbances for Tropical Cyclone Formation. Part II: Western North Pacific*. Monthly Weather Review 140(4):1067-1080

Gray WM (1968) Global view of the origin of tropical disturbances and storms. Mon. Weather. Rev. 96(10):669-700

Hanley D, Molinari J, and Keyser D (2001a) A composite study of the interactions between tropical cyclones and upper-tropospheric troughs. Mon. Weather. Rev. 129(10):2570-2584

Hanley D, Molinari J, and Keyser D (2001b) A composite study of the interactions between tropical cyclones and upper-tropospheric troughs. Mon. Weather Rev. 129(10):2570-2584

Harr PA and Elsberry RL (2000) Extratropical transition of tropical cyclones over the Western North Pacific. Part I: Evolution of structural

characteristics during the transition process. Mon. Weather. Rev. 128(8):2613-2633

Held IM and Soden BJ (2006) Robust responses of the hydrological cycle to global warming. J. Climate 19:5686-5699

Hill KA and Lackmann GM (2009) Influence of environmental humidity on tropical cyclone size. Mon. Weather Rev. 137(10):3294-3315

Houze RA (2010) Clouds in tropical cyclones. Mon. Weather Rev. 138(2):293-344

Huffman GJ, Bolvin DT, Nelkin EJ, Wolff DB, Adler RF, Gu G et al. (2007) The TRMM multisatellite precipitation analysis (TMPA): Quasi-global, multiyear, combined-sensor precipitation estimates at fine scales. J. Hydrometeorol. 8(1):38-55

IPCC (2013) Climate Change 2013: The Physical Science Basis. Contribution of Working Group I to the Fifth Assessment Report of the Intergovernmental Panel on Climate Change [Stocker, T.F., D. Qin, G.-K. Plattner, M. Tignor, S.K. Allen, J. Boschung, A. Nauels, Y. Xia, V. Bex and P.M. Midgley (eds.)]. Cambridge University Press, Cambridge, United Kingdom and New York, NY, USA:1248-1251

Jiang H, Halverson JB, Simpson J, and Zipser EJ (2008a) Hurricane “Rainfall Potential” Derived from Satellite Observations Aids Overland Rainfall Prediction. Journal of Applied Meteorology and Climatology 47(4):944-959

Jiang H, Halverson JB, and Zipser EJ (2008b) Influence of environmental

moisture on TRMM-derived tropical cyclone precipitation over land and ocean. Geophys. Res. Lett. 35(17)

Jiang H, Liu C, and Zipser EJ (2011) A TRMM-based tropical cyclone cloud and precipitation feature database. J. Appl. Meteorol. Climatol. 50(6):1255-1274

Jiang H and Zipser EJ (2010) Contribution of tropical cyclones to the global precipitation from eight seasons of TRMM data: Regional, seasonal, and interannual variations. J. Climate 23(6):1526-1543

Jones SC (1995) The evolution of vortices in vertical shear. I: Initially barotropic vortices. Q. J. R. Meteorol. Soc. 121(524):821-851

Jones SC, Harr PA, Abraham J, Bosart LF, Bowyer PJ, Evans JL et al. (2003) The extratropical transition of tropical cyclones: Forecast challenges, current understanding, and future directions. Wea. Forecasting 18(6):1052-1092

Kam J, Sheffield J, Yuan X, and Wood EF (2013) The Influence of Atlantic Tropical Cyclones on Drought over the Eastern United States (1980–2007). Journal of Climate 26(10):3067-3086

Khouakhi A, Villarini G, and Vecchi GA (2017) Contribution of Tropical Cyclones to Rainfall at the Global Scale. Journal of Climate 30(1):359-372

Kim D, Ho CH, Park DR, and Kim J (2019) Influence of vertical wind shear on wind- and rainfall areas of tropical cyclones making landfall over South Korea. PLoS One 14(1):e0209885

Kim J-H, Ho C-H, Lee M-H, Jeong J-H, and Chen D (2006) Large increase in heavy rainfall associated with tropical cyclone landfalls in Korea after the late 1970s. Geophys. Res. Lett. 33(18):10.1029/2006gl027430

Kim J-H, Ho C-H, Sui C-H, and Park SK (2005) Dipole structure of interannual variations in summertime tropical cyclone activity over East Asia. J. Climate 18(24):5344-5356

Kimball SK (2008) Structure and evolution of rainfall in numerically simulated landfalling hurricanes. Mon. Weather. Rev. 136(10):3822-3847

Klein PM, Harr PA, and Elsberry RL (2000) Extratropical transition of Western North Pacific tropical cyclones: An overview and conceptual model of the transformation stage. Weather Forecast 15(4):373-395

Klein PM, Harr PA, and Elsberry RL (2002) Extratropical transition of western North Pacific tropical cyclones: Midlatitude and tropical cyclone contributions to reintensification. Mon. Weather Rev. 130:2240-2259

Knaff JA, Longmore SP, and Molenar DA (2014) An objective satellite-based tropical cyclone size climatology. J. Climate 27(1):455-476

Knapp KR, Kruk MC, Levinson DH, Diamond HJ, and Neumann CJ (2010) The International Best Track Archive for Climate Stewardship (IBTrACS). B. Am. Meteorol. Soc. 91(3):363-376

Knutson TR, McBride JL, Chan J, Emanuel K, Holland G, Landsea C et al.

(2010) Tropical cyclones and climate change. Nature Geoscience 3(3):157-163

Krishnamurti TN, Biswas MK, Mackey BP, Ellingson RG, and Ruscher PH (2011) Hurricane forecasts using a suite of large-scale models. Tellus A: Dyn. Meteorol.and Oceanography 63(4):727-745

Krishnamurti TN, Pattnaik S, Biswas MK, Bensman E, Kramer M, Surgi N et al. (2010) Hurricane forecasts with a mesoscale suite of models. Tellus A: Dyn. Meteorol.and Oceanography 62(5):633-646

Li YB, Cheung KKW, and Chan JCL (2014) Numerical study on the development of asymmetric convection and vertical wind shear during tropical cyclone landfall. Q. J. R. Meteorol. Soc. 140(683):1866-1877

Lin Y, Zhao M, and Zhang M (2015) Tropical cyclone rainfall area controlled by relative sea surface temperature. Nat. Commun. 6:6591

Liu KS and Chan JCL (1999) Size of tropical cyclones as inferred from ERS-1 and ERS-2 data. Mon. Weather. Rev. 127(12):2992-3001

Liu M, Vecchi GA, Smith JA, and Murakami H (2018) Projection of Landfalling–Tropical Cyclone Rainfall in the Eastern United States under Anthropogenic Warming. Journal of Climate 31(18):7269-7286

Lonfat M, Marks FDJ, and Chen SS (2004) Precipitation distribution in tropical cyclones using the Tropical Rainfall Measuring Mission (TRMM) microwave imager: A global perspective. Mon. Weather. Rev. 132(7):1645-1660

Lonfat M, Rogers R, Marchok T, and Marks FD (2007) A parametric model for predicting hurricane rainfall. Mon. Weather Rev. 135(9):3086-3097

Marks FD, Kappler G, and DeMaria M (2002) Development of a tropical cyclone rainfall climatology and persistence (R-CLIPER) model. 25th Conf. on Hurricanes and Tropical Meteorology, San Diego, CA, Amer. Meteor. Soc., :327-328

Matyas CJ (2010) Associations between the size of hurricane rain fields at landfall and their surrounding environments. Meteorol. Atmos. Phys. 106(3-4):135-148

Matyas CJ (2014) Conditions associated with large rain-field areas for tropical cyclones landfalling over Florida. Phys. Geogr. 35(2):93-106

Matyas CJ (2013) Processes influencing rain-field growth and decay after tropical cyclone landfall in the United States. J. Appl. Meteorol. Climatol. 52(5):1085-1096

Maxwell JT, Soulé PT, Ortegren JT, and Knapp PA (2012) Drought-Busting Tropical Cyclones in the Southeastern Atlantic United States: 1950–2008. Annals of the Association of American Geographers 102(2):259-275

Merrill RT (1984) A comparison of large and small tropical cyclones. Mon. Weather. Rev. 112(7):1408-1418

Molinari J and Vollaro D (1989) External influences on hurricane intensity. Part I: Outflow layer eddy angular momentum fluxes. J. Atmos. Sci.

46(8):1093-1105

Montgomery MT and Smith RK (2017) Recent Developments in the Fluid Dynamics of Tropical Cyclones. Annual Review of Fluid Mechanics 49(1):541-574

Murakami H, Vecchi GA, Underwood S, Delworth TL, Wittenberg AT, Anderson WG et al. (2015) Simulation and Prediction of Category 4 and 5 Hurricanes in the High-Resolution GFDL HiFLOR Coupled Climate Model. Journal of Climate 28(23):9058-9079

Murakami H, Vecchi GA, Villarini G, Delworth TL, Gudgel R, Underwood S et al. (2016) Seasonal Forecasts of Major Hurricanes and Landfalling Tropical Cyclones using a High-Resolution GFDL Coupled Climate Model. Journal of Climate 29(22):7977-7989

Palmen E (1948) On the formation and structure of tropical hurricanes. Geophysica 3(1):26-38

Park D-SR, Ho C-H, Kim J, Kang K, and Nam CC (2016) Highlighting socioeconomic damages caused by weakened tropical cyclones in the Republic of Korea. Nat. Hazards 82(2):1301-1315

Park D-SR, Ho C-H, Nam CC, and Kim H-S (2015) Evidence of reduced vulnerability to tropical cyclones in the Republic of Korea. Environ. Res. Lett. 10(5):054003

Park DR, Ho CH, Chan JC, Ha KJ, Kim HS, Kim J et al. (2017) Asymmetric response of tropical cyclone activity to global warming over the North Atlantic and western North Pacific from CMIP5 model projections.

Sci. Rep. 7:41354

Peatman SC, Klingaman NP, and Hodges KI (2019) Tropical Cyclone–Related Precipitation over the Northwest Tropical Pacific in Met Office Global Operational Forecasts. Weather and Forecasting 34(4):923-941

Peng MS, Fu B, Li T, and Stevens DE (2012) Developing versus Nondeveloping Disturbances for Tropical Cyclone Formation. Part I: North Atlantic*. Monthly Weather Review 140(4):1047-1066

Peng MS, Jeng B-F, and Williams RT (1999) A numerical study on tropical cyclone intensification. Part I: Beta effect and mean flow effect. J. Atmos. Sci. 56(10):1404-1423

Rappaport EN (2014) Fatalities in the United States from Atlantic tropical cyclones: New data and interpretation. B. Am. Meteorol. Soc. 95(3):341-346

Rappaport EN (2000) Loss of life in the United States associated with recent Atlantic tropical cyclones. B. Am. Meteorol. Soc. 81(9):2065-2073

Rayner NA, Parker DE, Horton EB, Folland CK, Alexander LV, Rowell DP et al. (2003) Global analyses of sea surface temperature, sea ice, and night marine air temperature since the late nineteenth century. Journal of Geophysical Research 108(D14)

Reynolds RW, Rayner NA, Smith TM, Stokes DC, and Wang W (2002) An improved in situ and satellite SST analysis for climate. J. Climate 15(13):1609-1625

Rios Gaona MF, Villarini G, Zhang W, and Vecchi GA (2018) The added value of IMERG in characterizing rainfall in tropical cyclones. Atmospheric Research 209:95-102

Ritchie EA and Elsberry RL (2003) Simulations of the extratropical transition of tropical cyclones: Contributions by the midlatitude upper-level trough to reintensification. Mon. Weather. Rev. 131(9):2112-2128

Rodgers EB, Chang SW, and Pierce HF (1994) A satellite observational and numerical study of precipitation characteristics in western North Atlantic tropical cyclones. J. Appl. Meteorol. 33(2):129-139

Sampson CR and Schrader AJ (2000) The Automated Tropical Cyclone Forecasting System (version 3.2). Bull. Amer. Meteor. Soc. 81:1231-1240

Scoccimarro E, Gualdi S, Villarini G, Vecchi GA, Zhao M, Walsh K et al. (2014) Intense Precipitation Events Associated with Landfalling Tropical Cyclones in Response to a Warmer Climate and Increased CO2. Journal of Climate 27(12):4642-4654

Shapiro LJ (1983) The asymmetric boundary-layer flow under a translating hurricane. J. Atmos. Sci. 40(8):1984-1998

Skok G, Bacmeister J, and Tribbia J (2013) Analysis of Tropical Cyclone Precipitation Using an Object-Based Algorithm. Journal of Climate 26(8):2563-2579

Smith RK and Montgomery M (2010) Hurricane boundary-layer theory. Q. J. R. Meteorol. SOC 136:1665-1670

Smith RK, Montgomery MT, and Van Sang N (2009) Tropical cyclone spin-up revisited. Quarterly Journal of the Royal Meteorological Society 135(642):1321-1335

Tuleya RE, DeMaria M, and Kuligowski RJ (2007) Evaluation of GFDL and Simple Statistical Model Rainfall Forecasts for U.S. Landfalling Tropical Storms. Weather and Forecasting 22(1):56-70

Vecchi GA and Soden BJ (2007a) Effect of remote sea surface temperature change on tropical cyclone potential intensity. Nature 450(7172):1066-1070

Vecchi GA and Soden BJ (2007b) Global Warming and the Weakening of the Tropical Circulation. Journal of Climate 20(17):4316-4340

Vecchi GA, Soden BJ, Wittenberg AT, Held IM, Leetmaa A, and Harrison MJ (2006) Weakening of tropical Pacific atmospheric circulation due to anthropogenic forcing. Nature 441(7089):73-76

Villarini G, Lavers DA, Scoccimarro E, Zhao M, Wehner MF, Vecchi GA et al. (2014) Sensitivity of Tropical Cyclone Rainfall to Idealized Global-Scale Forcings. J. Climate 27:4622-4641

Webster PJ, Holland GJ, Curry JA, and Chang HR (2005) Changes in tropical cyclone number, duration, and intensity in a warming environment. Science 309(5742):1844-1846

Willoughby HE (1988) The dynamics of the tropical hurricane core. Aust. Meteor. Mag. 36:183-191

Wong MLM and Chan JCL (2004) Tropical cyclone intensity in vertical wind

shear. J. Atmos. Sci. 61(15):1859-1876

Woods CM and Edwards MC (2008) Factor analysis and related methods. C.R. Rao, J.P. Miller, D.C. Rao (Eds.). Handbook of statistics, volume 27: Epidemiology and medical statistics:367-394

Xu W, Jiang H, and Kang X (2014) Rainfall asymmetries of tropical cyclones prior to, during, and after making landfall in South China and Southeast United States. Atmos. Res. 139:18-26

Yang M-J, Zhang D-L, and Huang H-L (2008) A modeling study of typhoon Nari (2001) at landfall. Part I: Topographic effects. Journal of the Atmospheric Sciences 65(10):3095-3115

Yu H, Chen P, Li Q, and Tang B (2013) Current capability of operational numerical models in predicting tropical cyclone intensity in the Western North Pacific. Wea. Forecasting 28(2):353-367

Yu Z, Yu H, Chen P, Qian C, and Yue C (2009) Verification of tropical cyclone–related satellite precipitation estimates in mainland China. J. Appl. Meteorol. Climatol. 48(11):2227-2241

Zhang W, Vecchi GA, Murakami H, Delworth T, Wittenberg AT, Rosati A et al. (2016) Improved Simulation of Tropical Cyclone Responses to ENSO in the Western North Pacific in the High-Resolution GFDL HiFLOR Coupled Climate Model. Journal of Climate 29(4):1391-1415

국문초록

강풍과 폭우를 유발하는 태풍은 인간에게 가장 위협적인 기상 재해이다. 특히 태풍과 연관된 홍수는 막대한 경제적 피해와 사상자를 유발한다. 따라서 태풍의 강수를 정확히 예측하는 것은 사회적으로 큰 이익을 가져올 수 있다. 그러나 지금까지 태풍의 강수는 태풍의 진로나 강도에 비해 많은 관심을 받지 못했다. 태풍의 강수를 예측하기 위해서는 전 지구 태풍 강수의 기후적 특징과 변화 원리에 대한 이해가 반드시 필요하지만, 지금까지 이에 대해 자세히 연구되지 않았다. 이 논문은 위성 관측 자료를 활용하여 전 지구 태풍 강수의 기후적 특징을 조사하였다. 또한 태풍의 1차 순환, 주변 환경 조건 등 태풍의 강수를 조절하는 다양한 요인들에 대해서도 조사하였다. 이와 같은 방법을 통해 태풍의 강수에 관한 기본적인 지식을 개선할 수 있었다. 아울러, 고해상도 전구 기후 모형을 활용하여 지구 온난화에 따른 태풍 강수의 미래 변화에 대해서도 연구하였다.

이 연구에서는 전구 태풍 강수의 기후적 특징을 1998-2013년 기간의 TRMM-3B42 강수 자료를 활용하여 조사하였다. 태풍 강수 구조의 특징을 나타내기 위해 강수 강도(Rainfall Strength; RS)와 강수 면적(Rainfall Area; RA)을 정의하였다.

먼저 태풍의 강수 강도와 면적의 기본적인 통계량과 시, 공간 분포 등 다양한 특성을 조사하였다. 태풍의 강수 강도와 면적은 지역, 월, 연도에 따라 유의미하게 변하였다. 태풍의 강수 강도와 면적의 변화를 일으키는 원인에 대해 이해하기 위해 태풍 강수와 다양한 요인들(태풍의 1차 순환 및 주변 환경 조건)의 상호 관계에 대해 조사하였다. 그 결과 태풍의 강수 강도는 주로 태풍의 1차 순환에 의해 조절되며, 주변 환경 조건에는 크게 영향을 받지 않는 것으로 나타났다. 이와 반대로 강수 면적은 대규모 저(고)기압 시스템과 환경류 및 해수면 온도와 같은 대규모 환경 조건의 영향을 크게 받는 반면, 1차 순환의 영향을 적게 받는 것으로 확인되었다.

태풍 강수와 이를 조절하는 요인들의 관계는 지역에 따라 달라진다. 특히 태풍의 강수 면적에서 이러한 비선형적인 특징이 잘 나타난다. 태풍의 강수 면적과 주변 환경 조건의 비선형적인 관계에 대해 이해하기 위해 열대와 중위도 지역에서 태풍 강수 면적의 변동성에 대해 조사하였다. 중위도 지역에서는 강한 환경류가 태풍의 강수를 비대칭 적으로 확장시켜 강수 면적을 증가시키는 것으로 나타났다. 반면, 해수면 온도는 강수 면적 변화에 큰 영향을 주지 못하였다. 열대 지역에서는 태풍의 강수 면적과 주변 환경 조건의 관계는 중위도 지역과 반대로 나타났다.

중위도 지역에서는 차가운 해수면 온도에 의해 태풍은 약화되며 환경류에 대한 저항을 잃게 된다. 따라서 태풍의 강수 면적은 환경류 및 해수면 온도에 대해 비선형적인 반응을 하게 된다. 한반도에 상륙하는 태풍에 대해서도 대규모 환경류의 영향과 태풍 강수의 변화 과정에 대해 조사하였다. 한반도 지역에서 나타나는 강한 연직 바람시어에 의해 대체로 태풍의 바람 및 강수 구조는 뚜렷한 비대칭성을 보인다. 또한 태풍의 강수 면적은 연직 바람 시어의 강도에 따라 뚜렷하게 증가하지만, 바람 면적은 유의미하게 변하지 않는 것으로 나타났다. 연직 바람 시어가 강한 사례와 약한 사례에 대해 조사한 결과, 태풍 강수 면적의 증가는 연직 바람 시어가 유도하는 비대칭적인 대류(풍하-좌측/풍상-우측에서의 상승/하강 운동)와 연관된 것으로 확인되었다.

태풍 강수를 조절하는 요인들에 대한 이해에 기반하여, 여섯 개 대양 태풍의 강수 강도 및 면적에 대한 다중 선형 회귀 모형을 구축하였다. 회귀 모형은 여섯 대양의 태풍 강수 강도 및 면적의 변동성을 각각 10.9-37.2% 및 27.0-41.0%를 설명하였다. 회귀 모형은 또한 태풍 강수 강도 및 면적의 기후적 공간 분포와 변동성을 관측과 유사하게 추정하였다. 북인도양, 북서태평양, 동태평양, 북대서양 지역에 대해 태풍 강수 강도 및 면적의 관측과 회귀 모형 간 공간 상관 계수는 각각 0.52-0.95 및 0.74-

0.95로 나타났다. 태풍의 강수 강도 및 면적에 대한 관측 및 모형 간 상관 계수 역시 네 대양에서 유의미하게 나타났다. 따라서 현재 개발한 통계 모형은 북반구 태풍의 강수 강도 및 면적의 기후적 공간 분포 및 변동성을 성공적으로 설명한다. 한편, 남인도양 및 남태평양 태풍의 강수 강도 및 면적에 대한 회귀 모형은 상대적으로 낮은 성능을 보였다.

마지막으로 고해상도 전구 기후 모형을 활용하여 지구 온난화에 따른 태풍 강수의 미래 변화에 대해 예측하였다. 현재 및 미래 기후를 모의하기 위해 각각 70년 기간의 대조군과 RCP4.5 실험군을 설정하였다. 대조군과 실험군에는 각각 1986-2005년 기간의 관측 및 2081-2100년 기간의 17개 CMIP5 모델에서 확보한 해수면 온도와 복사 강제력의 기후 값을 처방하였다. 대조군 실험에서 태풍의 강수 강도를 과대모의 하는 경향이 나타나지만, 모형은 대체로 현재 기후에서 나타나는 태풍 강수 강도 및 면적의 시, 공간 변동성을 잘 모의하였다. RCP4.5 실험에서는 태풍의 강수 강도는 전 지구적으로 균질하게 증가하였다. 반면, 강수 면적은 열대 지역에서는 파동 형태의 변화를 나타냈고, 중위도 지역에서 균질하게 증가하였다. 미래 기후에서 태풍 강수 조절 인자의 변화를 분석한 결과, 균질한 태풍 강수 강도의 증가는 주로 전지구적으로 나타는 균질한 최대

풍속 및 해수면 온도의 증가와 연관된 것으로 나타났다. 한편 열대 지역에서 나타나는 파동 형태의 태풍 강수 면적의 변화는 워커 순환의 약화와 관련될 수 있으며, 균질한 최대 풍속 및 환경류의 증가는 중위도 지역에서 강수 면적 증가의 원인이 될 수 있다.

주요 단어: 태풍, 강수, 전구 기후, 전구 기후 모형, 기후 변화

학번: 2012-20334

감사의 글

이 논문을 완성하기까지 도움을 주신 많은 분들께 이 자리를 빌어 감사인사를 드립니다. 학부부터 박사학위를 마무리 할 때까지 저를 지도해주시고 아낌없이 지원해주신 허창회 교수님께 진심으로 감사 드립니다. 허 교수님을 통해 독립된 연구자가 갖춰야 할 능력과 가치관을 배울 수 있었습니다. 제 논문의 심사위원을 맡아주시고, 연구를 진행하는데 필수적인 수많은 조언을 해주신 백종진 교수님, 손석우 교수님, 유희동 부산지방기상청장님, Johnny Chan 교수님께도 감사 드립니다. 그리고 학생들의 학문적 소양을 길러주시기 위해 언제나 힘쓰시는 모든 대기과학 전공 교수님들께 감사의 말씀을 전합니다.

대학원 과정에서 만난 가장 소중한 인연은 기후물리실험실 선후배님들과의 인연입니다. 대학원에 들어와 어떤 연구를 할지 고민 중이던 저를 태풍의 세계로 이끌어주시고 처음으로 연구라는 것이 무엇인지 알려주신 진천실 형께 먼저 감사 드립니다. 제 학위 연구의 시작과 끝까지 함께하며, 연구적으로나 정신적으로나 지금의 저로 성장하는데 가장 큰 역할을 하신 박두선 형께 너무나도 많은 도움을 받았습니다. 짧은 글로 표현하기에는 부족하지만 감사의 말씀 전합니다. 각지에서 활약하고 계시는

김주홍 박사님, 정지훈 교수님, 이윤복 형, 최형진 교수님, 최용상 교수님, 박명숙 박사님, 정수종 교수님, 박태원 교수님, 김형석 교수님, 박상종 박사님, 전상윤 박사님, 홍선영 누나, 이윤경 박사님, 이윤곤 교수님, 이민희 박사님, 이승민 박사님, 박정현 누나께 감사 드립니다. 선배님들을 롤모델로 삼아, 발자취를 따라가며 많은 것을 배우고 느낄 수 있었습니다.

실험실의 기둥 역할을 해주시는 오혜련, 김현주 박사님, 제게 코딩을 가르쳐주셨고 후배들을 살뜰히 챙기시는 박창의 형, 안에서나 밖에서나 단짝처럼 붙어 다녔던 최우석 형, 501동의 NPC, 과제적토마 등 다양한 업적을 가지고 있는 박훈영 형, 척척 박사이자 김바리의 주요 고객이신 조희제 형, 카리스마 있는 德中德 이그림 누나, 이벤트가 있을 때마다 세심하게 챙겨주시는 허선경 누나, 언제나 유쾌한 한국인 Steven, 과제 전우이자 정 많은 아재 박창균 형, 든든한 후배이자 배울 점이 많은 허진우와 장민희께 감사 드립니다. 언제나 노력하는 윤정민과 앞으로가 기대되는 김익호, 실험실의 새로운 핵심 일꾼이 될 백관구, 박인규, 김가영, 현동규에게도 감사와 응원의 말씀을 전합니다. 졸업 후 각자의 길을 개척하는 남채현, 한여진, 정지영도 원하는 바를 모두 이루길 기원합니다. 대학원에 같이 들어와 동고동락한 권형안, 이승언, 이아름, 조채윤께도 감사의 마음을 전합니다. 앞으로 모두

원하는 자리에서 멋진 활약을 하리라 믿습니다.

학위를 마치기까지 긴 시간 동안 언제나 저를 응원해주시고 어려운 순간마다 힘이 되어주신 부모님께 깊이 감사 드립니다. 앞으로 더 자랑스러운 아들이 될 수 있도록 노력하겠습니다. 사랑합니다. 저를 친아들처럼 아껴주시고 격려해주시는 장인어른과 장모님, 그리고 과묵하지만 많은 것들을 신경 써주시는 강종모 형님께도 진심으로 감사 드립니다. 마지막으로 모든 순간을 영원히 함께할 사랑하는 아내 강현선에게 고마움을 전합니다.